Article

Vision System for the Mars Sample Return Capture Containment and Return System (CCRS)

Brent J. Bos [1,*], David L. Donovan [2], John I. Capone [1], Chen Wang [3], Terra C. Hardwick [1], Dylan E. Bell [4], Yuqing Zhu [1], Robert Podgurski [1], Bashar Rizk [5], Ireneusz Orlowski [4], Rachel A. Edison [4], David A. Harvey [4], Brianna Dizon [4], Lindsay Haseltine [4], Kristoffer C. Olsen [4], Chad Sheng [4], Robert R. Bousquet [4], Luan Q. Vo [4], Georgi T. Georgiev [1], Kristen A. Washington [1], Michael J. Singer [6], Stefan Ioana [6], Anloc H. Le [1], Elena M. Georgieva [1], Michael T. Hackett [1], Michael A. Ravine [7], Michael Caplinger [7], Phillip Coulter [1], Erin Percy [1], Charles Torisky [4], Jean-Marie Lauenstein [1], Kaitlyn L. Ryder [1], Michael J. Campola [1], Dillon E. Johnstone [8], William J. Thomes [1], Richard G. Schnurr [1], John C. McCloskey [1], Eugenia L. De Marco [1], Ellen Lee [1], Calinda M. Yew [1], Bo Yang [1], Mingyu Han [9] and Bartosz Blonski [9]

[1] NASA Goddard Space Flight Center, Greenbelt, MD 20771, USA; georgi.t.georgiev@nasa.gov (G.T.G.); anloc.le@nasa.gov (A.H.L.); michael.t.hackett@nasa.gov (M.T.H.); richard.g.schnurr@nasa.gov (R.G.S.); calinda.m.yew@nasa.gov (C.M.Y.); bo.yang@nasa.gov (B.Y.)
[2] McCallie Associates, Greenbelt, MD 20771, USA; localmaximums@protonmail.com
[3] KBR Incorporated, Houston, TX 20771, USA
[4] Genesis Engineering Solutions, Lanham, MD 20706, USA; lhaseltine@genesisesi.com (L.H.)
[5] Lunar and Planetary Laboratory, University of Arizona, Tucson, AZ 85721, USA
[6] Aerodyne Industries, Cape Canaveral, FL 32920, USA
[7] Malin Space Science Systems, San Diego, CA 92121, USA
[8] Science Systems and Applications, Lanham, MD 20706, USA
[9] United States Naval Academy, Annapolis, MD 21402, USA
* Correspondence: brent.j.bos@nasa.gov; Tel.: +1-301-286-5670

Abstract: The successful 2020 launch and 2021 landing of the National Aeronautics and Space Administration's (NASA) Perseverance Mars rover initiated the first phase of the NASA and European Space Agency (ESA) Mars Sample Return (MSR) campaign. The goal of the MSR campaign is to collect scientifically interesting samples from the Martian surface and return them to Earth for further study in terrestrial laboratories. The MSR campaign consists of three major spacecraft components to accomplish this objective: the Perseverance Mars rover, the Sample Retrieval Lander (SRL) and the Earth Return Orbiter (ERO). Onboard the ERO spacecraft is the Capture, Containment and Return System (CCRS). CCRS will capture, process and return to Earth the samples that have been collected after they are launched into Mars orbit by the Mars Ascent Vehicle (MAV), which is delivered to Mars onboard the SRL. To facilitate the processing of the orbiting sample (OS) via the CCRS, we have designed and developed a vision system to determine the OS capture orientation. The vision system is composed of two cameras sensitive to the visible portion of the electromagnetic spectrum and two illumination modules constructed from broadband light emitting diodes (LED). Vision system laboratory tests and physics-based optical simulations predict CCRS ground processing will be able to correctly identify the OS post-capture orientation using only a single vision system image that is transmitted to Earth from Mars orbit.

Keywords: Mars; cameras; sample return; space optics

1. Introduction

On 18 February 2021, the National Aeronautics and Space Administration's (NASA) Mars Perseverance rover completed a successful touchdown at Jezero crater on Mars. Its purpose is as follows: to explore and acquire samples from a part of Mars containing telltale signatures of aqueous alteration [1]. Perseverance arrived on Mars containing

43 sample tubes in total. A total of 5 of the 43 tubes serve as witness samples while 38 are available for storing Mars samples. During its initial science campaign, Perseverance filled nine of its onboard titanium sample tubes. Its first sample, an atmospheric sample acquired on 6 August 2021, was followed by eight samples gathered from the Máaz and Séítah formations, areas believed to be igneous in origin containing rocks aqueously altered on multiple occasions [1]. As of this writing, Perseverance has collected a total of 23 Martian samples and completed deposition of a ten-sample-tube cache in the Three Forks region of Mars on 28 January 2023. The Three Forks surface cache contains nine Mars samples (including the initial atmospheric sample) and a witness sample tube serving as an experimental control.

The launch, landing and Mars surface operations of the Perseverance rover are just the initial steps of the first phase of the NASA and European Space Agency (ESA) Mars Sample Return (MSR) campaign. The goal of the MSR campaign is to collect scientifically interesting samples from the Martian surface and return them to Earth for further study in terrestrial laboratories. Of particular interest for return are samples to help us understand the history of liquid water on Mars as well as its habitability in the distant past. Three major spacecraft components make up the current MSR campaign design: the Perseverance Mars rover currently operating, the Sample Retrieval Lander (SRL) and the Earth Return Orbiter (ERO). See Figure 1 for an artist's rendition of the MSR campaign's major components.
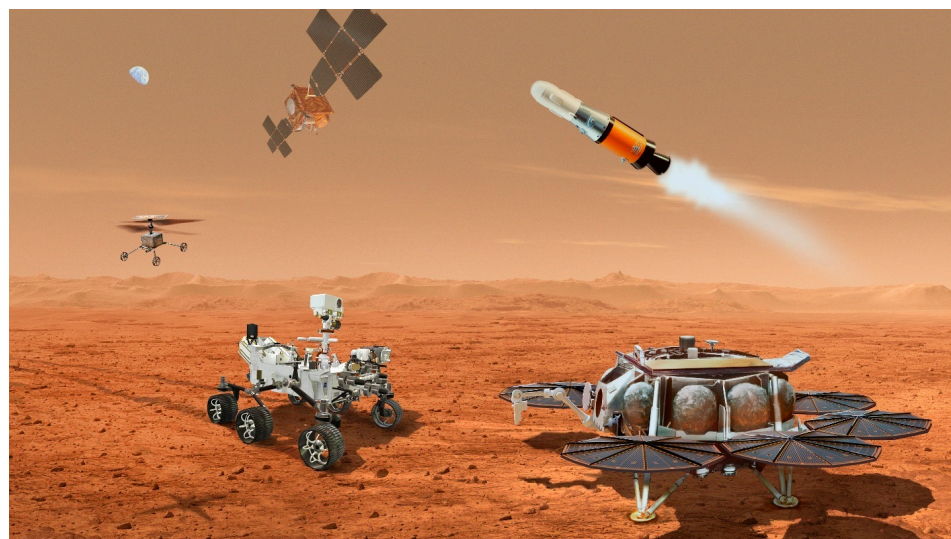

Figure 1. Artist's rendition of the Mars Sample Return (MSR) campaign's major components. In the lower left is the Perseverance Mars rover that successfully landed on Mars on 18 February 2021 and is currently acquiring up to 38 samples from the Mars surface and atmosphere. In the lower right is shown the Sample Retrieval Lander (SRL) which delivers to the Martian surface the Sample Transfer Arm and the Mars Ascent Vehicle (MAV) which is shown launching the Orbiting Sample (OS) container into Mars orbit. In the far left one of two SRL helicopters is shown which will be used as backup to retrieve cached sample tubes in case Perseverance experiences a failure prior to the arrival of the SRL. At the top is shown the Earth Return Orbiter (ERO) which will rendezvous with the OS container and capture it using the Capture, Containment and Return System (CCRS) that is included as part of its payload. After successfully capturing and processing the OS for Earth return, the ERO will leave Mars orbit and deliver the samples back to Earth.

The role of the SRL spacecraft is to land near the Perseverance rover on Mars, collect the Martian sample and witness tubes acquired by Perseverance and launch those samples into Mars orbit. The nominal plan is for the Perseverance rover to deliver the sample tubes to the SRL to put them within reach of the ESA-provided Sample Transfer Arm. This arm will load the sample tubes, one at a time, into the Orbiting Sample (OS) container which sits atop the Mars Ascent Vehicle (MAV). After the OS is loaded with samples, the MAV

launches from the SRL and inserts the sample container into Mars orbit. The OS container is approximately 239 mm in length and 221 mm in diameter, similar in shape (but smaller in size) to a commercially available propane tank (see Figure 2). It can hold as many as 30 titanium sample tubes from Perseverance. In the event that the Perseverance rover cannot deliver its samples to the SRL, the SRL also will deliver to the Martian surface two helicopters that can be used to retrieve the samples that Perseverance has cached on the surface. These will be similar in design to the Mars helicopter that successfully flew on Mars for the first time on 19 April 2021 [2].
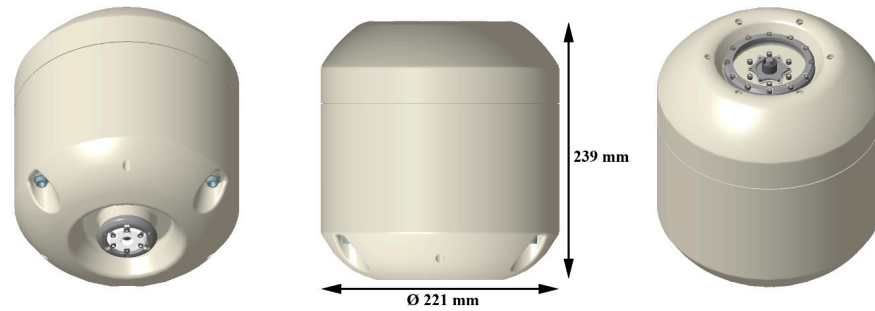

Figure 2. Conceptual computer aided design (CAD) views of the Orbiting Sample (OS) container as it appears in Mars orbit after release from the MAV (Mars Ascent Vehicle) showing an oblique view of the base endcap (**left**) and the lid endcap (**right**).

After the OS separates from the MAV and is inserted into Mars orbit, the MSR ERO spacecraft will rendezvous with the OS and capture it using part of its payload called the Capture, Containment and Return System (CCRS) (see Figure 3). The ERO spacecraft as well as the ERO launch vehicle are being provided by ESA. The CCRS is being provided by NASA's Goddard Space Flight Center (GSFC).
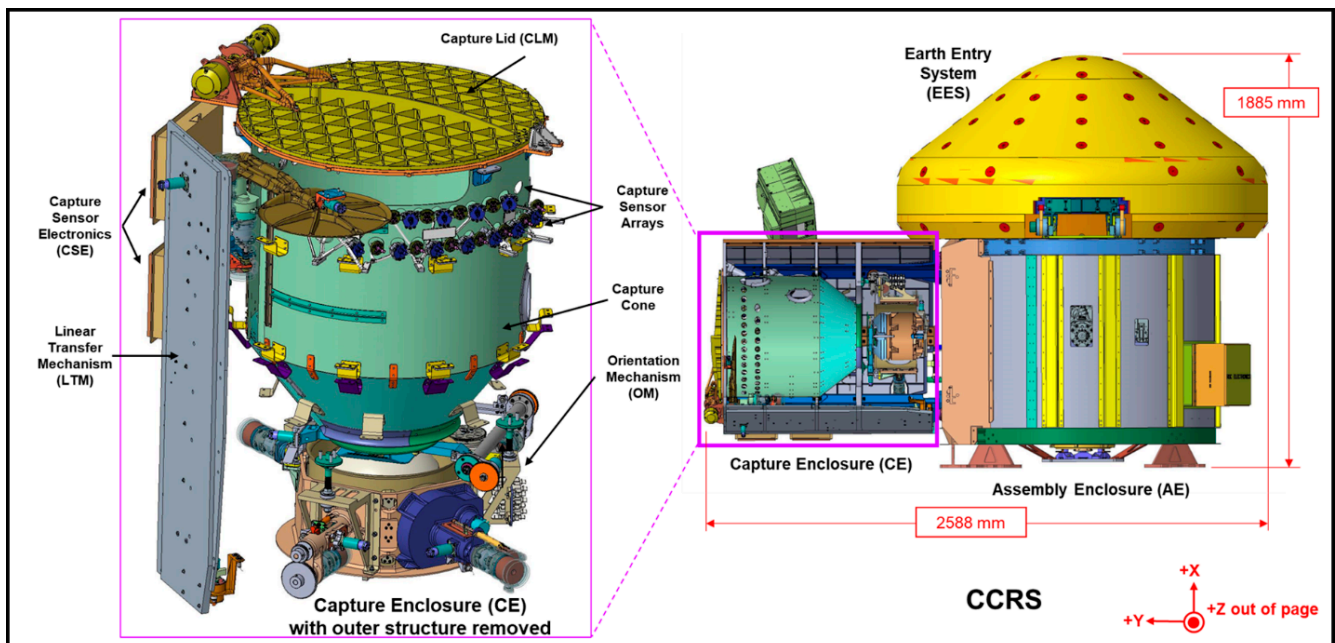
Figure 3. Conceptual computer aided design (CAD) views of the ERO (Earth Return Orbiter) Capture, Containment and Return System (CCRS) payload. The coordinate system axes shown in the lower right have their origins offset from the actual (0, 0, 0) vertex for clarity.

After the OS is captured and prepared for delivery to Earth, ERO will leave Mars orbit on an Earth-return trajectory to release the CCRS Earth Entry System (EES). The EES will

enter Earth's atmosphere and impact Earth's surface at the EES terminal velocity within the Utah Test and Training Range (UTTR) near Dugway, Utah. After landing in Utah the Mars samples will be transported to the NASA Johnson Space Center for curation before they are shared with other institutions around the world.

The primary CCRS operations begin after the OS container is inserted into Mars orbit. The ERO targets and rendezvous with the orbiting OS and maneuvers to align the OS orbital trajectory with the centerline of the CCRS capture cone, approaching the OS with a large enough closing velocity to overtake it. The CCRS then performs a series of functions to capture the OS within its interior.

First, the CCRS capture lid is commanded to open to expose the capture cone to space. Then, upon entry to the CCRS, the OS trips optical capture sensors which trigger a rotation of the linear transfer mechanism (LTM) into position within the cone's interior. The LTM then sweeps/pushes the OS to a captured reference position within an orientation mechanism at the end of the capture cone.

After OS capture, the CCRS begins a choreographed series of back-and-forth steps between sub-systems to sterilize the OS exterior, attach a lid assembly to the OS base and move the OS out of the CCRS capture enclosure volume and into the assembly enclosure using a rotation and transfer mechanism. Finally, the rotation and transfer mechanism loads the OS into the EES and closes out the EES for the return to Earth.

Before the rotation and transfer mechanism can mate the lid assembly to the OS, the CCRS must determine if it is safe for the hardware to do so by confirming proper OS orientation. The purpose of the vision system is to supply OS image telemetry to perform that critical inspection step.

2. Vision System Overview

The CCRS vision system is one of eleven CCRS sub-systems. The primary vision system objective is to acquire images of the OS container after it has been captured by the CCRS and held stationary with respect to the vision system within the CCRS orientation mechanism. Post-capture OS images will allow CCRS operators on the ground to discern the orientation of the OS prior to sterilization and processing for Earth return. CCRS mechanical constraints only allow the OS to be held in the orientation mechanism in one of two orientations. If the vision system images reveal that the OS is in the wrong orientation for further processing by the CCRS, then the orientation mechanism will rotate the OS 180° and the vision system will acquire additional images to determine that the reorientation was successfully completed.

In addition to its primary function, the vision system can also provide supplementary information in support of other CCRS operations. For instance, if the LTM funneling process does not successfully deliver the OS to the orientation mechanism, then vision system images can provide situational awareness to inform contingency operations. The vision system can also provide telemetry that the ultraviolet (UV) illumination system is operational prior to OS capture [3]. Although the vision system cannot directly detect the 280 nm ultraviolet radiation, it is sensitive enough to image the secondary visible illumination generated by UV fluorescence from certain CCRS surfaces.

The CCRS vision system architecture is based upon cameras using two-dimensional, silicon detector arrays with fixed-focus, refractive lenses and an illumination system that utilizes broadband light emitting diodes (LED). Similar types of imaging systems have been successfully operating at Mars since 1997 [4,5], and LED-based illumination systems were flight-qualified for Mars conditions shortly thereafter [6,7].

The CCRS vision system consists of two camera heads and two illumination modules. Only one camera is required to fulfill the vision system's operational goals but two are included for full system redundancy. Similarly, only one illumination module is required to take satisfactory images of the OS container but a second is included for full redundancy. The illumination modules are wired in a distributed manner such that any single or double system failure (except for double-fault cases where both cameras become inoperable or

power is lost to both the primary and redundant electronics) will not degrade vision system performance. This arrangement is also resilient to roughly half of the possible triple failure modes, producing images that, though degraded, still meet requirements.

All the vision system components are located within the CCRS interior and mounted via bracketry to the capture cone bulkheads. Portholes within the capture cone provide lines of sight to the post-capture OS container and allow light from the illumination modules to illuminate the OS. Each camera has a dedicated porthole whereas the pair of illumination modules share a single large porthole. See Figure 4 for an illustration of the vision system location within CCRS.
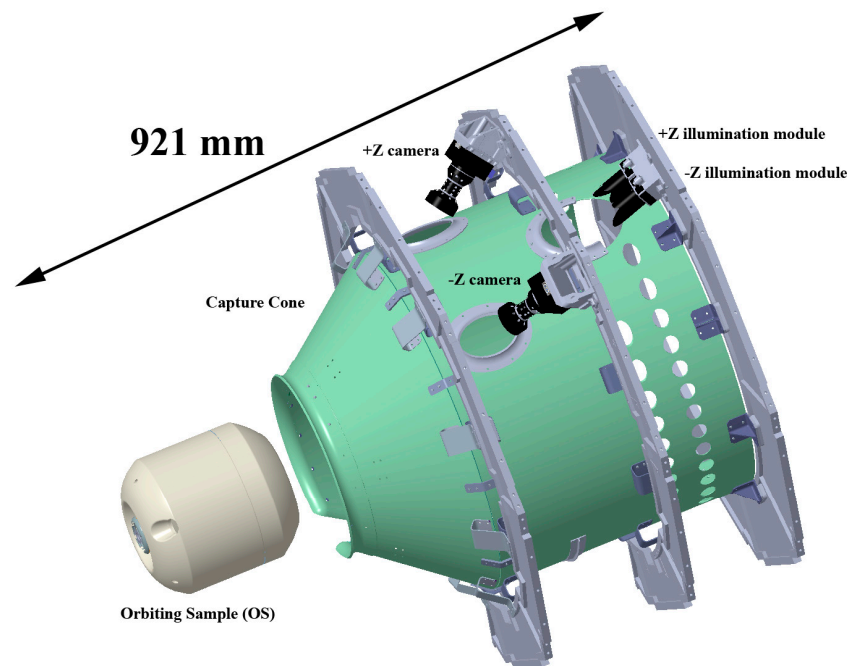
Figure 4. Simplified internal view of a portion of the CCRS (capture enclosure) showing the location of the vision system with respect to the capture cone (pale green) and the post-capture OS (off white). Brackets mount the two vision system cameras and illumination modules to two different CCRS bulkheads. Views of the OS and apertures for illumination are provided by three portholes in the capture cone cylinder. Each camera has a dedicated porthole while the two illumination modules share one large porthole. The colors (black) shown for the vision system components are true-to-life whereas the colors applied to all the other components are for figure clarity. The orientation mechanism is not shown to make the post-capture OS position clearly visible.

The CCRS vision system's optical performance is inextricably linked to the OS container's external optical properties, specifically the optical properties of the container endcaps, as well as the CCRS interior's ambient lighting conditions. Due to the immaturity of the CCRS mechanical and thermal blanket closeout design and uncertainties regarding spacecraft-to-sun vectors during on-orbit operations, the minimum ambient light level within the CCRS interior has yet to be bounded. In response, we have designed the vision system to function properly with or without the presence of ambient light coming directly from the Sun or reflected from the Martian disk. We initially considered near-infrared and thermal-infrared imaging solutions within the vision system design trade space. We did not choose that approach due to cost and schedule constraints as well as the much greater spaceflight heritage offered by visible-light imagers.

To take advantage of current camera designs that have spaceflight heritage we designed our system around camera offerings from industry and academic sources and developed a new, custom illumination system to enable any such camera to acquire high-fidelity OS images. To do this prior to the completion of the OS design, we developed

optical property requirements for the OS container endcaps which the OS team considered as part of the OS design.

The first optical property we specified for the OS container endcaps was for their bidirectional reflectance distribution functions (BRDF) to lie within the range shown in Equation (1) over the 400–900 nm wavelength range and angles of incidence and reflectance, θ_i and θ_r, respectively.

$$0.2 \text{ sr}^{-1} \leq \text{BRDF}(\theta_i, \theta_r) \leq 10 \text{ sr}^{-1} \text{ for } \theta_i = -80° \text{ to } 80°, \theta_r = -80° \text{ to } 80° \tag{1}$$

This BRDF specification allowed for a broad range of OS endcap surface treatments for the OS design team to consider. At the high end, the OS endcap reflectivity is allowed to be highly specular (31-times more reflective than an ideal Lambertian reflector) and at the low end its reflectance can be just 63% that of an ideal Lambertian reflector. For the vision system, we used these agreed-to BRDF limits to specify the range of acceptable illumination levels for the illumination system based on typical sensitivities for flight-heritage cameras and the illumination module-to-OS distances.

The second optical property we specified for the OS container endcaps was for individual and localized surface features to have a BRDF, BRDF_f, that differs from the surrounding surface BRDF over the 400–900 nm wavelength range by at least 25% as described with Equation (2).

$$\frac{\left| \text{BRDF}_f(\theta_i, \theta_r) - \text{BRDF}(\theta_i, \theta_r) \right|}{\text{BRDF}_f(\theta_i, \theta_r) + \text{BRDF}(\theta_i, \theta_r)} \geq 0.25 \text{ for } \theta_i = -80° \text{ to } 80°, \theta_r = -80° \text{ to } 80° \tag{2}$$

This OS contrast requirement ensured that whatever camera we selected, we would be imaging a scene with discernible features and not just an object that, while detected as being present (by meeting the specification in Equation (1)), would be devoid of resolvable features. We defined the OS feature contrast in this manner so that we could use it directly to predict camera system performance using modulation transfer function (MTF) values. During initial development, we required that OS contrasting features be at least 5 mm in size so that the vision system cameras could resolve them. Due to the viewing angles, OS topography and feature locations, this meant that the cameras needed to resolve detail ~3 mm or larger. We will show in Section 5 of this paper that now that the OS design is mature, we are able to determine that the OS endcap surface geometry by itself provides enough diversity in shape and large enough gradients in local surface slopes that shadows and shading are easily resolvable by the CCRS vision system even if individual features have the same BRDF as the background material.

Based on these two general reflective properties of the OS endcaps, we developed optical requirements for both the vision cameras and the illumination modules and flowed them to the individual components. These will be discussed further in Sections 4.1 and 4.2.

For radiometric requirements, we use photometric units for illuminance and luminance in place of radiometric units (e.g., Watts or photons) for irradiance and radiance. We did this due to three practical considerations. First, the vision system is intended to operate over a broad portion of the visible spectrum. Specifying irradiance and radiance over a broad wavelength range using radiometric units would also require an accompanying description of the applicable wavelength range as well as restrictions or descriptions on how the Watts or photons can be concentrated or distributed throughout the spectrum. Photometric units, although not perfectly constrained, are standardized with respect to a well-known and defined response curve. They do not require an accompanying ad hoc and elaborate spectral definition within the specification to eliminate ambiguity on where the optical power can fall on the spectrum. Second, most commercially available calibrated detectors that operate over the entire visible wavelength band are calibrated in photometric units of lux (or lumens/m^2). Third, most (if not all) commercially available broadband LEDs are specified in terms of their total photometric output. By working entirely in

photometric units, we eliminate the errors, approximations and assumptions we would need to introduce in order to work with the absolute radiometric units that we typically work with on spacecraft optical instrumentation.

3. Vision System CCRS Accommodations and Key Interfaces

The CCRS vision system components are mechanically attached to the CCRS capture cone bulkheads using brackets. The vision system, bulkhead and bracket interfaces all include pinned interface features. This provides installation repeatability during the ground integration and test phase and reduces the vision system alignment shift caused by launch loads. Mechanical surfaces with lines of sight to the interior of the vision system camera lens barrels are treated with low reflectance coatings or wrapped in low reflectance, visibly black blankets to minimize stray light.

All vision system components are mounted to aluminum capture enclosure structures. This provides adequate thermal conduction. The CCRS thermal design also requires all vision system hardware to have black (emissivity ≥ 0.8 over the wavelength range of 4 to 40 μm) exterior surfaces to facilitate radiative coupling. The capture enclosure thermal design requires it to be cold-biased. Vision system components are as follows:

- Passively kept below hot operational temperature limits during operations;
- Passively kept below hot survival temperature limits when not operating;
- Actively kept above cold survival and operational temperature limits using dedicated camera and illumination module heaters that are switched on by non-programmable thermostats.

Primary and redundant power is provided to the vision system cameras and illumination system via the CCRS avionics. Each camera communicates with the CCRS avionics via SpaceWire and is connected to a 5 V, unswitched service. Electrical power is provided to a camera anytime its corresponding side of the avionics is on. The illumination system is on a switched 28 V power service and shares the switched service with other CCRS sub-systems. Although the vision system cameras will go through a series of EMI/EMC (electromagnetic interference/electromagnetic compatibility) characterization tests prior to delivery, the current plan for CCRS operations is to not provide power to the cameras while the ERO Electra channel is required for communications.

A summary of the key CCRS-to-vision-system resources and interfaces is provided in Table 1.

Table 1. Summary of the key CCRS-to-vision-system interface values. Values in brackets represent the maximum allowed while other values shown are the current best estimate (CBE).

Key CCRS Vision System Interface Values—CBE [Max Budget]		
Metric	**Camera (Each)**	**Illumination Module (Each)**
Mass (kg)	0.5 [0.525] without cable	0.075 [0.115] without flying leads
Volume (mm)	100 (dia) by 120 (height)	Base 62 × 38 × 18 (height) Baffle Ø36 × 36 (height)
Distance (mm) mounting plane to OS endcap	589.44	723.56
Angle (deg) boresight to OS centerline	38.0	26.5
Data Interface	SpaceWire	N/A
Power (W)	2.0 [2.5]	6.35 [7.0]
Supplied Bus Voltage (V)	5 (unswitched)	28 (switched)
Supplied Max Bus Current (amps)	[1.0]	[0.5]
Survival Temp Range (°C)	−50 to +70	−40 to +55
Operating Temp Range (°C)	−30 to +40	−30 to +45
Turn-on Temp Range (°C)	−40 to +55	−40 to +55
Thermal Dissipation (W)	1.25 on, not imaging [2.0]	[5.0] both strings

4. Vision System Description and Design

4.1. Camera Description

Tasked with delivering an imager in less than two years to provide the critical OS orientation telemetry, we based our initial vision system concepts on existing camera designs that had flight heritage. Ultimately, we selected a camera that had already proven itself on a previous NASA sample return mission: the Malin Space Science Systems (MSSS) ECAM C50 that flew as StowCam in the OSIRIS-REx TAGCAMS [8,9]. That camera had the responsibility of documenting the secure deposition of the OSIRIS-REx sample head within the Sample Return Capsule (SRC), a critical operation for that mission.

For the Mars Sample Return and OSIRIS-REx applications, both missions' cameras record events initiated by spacecraft mechanisms under controlled illumination and image acquisition conditions. For example, in both cases, the target exhibits no relative motion with respect to the camera. The cameras differ, however, in several respects: (a) while the sun illuminated the StowCam scene, an artificial light source would be necessary to enable OS imaging within the capture cone; (b) due to mass constraints, the cameras could not use the usual MSSS electronics control module called a DVR (digital video recorder)—but would have to be controlled directly from the spacecraft avionics; (c) because of volume constraints, the cameras could not include the typical stray light baffle (a highly effective part of the StowCam with multiple stray light vanes); (d) the cameras would utilize a new lens design, although almost identical to the StowCam focal length f-number and optical quality, it would be significantly easier for MSSS to manufacture.

Each of these alterations—to varying degrees—complicated the strong heritage provided by the ECAM. However, they were mitigated by a number of factors. First, MSSS has delivered numerous iterations of its ECAM camera line—the basis for StowCam—including versions dispensing with the electronics controller and stray light baffle. Second, new refractive optics prescriptions, those that change nothing about the mechanical and thermal principles underlying the physical design but simply provide a more manufacturable prescription, we consider almost routine. This is particularly true when the number of elements and lens materials are similar to the flight heritage. The latter was a relevant and timely risk reduction due to the short delivery schedule of the capture enclosure cameras.

With the OS captured and stationary, and while mounted to a fixed position inside the capture enclosure, the vision system cameras will collect and transfer to the avionics sub-system at least one image of the OS endcap to determine its orientation. The minimum camera requirement is to capture detail as small as 3 mm with a contrast (modulation) larger than 0.6 when the scene luminance is ≥7.8 lumens/m2/steradian. The OS will be stationary during the exposure, allowing us, during operations, to retain exposure time as a powerfully flexible parameter to conserve margin and reduce risk. By design, overexposed portions of an image, up to a factor of at least 100, will not materially encroach on other parts of the image [9].

The cameras use the same detector (with the same integral Bayer color filter) and camera head electronics as StowCam. The detectors are commercial complementary metal oxide semi-conductor (CMOS) image sensors (ON Semicondutor MT9P031 5-megapixel image sensor) with a total of 2752 × 2004 readout pixels and an active image area of 2592 × 1944 pixels. The independently validated pixel pitch is 2.2 μm while the optically active pixel area determined from microscopic inspection and analyses is ~1.43 μm × 1.43 μm [9]. As described by Bos et al. [9], for the most accurate image reduction it is beneficial to readout the entire 2752 × 2004 image to assess detector dark current and electronic offsets. A rolling shutter controls exposure durations. By default, the sensors produce 12-bit pixel values with digital numbers (DN) ranging from 0 to 4095. The camera heads also include an Actel FPGA (field programmable gate array) for sensor control, communications and voltage regulation to supply power. A block diagram of the camera heads is shown in Figure 5. A short bandpass filter is located in front of the detector to block infrared light within the silicon pixel response. The average transmission of the filter is >82%. When combined with the anti-reflection coatings of the camera lenses, the spectral response

of the cameras is between 400 nm to 700 nm. Since OSIRIS-REx, NASA has also flown two more camera heads with the monochrome versions of the same detectors as part of the Terminal Tracking Camera (TTCam) on the Lucy Trojan asteroid mission [10]. The SpaceWire electrical interface adopted by the CCRS is also the standard camera interface provided by MSSS.

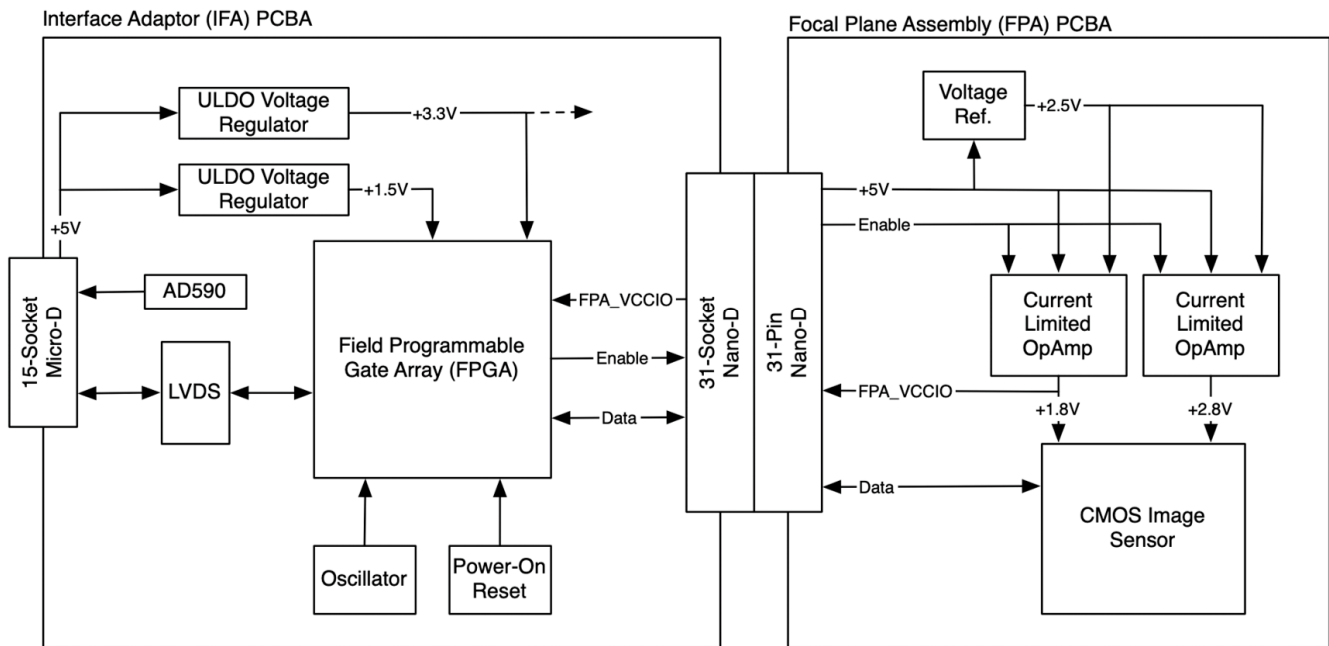# Camera Electronics Block Diagram

Figure 5. Electrical block diagram of the vision system camera head.

In order to discriminate between the OS lid and base, the cameras need to acquire images with sufficient resolution and field of view. To achieve this, we defined a cylindrical depth-of-field volume requirement of 235 mm in diameter and 60 mm long over which the cameras have to resolve a 3 mm diameter feature with an MTF of 0.6 or greater. This volume is located 461 mm (see Figure 6) from the first lens vertex of the CCRS cameras at an angle of 38.0° off the nominal post-capture OS centerline. We sized the depth-of-field volume based on the following: the nominal OS design, the OS tolerances and the combination of the CCRS uncertainties and tolerances in between the camera's mechanical interface and the post-capture OS location and orientation. The imaging scenarios are rotationally symmetric about the CCRS capture cone y-axis, making the camera viewing geometries (and requirements) with respect to the OS identical to each other.

To capture the required OS endcap images, both cameras use the same 7.1 mm focal length lens operated at F/3.5 with the best focus (i.e., minimizes aberrations) set for an object located 493 mm from the first lens surface vertex. The lens design uses two lens groups with a 4.26 mm diameter aperture stop located between them. Two aspheric lenses are used for correcting image aberrations and reducing the lens count. The athermal design of the lens assembly enables the camera to stay in focus while operating over the temperature range of −30° to 40 °C. Figure 7 shows the 7.1 mm lens layout and ray trace. When integrated with the camera detector, the lens provides a wide 45.6° × 34.3° field of view (57.0° diagonal) over the 2592 × 1944 active imaging area. The camera instantaneous field of view (IFOV) or single pixel scale is 0.31 mrad.
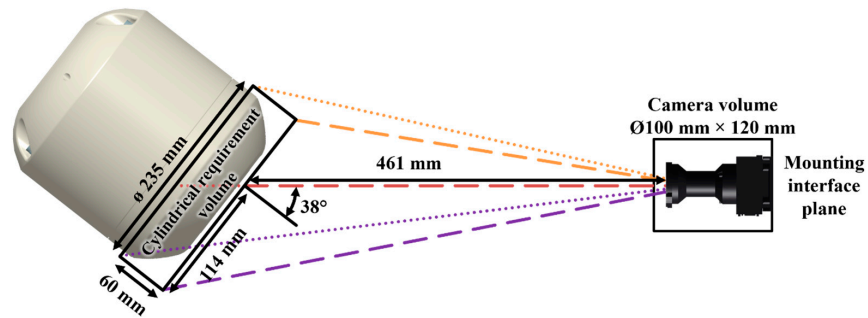
Figure 6. Diagram of the OS depth-of-field volume with respect to the nominal camera locations and volume allocations. The 461 mm distance shown is from the vertex of the first lens surface to the first plane in the depth-of-field cylindrical volume. The best focus is set for a position 493 mm from the first lens vertex. MTF curves at the field positions illustrated above are provided in Figure 8.
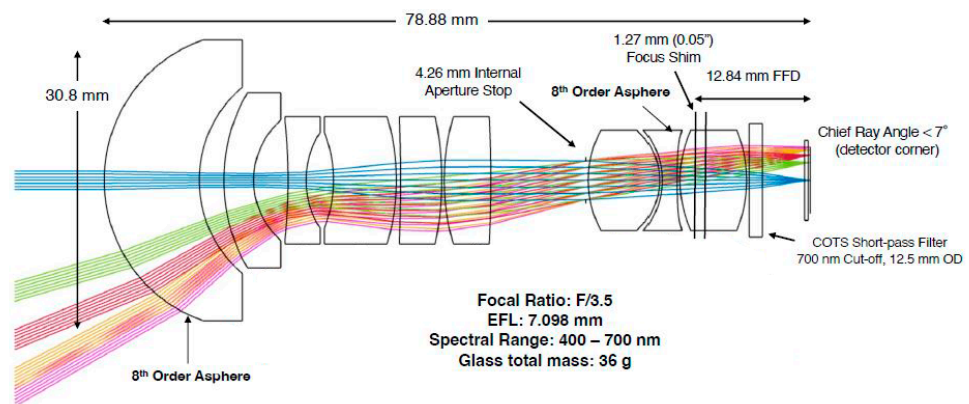

Figure 7. Layout and ray trace of the vision system camera lens.

Figure 8 shows the predicted nominal MTF performance for the camera when imaging a 3 mm object on planes normal to the camera boresight and located at the near and far positions of the cylindrical depth-of-field volume. The MTF calculations include the degradation caused by the camera detector's MTF. The field points correspond to those shown in Figure 6.
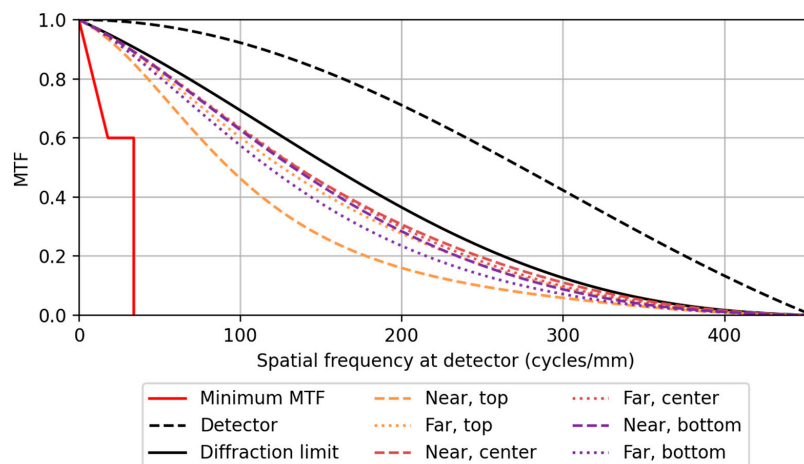

Figure 8. The minimum required and predicted camera MTF performance at the center and corners of the camera detector active imaging area for flat planes located at the near and far planes of the depth-of-field requirement volume, as depicted in Figure 6. The plot ends at a spatial frequency of 454.5 mm^{-1} which is equivalent to the highest sampling frequency of the detector. The prediction includes the optical as well as the detector MTF.

To determine the camera design compliance with the depth-of-field specification, we created a camera model that uses raytracing to determine the optical contribution to the point spread function (PSF) and an idealized pixel model to calculate the detector PSF. Figure 9 shows the predicted pixel sampling and nominal MTF performance for the selected camera at the extreme ends of the depth-of-field cylinder. This shows there is significant margin to meet the >0.6 contrast requirement for an object 3 mm or larger in size. Table 2 summarizes the key vision system camera parameters. Figure 10 shows a previously constructed ECAM camera (without the typical MSSS stray light baffle) that will be very similar to the cameras built by MSSS for the CCRS vision system.
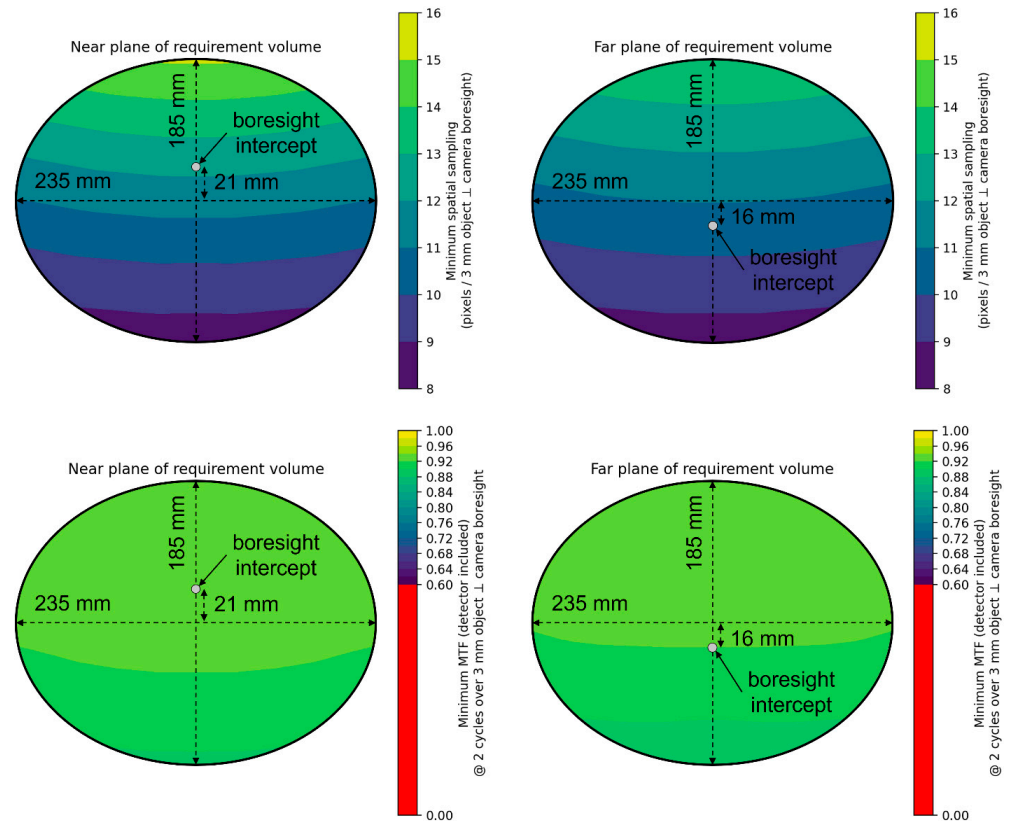

Figure 9. Ray trace model calculations of the detector sampling (**top row**) and the MTF values corresponding to two cycles across 3 mm (**bottom row**) at the two extreme depth-of-field planes for the selected vison system cameras. The calculations include optical as well as detector MTF effects. The results indicate that the cameras will have sufficient resolution and contrast to discriminate between features on the OS endcaps.

Table 2. Summary of the key CCRS vision system cameras' parameters.

Parameter	Value
Effective Focal Length (mm)	7.1
F/#	3.5
Best Focus Distance from First Lens Surface (mm)	493
Pixel Spacing (µm)	2.2
Pixel Scale/IFOV (mrad/pixel)	0.31
FOV (°)	45.6 (H) × 34.3 (V)
Entrance Pupil Diameter (mm)	2.0

Table 2. *Cont.*

Parameter	Value
Optical Transmission (%)	>80%
Optical Distortion (%)	<8%
Detector Type	CMOS
Detector	ON Semiconductor MT9P031
Array Size	2592 × 1944 image area (2752 × 2004 total)
Camera Head Power (W)	1.5 standby, 2.0 per camera
Maximum Frame Rate (FPS)	1
Quantization (bits/pixel)	12
Read Noise (e-)	7
Minimum Exposure Durations (ms)	0.1528 12-bit mode, 0.0764 8-bit mode
Maximum Exposure Duration (s)	30.7675
Full Well (e-)	5400
Data Interface (100 MHz output)	SpaceWire
Mass (kg)	0.5
Volume Allocation (mm)	120 (long) × 100 (diameter)
Power (W)	2

Figure 10. Image of a previously constructed Malin Space Science Systems (MSSS) ECAM camera that is identical to the CCRS vision system camera design.

Figure 11 shows a simplified block diagram of the interface between the CCRS avionics and the camera heads, while Figures 12 and 13 display more detail. We designed the electrical interface with EMI/EMC (electromagnetic interference/electromagnetic compatibility) concerns in mind. The camera chassis will be grounded to the CCRS structure and connected to power and data output shields while maintaining its own internal ground connected through an isolation provided by 11 and 22 MΩ resistors, respectively. The 15-pin camera connector will split into 9- and 6-pin harnesses (Figure 11) that feed as separate SpaceWire and power sensor links into the avionics. The 9-pin SpaceWire will follow a standard Type A format (pin 3 not connected), minimizing ground loops. The avionics will not connect to the integral camera temperature sensor. Instead, spacecraft-provided thermal sensors located at the camera interface will monitor camera temperatures. The cameras will meet all performance requirements over a temperature range of at least −30 °C to +40 °C. They can be powered on anywhere over a −40° to +55 °C temperature

range and survive indefinite exposure at temperatures ranging from −50° to +70 °C. Their peak power draw is 2.0 W, and they operate on a 5.0 V supply.
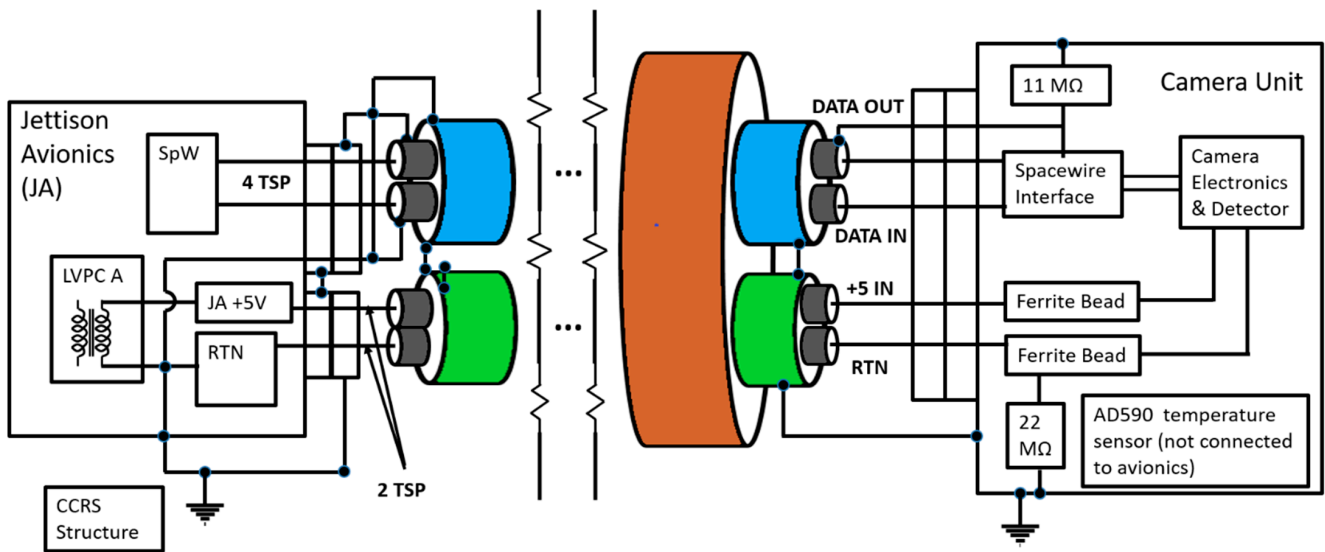

Figure 11. Simplified block diagram of the interface between the CCRS avionics assembly and the capture enclosure camera head. The key ground path is shown, including isolation of the camera electronics from chassis ground, which is connected to both the CCRS structure and the internal SpaceWire shields. The SpaceWire strobe signals are not explicitly shown (Acronyms: 1. TSP Twisted, shielded pair; 2. LVPC Low-Voltage Power Converter; 3. RTN Return; 4. JA Jettison Avionics; 5. CCRS Capture, Containment Return System; 6. SpW Spacewire; 7. AD590 Analog Devices 590 Temperature Sensor).
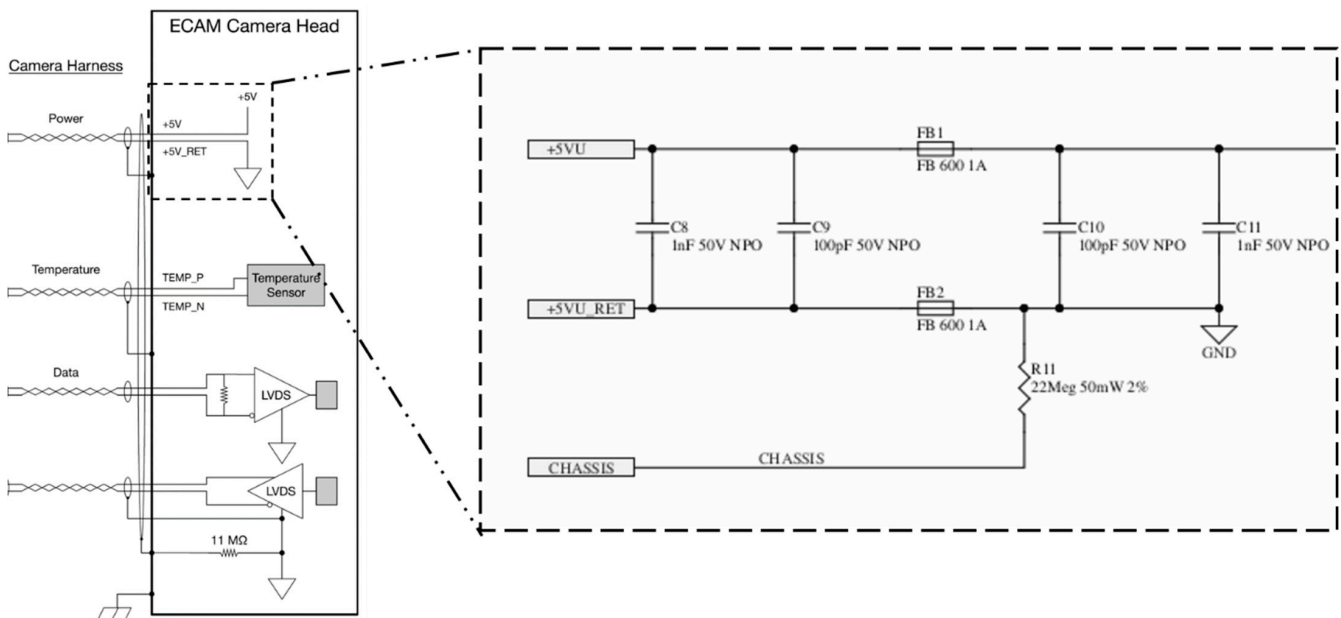

Figure 12. The camera head ground plane connected to a +5 V return through a Ferrite bead and isolated from the chassis ground by 11 MΩ resistance (dual 22 MΩ resistors in parallel). Chassis grounded to the CCRS structure. Chassis connected to SpaceWire outer shield and power inner shield.
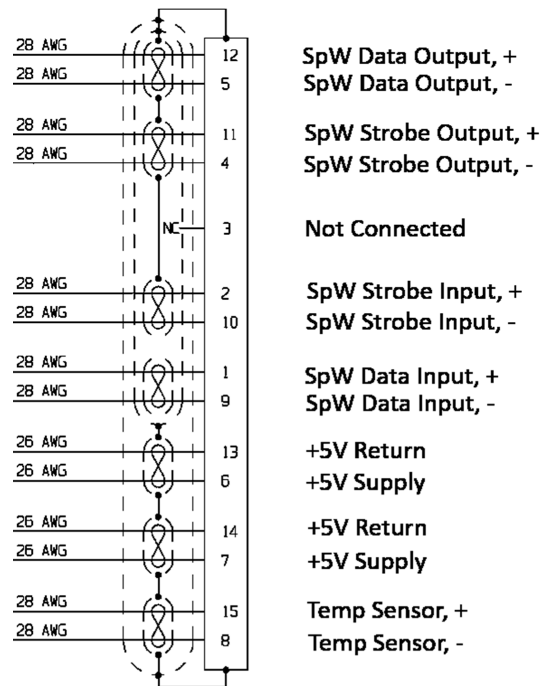
Figure 13. The camera 15-pin Micro-D Socket (M83513/01-BN) pinout shows the chassis ground connected to the power twisted pair harness internal shields; the chassis ground connected to the SpaceWire bundle shield and to strobe input and output twisted pair shields and data output twisted pair shield; data input twisted pair shield left isolated; Pin 3 not connected through harness following Spacewire Type A standard and temperature sensor also not connected through harness.

The ERO will utilize the same Electra communications system that has serviced robotic Mars missions for most of the 21st century. Existing orbiters that host this system can relay communications and aid navigation for robotic spacecraft—both those in orbit and stationed on the surface—facilitating mission success [11]. The four channels it employs—which operate around 400 MHz—fall on or near harmonics of the frequency of the capture enclosure cameras: 100 MHz (see Table 3). Electromagnetic compatibility (EMC) considerations require that these four bands receive additional scrutiny. Since it is possible that the MSSS cameras may not pass such a stringent notched test, we are likely to operationally mitigate the risk of interference by not operating the cameras during critical ERO communications.

Table 3. Radiated emissions, electric field, on-orbit, receiver notches planned for the capture enclosure camera prior to hardware delivery. The X-band test was recently added with the specific test parameters still to be determined (TBD) or revised (TBR) by the CCRS project.

Radiated Emission, On-Orbit, Receiver Notches			
Receiver	**Frequency Range (MHz)**	**Electric Field (dBμV/m)**	**Measurement Bandwidth**
ELECTRA Channel 0	401.585625 ± 2	-5	100 Hz
	401.585625 ± 0.1	-10	100 Hz
ELECTRA Channel 1	404.4 ± 2	-5	100 Hz
	404.4 ± 0.1	-10	100 Hz
ELECTRA Channel 2	391 ± 2	-5	100 Hz
	391 ± 0.1	-10	100 Hz
ELECTRA Channel 3	392 ± 2	-5	100 Hz
	392 ± 0.1	-10	100 Hz
X-Band	7145–7190	-26 (TBR)	TBD

4.2. Illumination System Description

The purpose of the illumination system is to illuminate the OS endcaps with light of an intensity range and uniformity that allows the vision system cameras to acquire high-quality OS endcap images in the absence of ambient sunlight. MSR programmatic constraints limit our ability to modify the OS optical properties and shape as well as most of the camera characteristics. This means the use of a custom illumination system is the best avenue to optimize the overall vision system performance.

4.2.1. Key Illumination System Requirements

Table 4 summarizes the key illumination system mass, electrical, thermal, structural and optical requirements. These requirements flow directly from the CCRS accommodations whereas the optical requirements flow from a consideration of the OS container optical properties, the size and geometry of the OS endcaps and the optical performance of the vision system cameras.

Table 4. Summary of the key illumination system requirements.

Description	Requirement	Required Value
Illuminance	At two specified planes, near and far planes, over a specified area	50 to 750 lux per module
Illumination Uniformity	Luminance variation over defined local Illumination zones	<5% over a 10mm diameter zone
Electrical	Operating voltage range and power consumption	25.7 to 28.2 V <7 W
	Maximum derated operating current (75% derating)	375 mA
Thermal	Survival temp (protoflight qualification)	$-40°$ to 55 °C
	Operation temp (allowable flight temp)	$-30°$ to 45 °C
	Maximum derated LED junction temp	95 °C (after 40 °C derating)
	Maximum thermal dissipation per module	5 W
Mass	Maximum mass per module	100 g
Stiffness	Minimum frequency	100 Hz

Both of the OS endcaps exhibit complex topography with a variety of local surface slopes and distinguishing features located at a variety of depths. Simplified optical requirements for the illumination system were developed through a series of first-order hand calculations and then progressively more elaborate optical test and modeling activities as we describe later in Section 5. We have found through this process that we can adequately specify the light pattern generated by the illumination system using two relatively simple optical criteria that apply at near and far illumination areas. The first requires the illuminance over the defined illumination areas to fall within 50–750 lux while the second requires an illumination uniformity of 5% or better within any 10 mm diameter circle located within the same illumination area.

The illumination area sizes and locations are calculated by considering the maximum OS dimensions, CCRS capture location uncertainties, CCRS capture orientation uncertainties and the illumination system design, fabrication, assembly and installation tolerances. By oversizing the illumination areas to consider all of these effects we ensure that even for a worst-case stack-up of errors, sufficient light with the necessary uniformity will illuminate the OS endcaps. In addition, to ease the verification process, we have orientated these illumination areas such that each surface normal is parallel to the illumination system mechanical interface surface normal. More detail regarding the geometry of the illumination areas will be provided in the optical design description in Section 4.2.5.

4.2.2. LED Characteristics and Performance

Previous spaceflight experience with LED illumination arrays [6,7] motivated us to design the CCRS illumination system using the same technology. Our review of the literature led us to consider LEDs from Nichia (Tokushima, Japan) and Lumileds (San Jose, CA, USA). We ultimately selected a white-light LED, LXZ1-4070, from the Lumileds corporation due to its high optical efficiency, small size (~1.7 mm × 1.3 mm × 0.59 mm), operational temperature range (−40 °C to 135 °C) and its Mars Perseverance rover heritage [12]. To facilitate LED performance verification and flight qualification, we ultimately purchased 1000 units on a single order. Before developing the final illumination system design, we completed a series of LED characterization tests to validate the vendor's published specifications and performance.

Our initial test investigated LED performance and survivability over temperature using Lumileds' LXZ1-PM01 green and LXZ1-4070 white LEDs. The four-day test evaluated three green LEDs and four white LEDs over a temperature range of −70° to 65 °C within an environmental test chamber. To maintain a balance between test duration and temperatures tested, we utilized several different temperature step sizes: 2°, 5° and 10 °C depending on the temperature. The smaller step sizes (2° and 5°) were used at the temperature extremes (e.g., 2 °C step sizes were used from −50° to −70 °C) to more carefully test performance at the temperatures more likely to cause LED failures. At fixed temperature points we performed current sweeps, ranging from 10 mA to a maximum of 500 mA when the test temperature was below 0 °C or 10 mA to a maximum of 1000 mA when the temperature was above 0 °C. We measured the illuminance variation with changes in current and temperature using a photometer located outside the environmental chamber at a fixed distance. Every day, we acquired baseline illuminance measurements at 20 °C to check the consistency of the set up and LEDs.

Figures 14 and 15 illustrate the variations in the electrical and optical behavior of the LEDs with temperature. For instance, there is an approximate 6.7% decrease in voltage when the temperature increases from −70 to 65 °C, exhibiting a roughly linear trend with temperature. Additionally, at lower operating currents, the changes in radiance are relatively mild. However, at higher currents, such as 500 mA, the illuminance varies by approximately 17.1% with temperature, even at the same current.
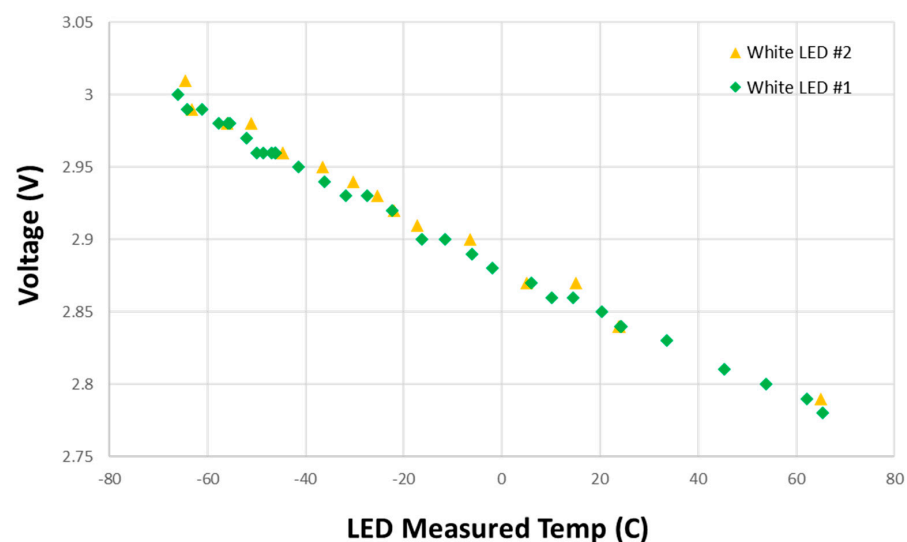

Figure 14. LED variation of voltage with temperature from −70 °C to 65 °C at a constant current of 300 mA for LXZ1-4070 LED manufactured by Lumileds (San Jose, CA, USA).
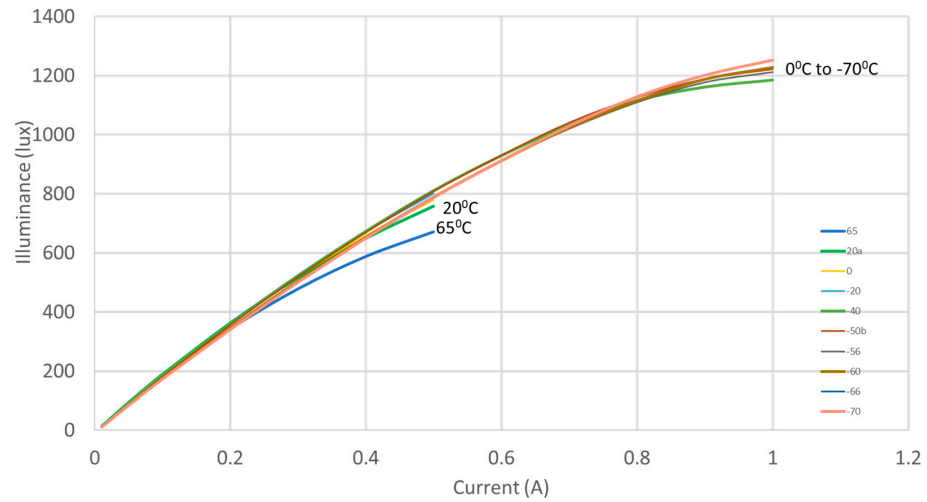
Figure 15. Changes in LED illuminance with current sweeps ranging from 10 mA to either 500 mA or 1000 mA across a temperature range from −70 °C to +65 °C.

During a follow-up LED test, we measured the LED electro-optical efficiency at various temperatures. This test was specifically tailored to provide data for our illumination system thermal model and used the Lumileds LXZ1-4070 white-light LED selected for the final design.

The LED efficiency evaluation measured the electrical power consumption of six LEDs at −40 °C, 25 °C and up to 55 °C, which covers the CCRS illumination system operational temperature range as well as typical room temperature. The LEDs were driven with currents ranging from 5 mA to 500 mA, increasing in steps of 5 mA up to 10 mA and then in 50 mA increments thereafter. At each step, we captured all the visible light emitted from each LED using an integrating sphere optically coupled to a calibrated spectrometer to measure the optical power. By comparing the light power output with the electrical power input, we quantified the efficiency at each operational temperature and each prescribed current. We observe that light efficiency generally decreases with an increase in operating current and temperature (see Figure 16). We attribute the variation in light efficiency at current levels below 50 mA (observed in the initial part of the curve) to noise-induced inaccuracies in the light power and voltage measurements. Among the six LEDs tested, the worst case showed a light efficiency of 36.2% at 150 mA and 55 °C. Based on this result we used a conservative LED light efficiency of 36% in our final thermal design and simulations.

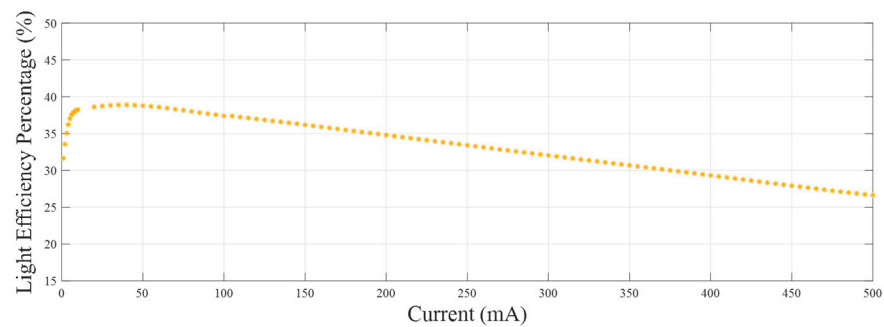**Figure 16.** Variation of LED light efficiency versus current at 55 °C for the least efficient LED among the six LEDs tested. This represents a worst-case scenario estimation of light power, thereby providing insight into the maximum potential thermal dissipation for our illumination system.

An assessment of the LXZ1-4070 LED's construction and the CCRS spaceflight radiation environment motivated us to complete a series of proton radiation tests at the Crocker Nuclear Laboratory (University of California—Davis). Constructed from InGaN (indium gallium nitride) with a phosphor coating and shielded by a thin silicone layer, the LXZ1-

4070's primary vulnerability to radiation is expected to be performance degradation due to the total non-ionizing dose (TNID). Radiation modeling predicts a maximum cumulative dose of approximately 7 krad (Si). To provide a margin, we exposed the LED test articles up to 61.1 krad.

We prepared 84 LEDs for the radiation test. They were mounted to six printed circuit boards (PCB) (each holding 14 LEDs) using standard manufacturing techniques. Four PCBs were irradiated while two PCBs were maintained as unexposed control samples. The irradiated PCBs were exposed to increasingly higher doses of radiation throughout the test. Two boards were exposed to three different doses while the other two were exposed to four. Table 5 shows the test details. Prior to and after each irradiation step at room temperature, we conducted on-site electrical characterizations, including current sweeps from 0 mA to 160 mA in 10 mA increments and voltage measurements, along with optical characterizations such as spectrum and illuminance measurements at fixed currents of 30 mA and 150 mA to prevent over or under illumination. The unirradiated control PCBs underwent the same evaluations at each dose step. Post-irradiation measurements were carried out in an unbiased manner (after board cooling) to prevent annealing of total dose effects that could arise from device heating during proton exposure. Off-site we also performed more accurate pre- and post-radiation exposure optical measurements using a stable test set-up with a validated relative illuminance repeatability uncertainty of ~3% or better. Our assessment of the test results is that even at a total dosage significantly greater than expected in flight (61.1 krad versus 7 krad) the change in LED optical performance is within the measurement noise (see Figure 17).

Table 5. Radiation dosage exposures for individual test PCBs. The control PCBs, unexposed to radiation, were evaluated at the same intervals as the test PCBs to account for systematic variables, including environmental temperature variation and measurement repeatability. This ensures accurate comparison between irradiated and unirradiated conditions.

|	Radiation Test Dosage Summary (DDD = Displacement Damage Dose; TID = Total Ionizing Dose)				
PCB No.	**Round 0** DDD (InGaN) [MeV/g]; 64 MeV Proton Eq. Fluence [cm^{-2}]; TID (Si) [krad(Si)]; DDD (Si) [MeV/g]	**Round 1** DDD (InGaN) [MeV/g]; 64 MeV Proton Eq. Fluence [cm^{-2}]; TID (Si) [krad(Si)]; DDD (Si) [MeV/g]	**Round 2** DDD (InGaN) [MeV/g]; 64 MeV Proton Eq. Fluence [cm^{-2}]; TID (Si) [krad(Si)]; DDD (Si) [MeV/g]	**Round 3** DDD (InGaN) [MeV/g]; 64 MeV Proton Eq. Fluence [cm^{-2}]; TID (Si) [krad(Si)]; DDD (Si) [MeV/g]	**Round 4** DDD (InGaN) [MeV/g]; 64 MeV Proton Eq. Fluence [cm^{-2}]; TID (Si) [krad(Si)]; DDD (Si) [MeV/g]
SN005	0 0 0 0	0 0 0 0	0 0 0 0	0 0 0 0	0 0 0 0
SN004	0 0 0 0	7.16×10^7 2.10×10^{10} 2.8 8.13×10^7	1.43×10^8 4.20×10^{10} 5.5 1.63×10^8	2.87×10^8 8.39×10^{10} 11.0 3.25×10^8	n/a n/a n/a n/a
SN021	0 0 0 0	1.43×10^8 4.20×10^{10} 5.5 1.63×10^8	2.87×10^8 8.39×10^{10} 11.0 3.25×10^8	5.73×10^8 1.68×10^{11} 22.0 6.51×10^8	n/a n/a n/a n/a
SN002	0 0 0 0	0 0 0 0	0 0 0 0	0 0 0 0	0 0 0 0
SN010	0 0 0 0	1.43×10^8 4.20×10^{10} 5.5 1.63×10^8	2.87×10^8 8.39×10^{10} 11.0 3.25×10^8	5.73×10^8 1.68×10^{11} 22.0 6.51×10^8	7.95×10^8 2.33×10^{11} 30.5 9.03×10^8
SN025	0 0 0 0	2.87×10^8 8.39×10^{10} 11.0 3.25×10^8	5.73×10^8 1.68×10^{11} 22.0 6.51×10^8	7.95×10^8 2.33×10^{11} 30.5 9.03×10^8	1.59×10^9 4.66×10^{11} 61.1 1.81×10^9

(**a**)

(**b**)
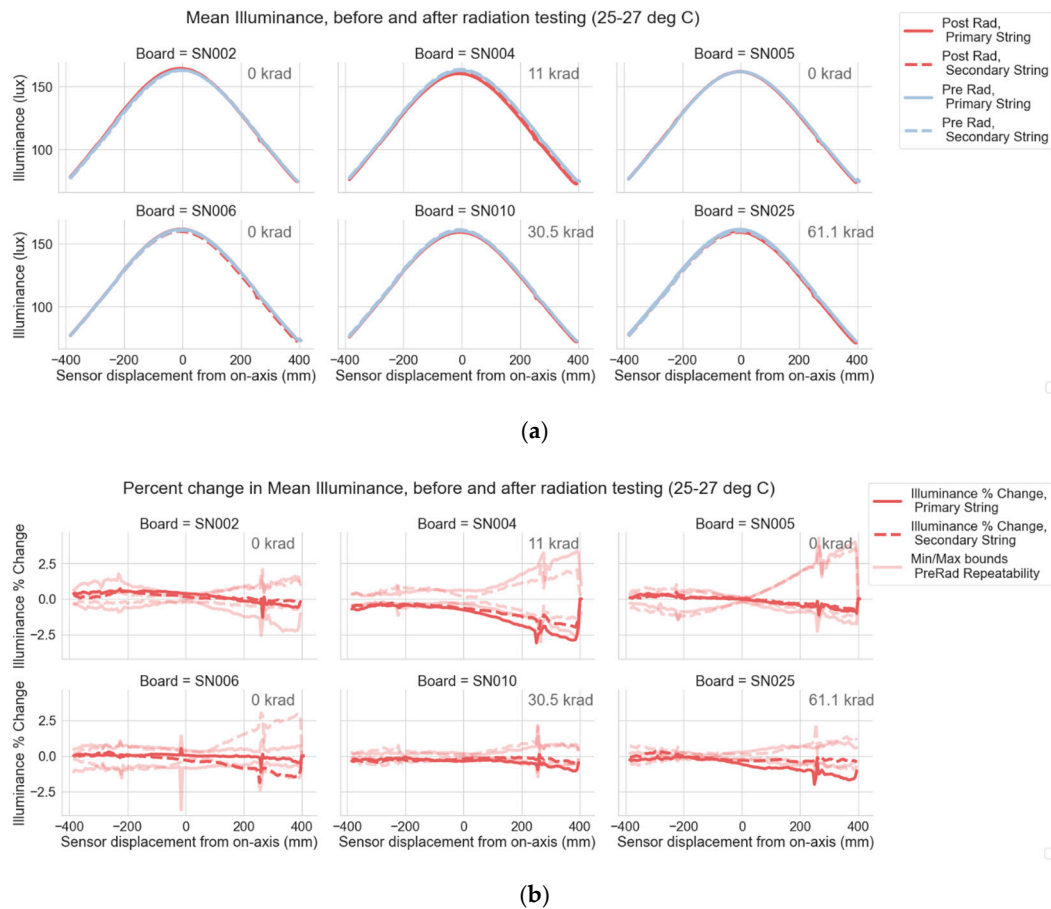
Figure 17. Pre- and post-radiation test optical characterization for LEDs exposed to various radiation dosages. No discernible changes were observed in the measured LED illumination patterns (**a**). The illuminance percent change data (**b**) indicate that optical degradation due to radiation exposure was within the measurement noise—not exceeding 3% even under the most pessimistic assumptions.

4.2.3. Electrical Design

The nominal voltage required to operate a single LXZ1-4070 LED is 2.8 V while the voltage interface supplied by the CCRS varies from 25 to 28 V. To determine the optimum number of LEDs to connect in series for our application, we constructed an opto-electrical model consisting of various numbers of LEDs and resistor values. This model includes the temperature-dependance of the LED current–voltage behavior using coefficients we derived from our LED thermal tests. The model predicts that to keep the highest minimum optical output at either end of the operational temperature range requires seven or eight LEDs when wired in series. In addition, the model predicts that the variation in total luminance across our operational temperature range is minimized when seven LEDs are in series. Seven LEDs are predicted to generate ~150 lux at the required range under our operational conditions, providing a significant margin against the 50-lux requirement. Based on these considerations, we based the illumination system on sets of seven LEDs wired in series.

Connecting seven LEDs in series to our CCRS electrical interface requires additional resistance in the circuit. We considered several constraints when selecting resistors including the following: the resistor's size, the power rating, the total thermal dissipation and availability as a flight-certified component. Due to the limited illumination system mass allowance we aimed to minimize the resistor size without compromising functionality. We settled on a resistor size of 5.0 mm × 2.5 mm. Resistors of this size typically have a maximum power rating of 1 W. Adhering to the standard 80% derating rule in flight design, we opted for three 2010-sized resistors instead of one larger resistor, which would

have either significantly increased the size or compromised the power rating. The use of three resistors wired in series also provides flexibility in resistor placement on the PCB, allowing each resistor's position to be optimized. To meet our thermal dissipation requirements (including the 15% thermal margin design guideline followed by NASA's Goddard Space Flight Center flight) we chose three 28 Ω 800 mW resistors (#M55342K08B28D0SS6) supplied by Vishay Intertechnology (Malvern, PA, USA) for the flight design.

With the opto-electrical optimization complete, we focused our efforts on determining how many seven LED circuits the vision system would require and CCRS could support. We found through test and analyses that the camera and illumination system positions that are preferred from a CCRS systems perspective require only one set of seven LEDs to properly illuminate the OS (for either camera) and do not require separate or dedicated illumination modules. Furthermore, failure mode analyses indicated that the most redundant illumination system design for the CCRS configuration is achieved when two, seven-LED circuits are connected in parallel to one CCRS power switch, and each set of seven LEDs connected in series is mounted to a completely different mechanical component. The CCRS provides two switches to the illumination system, both of which provide enough power (7 W maximum) to accommodate a circuit of 14 LEDs wired in parallel. To take advantage of this and maximize the illumination system's fault tolerance, we chose an illumination system architecture consisting of two illumination modules. Each module contains 14 LEDs with a primary circuit of seven LEDs connected in series to the primary switch and a backup circuit of seven LEDS connected in series to the secondary switch. Each set of seven LEDs is connected in parallel to a set of corresponding seven LEDs in the other module. This electrical and mechanical arrangement can absorb >20 different single and compound failures without compromising the vision system performance.

Both of the illumination system's modules are electrically connected to the CCRS avionics with two-meter-long, 28 AWG (American wire gauge), jacketed-pair wires with flying leads. The electrical diagram for a single illumination module is shown in Figure 18.
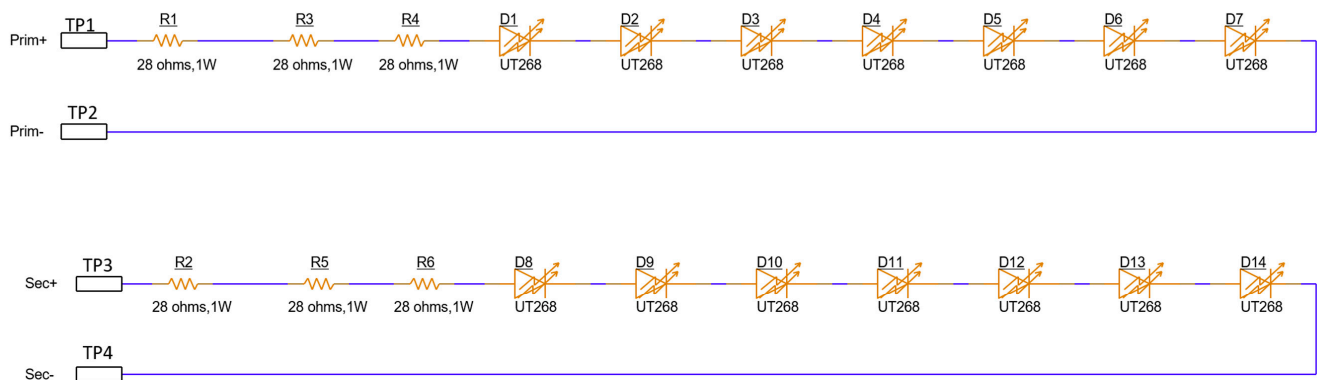

Figure 18. Electrical diagram for a single illumination module, constructed from two independent circuits. Each circuit contains seven LEDs (LXZ1-4070) and three resistors (2010 size, 800 mW Power Rating, sourced from Vishay Intertechnology).

4.2.4. Printed Circuit Board Design

The printed circuit board (PCB) design was driven by electrical, mechanical and thermal requirements. The board components include six resistors in a 2010 package, 14 LEDs and four wire pads. All parts are mounted within the 30.5 mm diameter board area.

Thermal requirements drove us to construct the board with an aluminum core to quickly dissipate heat and maintain the PCB temperature range to not exceed the component specifications. All parts are located on one side of a single layer, Arlon 85HP laminate sheet. The 2.5 mm thick, 6061-T6 aluminum core adheres to the back side by a prepreg sheet material. The laminate-over-metal core construction provides optimal thermal transfer to the board interface.

We performed analyses on the PCB design that included electrical, stress and thermal analyses. All analysis results show that the PCB meets all requirements with margin. Figure 19 shows the front and back PCB design for the CCRS illumination system.
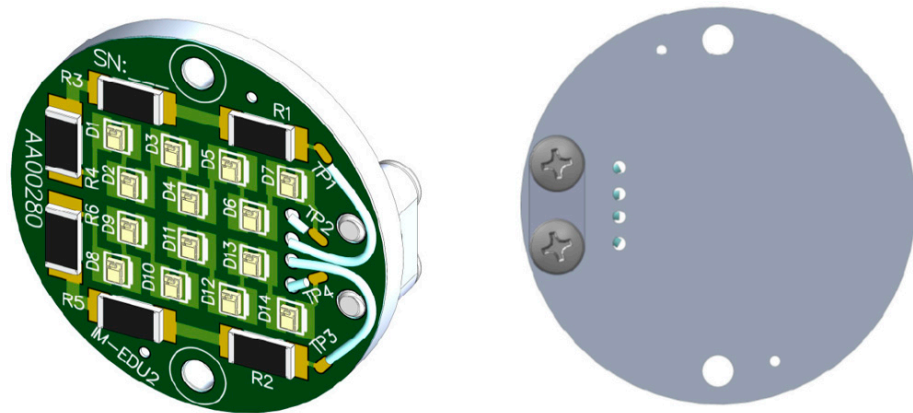

Figure 19. Front and back surfaces of the illumination system PCB design.

4.2.5. Optical Design

Due to the ample electrical power provided by the CCRS, we determined early during the vision system development phase that powered optics would not be necessary to meet the required illuminance levels. In addition, due to the distances between the captured OS and the available illumination system mounting locations, we found that powered optics would not be needed to shape a uniform light pattern over the required areas. These two conclusions, along with the significant mass savings, fabrication and assembly simplicity and schedule considerations, drove us to only explore optical designs that provided direct illumination of the required areas with the LEDs. For a direct illumination architecture, the two most important optical design considerations are the LED locations and the component mechanical obscurations.

We previously described in Section 4.2.3 how we found a seven-LED arrangement to be optimum from an electrical perspective. For the CCRS illumination range and geometry, the most optimum LED arrangement from an optical perspective is one where both the primary and redundant set of LEDs are tightly clustered together and uniformly distributed around a central point. Our initial designs used this approach until we discovered during the first EDU fabrication effort (see Section 4.2.9) that this design was susceptible to developing electrical shorts. To remedy this in the flight design, we have selected a slightly non-optimal LED arrangement from an optical perspective but one that significantly reduces the likelihood of manufacturing defects and the need for rework of the flight units.

To protect the LED PCBs during CCRS integration and to better control the emitted light, each illumination module includes an integrated baffle. The baffle is designed so that it is the only illumination module component that obscures the light pattern emitted into the CCRS interior and exterior. We also found through test and analyses that we could slightly increase the overall light level and improve the uniformity over the illumination zones if we made the baffle interior optically diffuse (see Section 4.2.9).

The final location and volume allocation for the vision system cameras within the CCRS do not provide enough space to include the highly effective stray light baffles that MSSS typically includes with their ECAM flight cameras [8–10]. Although we have not discovered any significant illumination-module-to-camera scattered light paths caused by the CCRS hardware, we have designed the illumination module baffle to accomplish the following: minimize the light that directly illuminates the CCRS components outside of the required area while maximizing the illumination uniformity.

For the flight CCRS illumination system, there are two illumination areas (a near and a far area) defined for each of the two illumination modules over which the optical requirements must be met. The emission areas for both the primary and redundant LEDs

are shown in Figure 20. The baffle design needs to provide illumination that meets the uniformity requirement within each illumination area for both the primary and redundant LEDs. To accomplish this, both sets of LEDs are considered during the baffle design process. We simplify the baffle design and manufacturing process by creating a rectangle that circumscribes the emitting area of all 14 LEDs on a single PCB. Additional clearance to the LED emission area is added on one side of the rectangle to prevent interference between one of the illumination modules' baffle petals and the CCRS capture cone. We designed the baffle using only the near requirement area (located 677 mm away from the LED emission area) due to it being more constraining. We then project the emission rectangle onto the elliptical boundaries of the nearest distant illumination area and use the "Lofted Cut" feature in the CAD tool SolidWorks to determine where the projected rectangular area intersects a cylinder centered on the PCB. The intersecting areas on the cylinder are then removed. We retain the remaining portions of the cylinder to define the baffle shape to provide a clear, unobscured line-of-sight for each LED to every location within the elliptical illumination area. This creates the maximum illumination uniformity within the illumination area for the given LED arrangement—identical to the uniformity that would be achieved in the absence of a baffle. For overall manufacturability the $+Z$ and $-Z$ illumination module, PCBs and bases are identical to each other and do not have mirror symmetry. For this reason, the optimum baffle aperture shapes are slightly different between the two modules (see Figure 21).
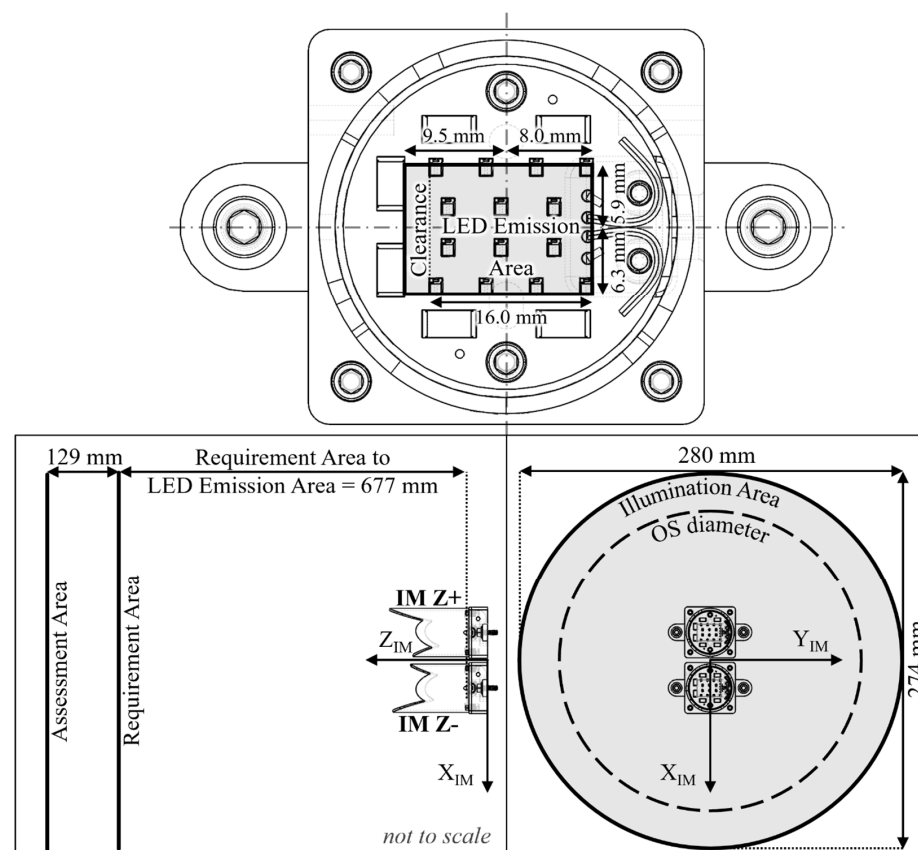

Figure 20. Illustration of the illumination module illumination areas over which the illuminance and uniformity requirements are to be met to ensure visibility of the OS endcaps (bottom). The illumination module baffle was designed using the near requirement area (located 677 mm away from the LED emission area) due to its being the most constraining. An oversized rectangle surrounding the 14 LEDs was used to represent the LED emission area in the design. Additional clearance to the LED emission area was added to one side of the rectangle to eliminate mechanical interference between one of the illumination modules' baffle petals and the CCRS capture cone.
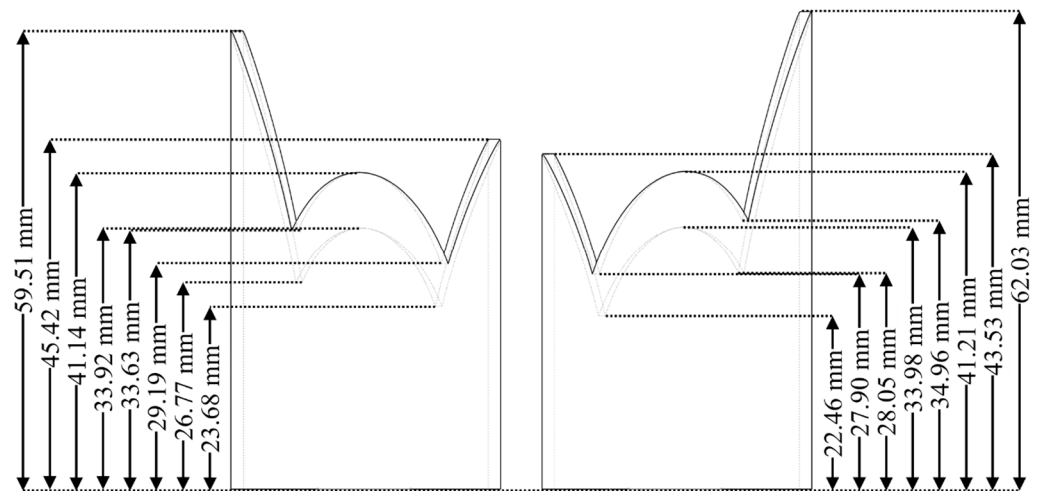
Figure 21. Illumination module baffle designs for the −Z (**left**) and +Z (**right**) illumination modules that maximize the light uniformity in the required illumination areas but minimize the light that strikes other areas. Dimensions indicate the distances between the LED emission plane and the baffle aperture minima and maxima dimensions.

Ray trace analyses indicate the baffle petals block 85% of the unwanted LED emission that would otherwise illuminate the CCRS interior if an elliptical baffle opening was used with a height set to provide the same level of illumination uniformity.

4.2.6. Mechanical Design

The illumination module mechanical components have two primary purposes: secure the LED PCBs in place with respect to the CCRS capture enclosure brackets and the captured OS and provide a light baffle that minimizes stray light while maximizing illumination uniformity (see the optical design described in the previous section). We chose to meet the illumination system optical performance and redundancy goals within the CCRS accommodations by mounting two illumination modules in close proximity to each other (when installed on the CCRS, the module bases are separated by only 3.5 mm). The primary illumination module constraints are a 100 g-per-module mass limit and a maximum volume allocation of 40 mm × 65 mm × 80 mm per module.

The illumination module mechanical components are constructed from aluminum 6061-T6. To optimize the optical performance, the baffle interior is first bead blasted per MIL-STD-1504 [13] at 30 psi using Ballotini glass beads per MIL-PRF-9954D, MG-9 (125–180 grit size) [14]. Then, the interior is coated in clear anodize Type III, Class 1 per MIL-A-8625 [15]. The exterior surfaces of the baffle and base are finished with black anodize Type III, Class 2 per MIL-A-8625 [15] for thermal and optical considerations. Finally, the bottom surface of the baffle, the top and bottom surfaces of the base and the mounting holes of the base use a chemical film Type I Class 3 coating per MIL-DTL-5541 [16] to provide a sufficient electrical ground path. Two threaded holes surrounded by the same chemical film coating are included on the base to add a grounding lug should another electrical ground path be needed. The final mechanical design is shown in Figures 22 and 23.
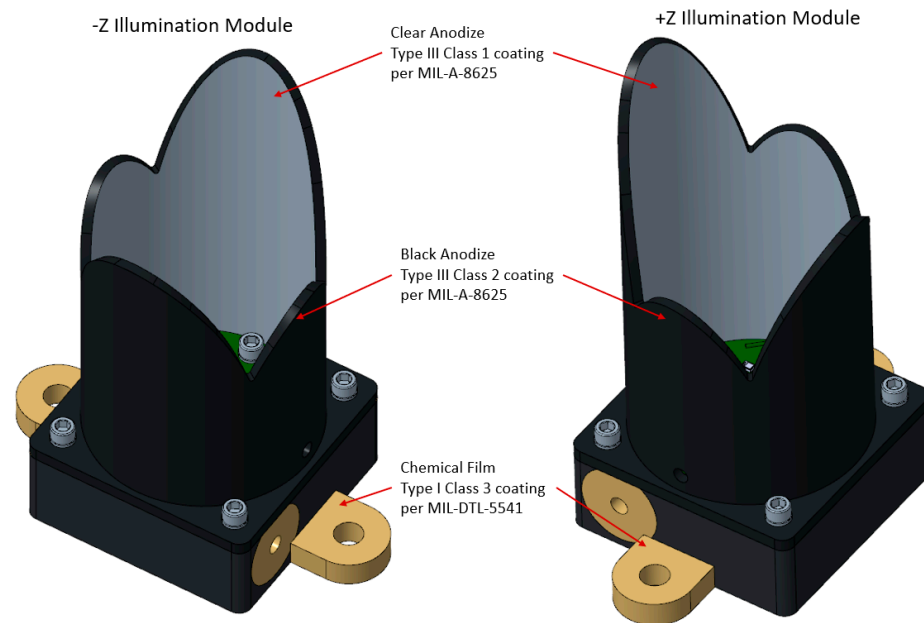
Figure 22. Mechanical design with coating specifications, showing two unique baffle designs and one common base design for each module.
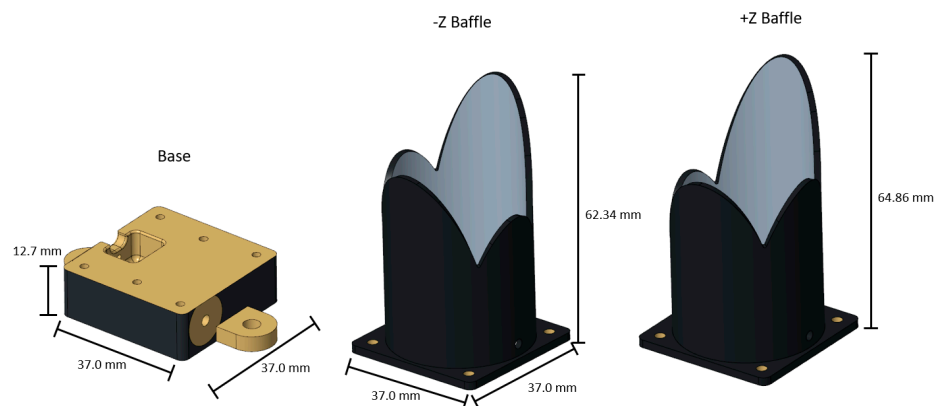

Figure 23. Overall dimensions of the illumination modules.

4.2.7. Thermal Model and Analysis

We constructed a thermal model to confirm the illumination modules' performance over the required $-30°$ to $45\,°C$ operational temperature range with a maximum power dissipation of 5 W per module when all 14 LEDs are powered on. Derating guidelines for the illumination module electrical components require, during electrical operation, that the LED junction temperatures remain below $95\,°C$ and that the resistors remain below $70\,°C$.

Several modeling assumptions were made to represent the worst-case thermal scenario accurately. We set the boundary conditions to $45\,°C$ steady state, with no radiative loss considered. Each seven-LED circuit was designed to have a maximum thermal dissipation of 2.5 W. This was distributed between the LEDs and resistors and included an additional 15% thermal simulation margin. Specifically, by factoring in the 36% optical efficiency (Section 4.2.2) and 15% margin, the seven LEDs connected in series dissipated a total of 1.58 W while the resistors dissipated 1.3 W by including the same simulation margin. For the LED thermal resistance, we used $6\,°C/W$ per the Lumileds data sheet. The PCB-to-base bolted contacts' thermal conductance values came from Table 8.4 of the Spacecraft Thermal Control Handbook [17]. For the thermal interface materials, the eGRAF HiTherm (Lakewood, Ohio) was assumed to have a 0.254 mm thickness and a conservative 50% areal coverage between the PCB and base. Based on this and NASA Goddard Space Flight

Center experience, the interface conductance was assumed to be 0.33 mW/mm²/°C. From the illumination module base to the thermal model boundary, we assumed a 3.81 mm thick Cho-Therm 1671 (Parker Hannifin, Woburn, MA, USA) layer with a conservative 10% areal coverage. For the thermal contact between the LEDs, resistors and their respective copper pads, we assumed a 0.381 mm thickness and 50% areal coverage.

Figure 24 displays the thermal simulation's results, showing the temperature distribution within the illumination module. The simulation predicts a maximum resistor temperature of 66.61 °C and a maximum LED junction temperature of 68.27 °C—indicating a safety margin of 3.39 °C below the 70 °C derated temperature for the resistors and a 26.73 °C safety margin for the LEDs' 95 °C derated junction temperature. The analysis confirms that even with a 15% thermal dissipation margin, the illumination modules meet the component thermal specifications at a boundary temperature of 45 °C.
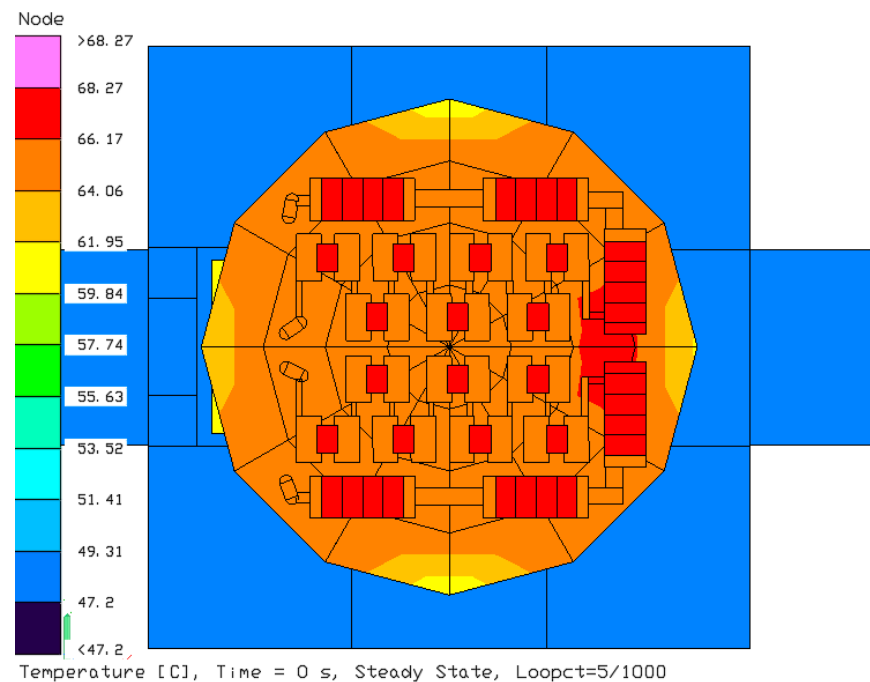

Figure 24. Thermal model simulation results showing the LED junction and resistor temperatures meet the component specifications with margin.

4.2.8. Structural Analysis

To assess structural performance, we created a finite element model (FEM) of the illumination module using three-dimensional (3D) solid elements for the structure and two-dimensional (2D) laminate elements for the LED board. Fixed boundary conditions were then applied at the two #6 fastener holes at the base of the housing. Aluminum 6061-T6 was the material used for the baffle and base, copper and Arlon 85HP laminate for the LED board and Cho-Therm for the thermal interface material. The FEM mass was 74 g and consisted of ~62,000 elements.

A quasistatic load of 70 G was applied to the FEM, with the load applied independently in each of the three primary axes. The analysis produced a maximum stress of 14 MPa, less than 10% of the yield strength (241 MPa) of aluminum 6061-T6. The other materials showed similarly low stresses. We also completed a modal analysis run on the FEM which predicted a 1st mode of 2723 Hz, well above the flight requirement of 100 Hz. Based on these results, the illumination module structure is deemed suitable for flight loads.

4.2.9. Engineering Development Unit Fabrication and Testing

To develop manufacturing experience and validate our illumination system design and analyses, we completed two rounds of engineering development unit (EDU) fabrication and

testing. The first set of EDU units were built from a preliminary illumination module design and went through a series of environmental tests as well as pre- and post-environmental optical characterization tests. We built a second set of EDU units from the flight design and had them optically tested. Depending on future MSR programmatic decisions, the second set of EDU units may also go through an environmental test campaign that will be identical to the flight model qualification as a risk-reduction activity.

For the first EDU campaign, we constructed and tested six complete illumination modules (during that phase of development, both illumination modules were identical in design). Test facility schedule constraints dictated that the vibration test would have to follow the thermal vacuum testing.

The thermal vacuum test was performed in a Dynavac chamber (Hingham, Massachusetts), chamber GES343, at Genesis Engineering Solutions (Lanham, MD, USA). We evacuated the chamber to 10-7 Torr and varied the thermal shroud temperature from −170 °C to +150 °C. Type T thermocouple sensors measured temperatures at various locations within the chamber and mounting plate. Each of the six illumination modules had thermocouples attached to their LED boards while two of those six modules also had thermocouples attached to their bases. Temperature measurements were logged using the facility's data acquisition system while chamber data were logged using a LabVIEW VI application.

The thermal vacuum test consisted of nine phases, starting with Phase A at an ambient pressure of 10-5 Torr where an illumination module time constant and a full current sweep were conducted. Phase B ramped the temperature to a hot survival limit of 55 °C at a rate of <2 °C/minute, followed by a four-hour dwell in Phase C and operational checks in Phase D. Phases E through G focused on the transit to the cold survival temperature and operational checks at −40 °C. Phase H transitioned back to ambient temperature, and Phase I consisted of a final functional check at ambient conditions (see Figure 25). These tests confirmed the illumination modules' ability to withstand both hot (55 °C) and cold (−40 °C) extremes, characterized illumination modules' performance over operational temperatures and verified LED functionality throughout the expected operational conditions. Figure 26 shows the thermal vacuum chamber test set up.
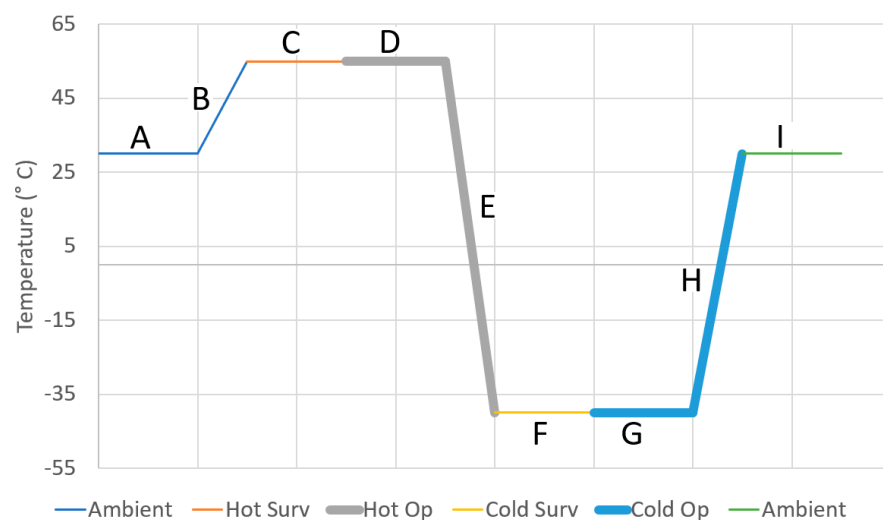

Figure 25. Graphical representation of the EDU illumination module thermal vacuum test temperature profile. Section A is the initial ambient condition. Section B is the ramp up to the hot survival temperature. Section C is the hot survival test. Sections D and E are the hot operational and ramp-down operational tests. Section F is the cold survivability test. Sections G and H are the cold operational and ramp-up tests and Section I is the final ambient test condition.
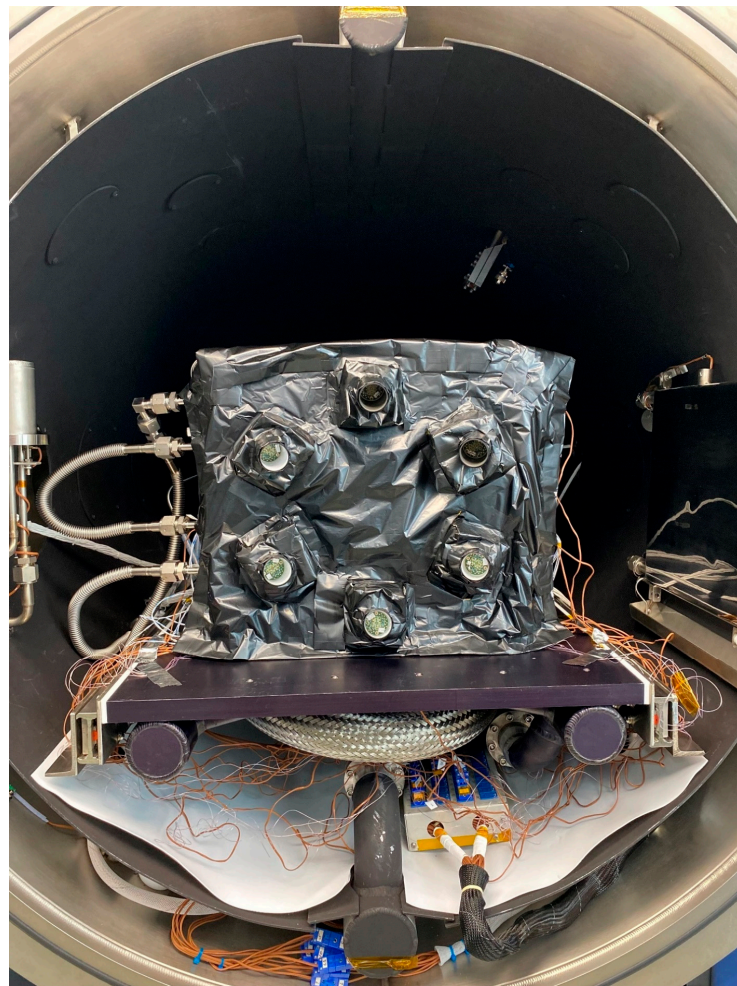
Figure 26. EDU illumination module thermal vacuum test set-up prior to chamber door closure. Six test articles are visible with views of the PCBs looking along the baffle interiors.

The illumination module vibration tests were conducted using the vibration table M5044A-PA155 at Genesis Engineering Solutions. These tests were preceded with a bare table sine sweep to ensure the correct setup of the testing apparatus and the integrity of the accelerometer installation.

Following this initial step, the test protocol proceeded in a systematic manner for each of the three orthogonal axes. For each axis, the sequence started with a pre-test sine sweep, ranging from 20 to 2000 Hz at an acceleration of 0.25 g. This established a baseline profile for the respective axis. Subsequently, the modules underwent a random vibration test at four distinct intensity levels: 0 dB (the reference level), −3 dB, −6 dB and −12 dB. After completing the random vibration tests for a particular axis, a post-test sine sweep was conducted for that same axis. This step was to detect any significant shifts in natural frequency. This protocol was repeated for each of the three orthogonal axes to ensure a comprehensive evaluation of the modules' structural integrity and resilience under various vibrational conditions. Figure 27 shows the vibration test set up.
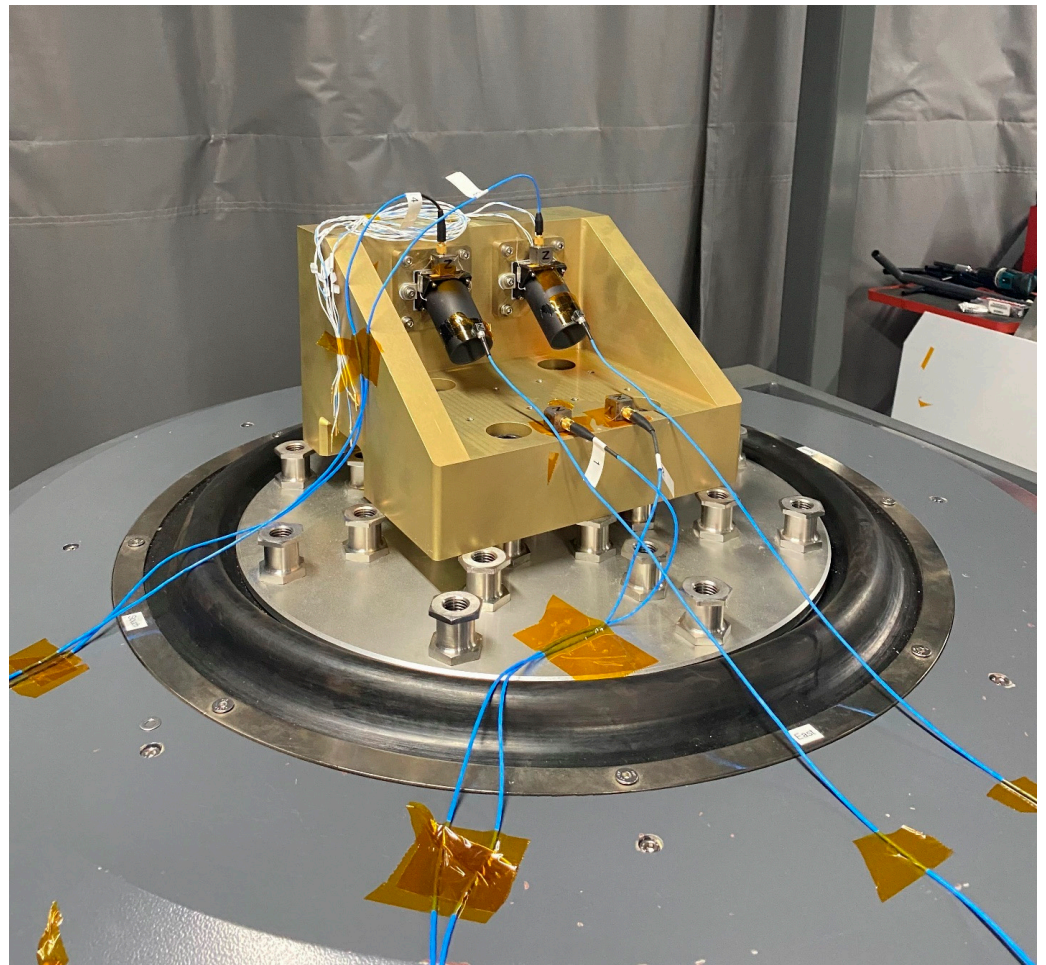
Figure 27. EDU illumination module vibration test arrangement. This set up allowed two illumination modules to be tested at the same time.

The environmental test campaign caused no LED failures during the thermal vacuum or vibration tests and caused no statistically significant shifts in component natural frequency. Voltage changes pre- and post-environmental testing were within 1.6% across all six modules (84 LEDs total, two sets of seven LEDs wired in series per module, six modules), and luminance changes were within the optical test set-up repeatability of 2–3%. These results confirm the system's robustness and reliability.

As part of the first EDU investigation, we evaluated the optical performance of two types of interior coatings with the six EDU units: bead blasted with clear anodization, known for its diffuse scattering properties, and A276 Aeroglaze, which provides a more specular scattering surface. The EDU optical testing showed that the diffuse coating achieved superior overall uniformity across a larger area for our baffle design. Based on these results, we chose the bead-blasted, clear anodized coating for the interior of the illumination module baffles for the flight design as well as the units fabricated for the second EDU campaign.

In addition to the valuable performance information provided by the EDU campaigns, the illumination module fabrication and assembly lessons that were learned also impacted the flight model design. For instance, for our printed circuit board (PCB) fabrication and assembly processes, we discovered that mounting the LEDs and resistors on the opposite side of the PCB increased the chances of creating an electrical short due to the resistor soldering process. We corrected this for the flight design and the second EDU units by mounting the LEDs and resistors on the same side of the PCB. We also found with the first set of EDU units that we were too aggressive with the LED pad spacing by not leaving

adequate margin to protect against solder bridges that cause LED electrical shorts. We corrected this in the flight design and the second set of EDU units by increasing the pad spacing from 254 μm to 330 μm. See Figure 28 for an illustration of the changes made between our initial design and the flight model.
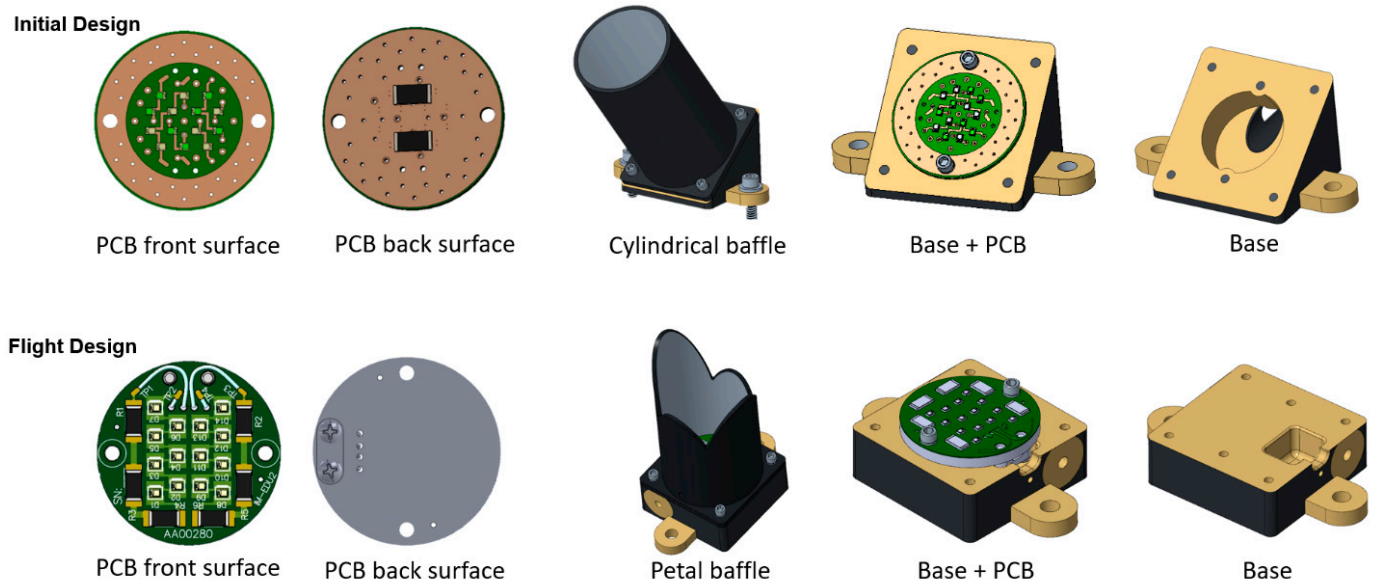

Figure 28. Illustration of the changes made to the initial illumination module design based on the lessons learned from the EDU fabrication and test activities.

The fabrication of the second set of EDU units followed the planned flight assembly process. The assembly commenced with the 14 LEDs and 6 resistors being installed on the PCB simultaneously. The components were placed on solder paste at their pad locations and reflowed at the same time through standard convection reflow. After these components were mounted, the electrical team soldered the wires and conducted electrical checks to ensure everything functioned correctly. This included verifying the electrical connection in each seven-LED circuit, ensuring resistor values were within specified tolerances and confirming electrical isolation. Toward the end of the PCB assembly process, Delrin thermoplastic (Wilmington, DE, USA) strain-relief clamps were installed on the underside of the PCBs for added durability and strain relief. Following this, the boards were ready for integration with the mechanical parts.

Assembly took place on an electrostatic discharge (ESD)-controlled workbench with all the necessary components laid out: the aluminum baffle and base; the populated PCB; the eGRAF HiTherm thermal interface material (previously cut using custom stencils to match the PCB-to-base contact area) and the fasteners. First, we placed the HiTherm cutouts on the base, ensuring accurate alignment. Then, the PCB was positioned so that its cables exited through a pre-designated groove in the base. We inspected the match between the shapes of the HiTherm thermal interface cutouts and the PCB to confirm a minimum of excess material. The PCB was then secured over the HiTherm layer and torqued down to the inserts on the base per the specification. Next, a fit check of the baffle over the base and board was conducted and the alignment was verified by inspecting the edges of the baffle and PCB. Finally, we fastened the baffle to the base by torquing down the fasteners to specification. We constructed a total of four flight-like illumination modules in this manner and checked for proper operation before proceeding to more in-depth optical testing. Figure 29 shows two of the completed EDU units constructed from the flight design.

Figure 29. Image of two of the EDU illumination modules constructed from the flight model design. Although the −Z module (**left**) and the +Z module (**right**) baffles appear to be mirror copies, they are not exact mirror matches due to the use of a common module base. The small hole visible near the PCB in each module is for EDU test instrumentation and will not be present in the flight models (Photo Credit: Katherine M. Mellos).

The goal for the detailed optical characterization of the final EDU units was to determine how well the flight baffle design meets the illumination system illuminance and uniformity requirements and matches the performance predicted by our design and analysis tools. We prepared for the tests by mounting the illumination module to a cage set-up secured to an optical bench and aiming the module back toward the bench along a vector perpendicular to the optical bench tabletop. On the optical table, a two-degree of freedom translation stage, aligned with the illumination module base held above, carried a calibrated International Light Technologies (Peabody, MA, USA) ILT2400 photometer head with a 3 mm diameter aperture. The photometer could translate up to 417 mm in one direction and 303 mm in the other to cover with margin the required elliptical illumination areas. The test set up was located in a clean tent in an ESD (electrostatic discharge) controlled space, and the environment was maintained to within ±3 °C of 20 °C using heaters and a humidifier.

The test set up was precision aligned using a helium-neon (HeNe) laser, flat mirrors and a pellicle mounted in between the illumination module and the center of the PCB. This step ensured close to 0° tip/tilt between the PCB and the photometer head when the photometer was directly below the illumination module. Figure 30 shows the optical test configuration.
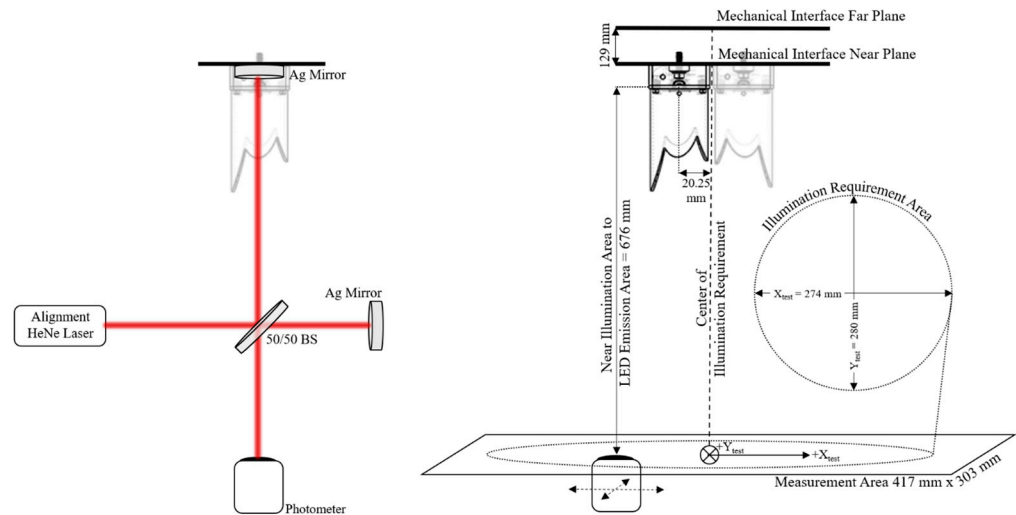
Figure 30. Illustration of the EDU illumination module optical test set-up. The diagram on the left shows the alignment approach used to minimize the tip/tilt between the illumination module LED emission plane surface normal and the optical measurement plane. The diagram on the right shows the optical test dimensions. Note the test distance is 1 mm different from the distance originally used to design the baffle due to late changes in the illumination module design and CCRS accommodations.

The optical testing proceeded by powering the illumination modules at 80 mA and letting them reach thermal equilibrium. Then, we acquired photometer measurements by translating the photometer step by step throughout the 417 mm × 303 mm test area. The measurements and translations were all automated through computer control of the stages and photometer. The translation step sizes were 3 mm along each axis, and at each position three measurements were taken before moving onto the next point. We used two types of scans during the test: a profile scan and a grid scan. The grid scans measured illuminance at equidistant points throughout the required illumination area while the profile scans measured illuminance along two orthogonal lines that intersect directly below the illumination module. We completed illuminance measurements at two photometer head ranges from the illumination module mechanical interface, 689.6 mm and 818.2 mm, to evaluate performance at the required distances.

Our analysis of the EDU optical measurements shows that all four illumination modules (two +Z and two −Z) constructed using the flight design and manufacturing processes meet the illuminance requirements at both the near and far evaluation planes (see Figure 31). The illuminance variation requirement is also met over most of the required area for all four EDU modules except for a portion of the required ellipse, ~5 mm wide and 12 mm long, near the edge of the requirement zone where the variation is 5% or more (see Figure 31). A subsequent investigation has found that this non-compliance was mistakenly designed into the baffles due to the SolidWorks "Lofted Cut" feature. This feature only ensures that points on the perimeter of the emission area have an unobscured view of a corresponding point on the perimeter of the illumination area. This causes some portions near the edge of the illumination area to be non-compliant where LEDs located at the corners of the emission area are partially obscured by the baffle.
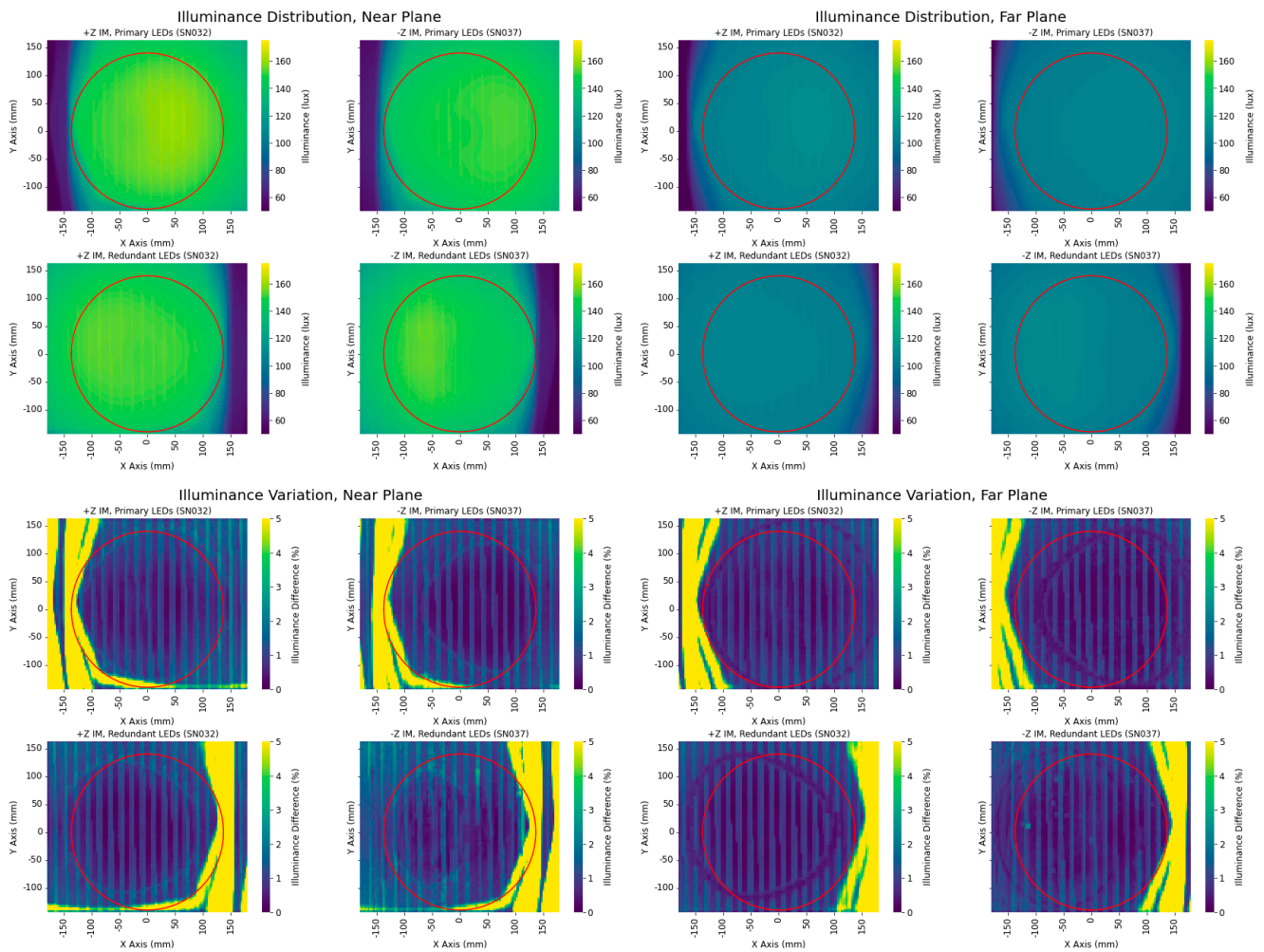
Figure 31. EDU illumination module optical test results at both the near (**left**) and far (**right**) evaluation planes for the two +Z illumination modules and two −Z illumination modules. In all eight cases, the maximum and minimum illuminance requirements are met over the required area (red circle). The illuminance variation requirement is also met over most of the required area (red circle) for all eight EDU modules except for areas ~5 mm × 12 mm in size near the edge of the requirement zone where the variation is 5% or more. A subsequent investigation has found that this non-compliance was mistakenly designed into the baffles due to a misunderstanding of the SolidWorks "Lofted Cut" feature. Note that the low-level periodic variation running left to right in the illuminance uniformity results are not present in the optical patterns but are caused by periodic noise in the photometer.

Although our plan is to slightly modify the illumination module baffle to correct the small design error for the flight-build, the illuminance variation violations are minor with respect to the overall system performance.

The vision system operations concept that the system was designed around calls for seven LEDs in both the +Z and −Z illumination modules to illuminate the OS at the same time when images are acquired. In addition, the current CCRS operations concept calls for powering all 14 LEDs simultaneously in each illumination module during image acquisition due to the operational efficiencies that the approach provides. Figure 32 shows how the illumination pattern changes when either of these two operations concepts are employed.
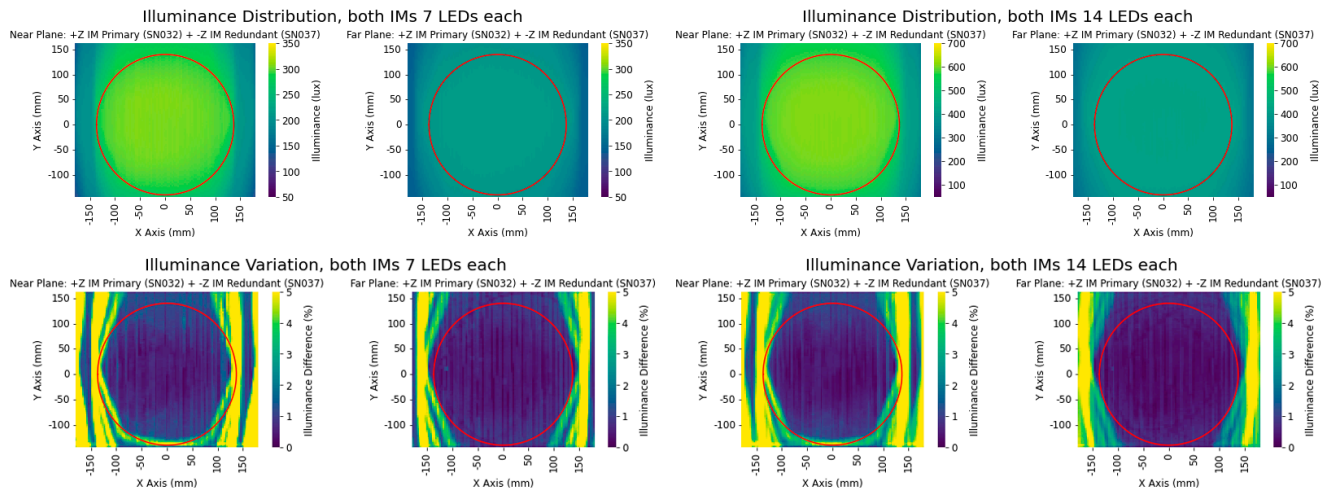
Figure 32. EDU illuminance results over the required area (red circle) when the primary 7 LEDs in each illumination module are powered on (**left**) and all 14 LEDs in each illumination module are powered on (**right**). With 7 LEDs in each illumination module powered on, the illuminance doubles when compared to only one module being powered on (see Figure 31). With 14 LEDs in each illumination module powered on, the illuminance doubles when compared to 7 LEDs being powered in each illumination module. For the case with all LEDs powered on, the small areas at the near plane where the illuminance uniformity is >5% appear on both sides of the required area while the individual areas of non-uniformity shrink. Although the nominal vision system operations concept assumes only 7 LEDs in each illumination module are powered on, for operational efficiency the CCRS operations concept currently assumes all LEDs (28) will be powered on during imaging.

5. Vision System Performance

To assess the performance of the cameras and illumination modules functioning together as a unified CCRS sub-system, we completed a comprehensive optical test and analysis program. The activities included the following: optical characterization of CCRS surface treatments, laboratory testing, non-sequential ray tracing and system modeling using higher-level languages such as Python.

In our experience this level of effort is unprecedented when compared to the development of optical systems for other planetary missions. We believe in the necessity of this activity given the criticality of the CCRS operation in the greater MSR campaign as well as the complicated imaging scene created by the captured OS and the CCRS interior. Relying on first-order calculations or depending upon scene simplifications is useful and expedient to develop component-level specifications but is inadequate for verifying vision system performance in the unique CCRS environment. Discovering inadequate vision system performance during the CCRS-level integration and test phase would jeopardize our ability to launch on schedule—an unacceptable risk. Through our extensive test and analysis program, we have determined that the flight system design will easily meet the CCRS on-orbit operational goals with significant margin. The sections that follow provide the basis for this conclusion.

5.1. Reflectivity and Scattering Measurements

Unlike our typical experience with planetary mission imaging systems, everything we plan to observe with the CCRS vision system will be manufactured. The only naturally occurring material we may image is contamination on the OS exterior. This provides both a challenge and an opportunity. The challenging aspect is that fabricated components are likely to have much more disparate reflectance properties than objects that appear in nature, potentially requiring a much more flexible imaging system than otherwise would be required. The advantage is that we can measure proposed MSR and CCRS surface properties to inform the selection of surface finishes as well as develop highly accurate

predictions of vision system performance. To address both of these aspects, we initiated a comprehensive optical characterization campaign of MSR and CCRS surface finishes relevant to the vision system.

Characterization of MSR and CCRS surface finish samples was performed at the Goddard Space Flight Center (GSFC) with the Diffuser Calibration Laboratory's (DCL) optical scatterometer [18]. The DCL is a secondary calibration facility with radiometric calibration measurement capabilities traceable to those made in the primary facility located at the National Institute of Standards and Technology (NIST). The scatterometer is cleanroom compatible. It can be used for BRDF and/or BTDF (bidirectional transmission distribution function) measurements in both in-plane and out-of-plane modes. The setup is modifiable to address the requirements of each project. The main configuration of the optical table includes the following components: an Energetiq EQ99 light source, a monochromator, tunable coherent sources, a supercontinuum white laser and an optical parametric oscillator system. Additional sources, polarization analyzers and filters can be connected to the setup depending on project requirements. Three detectors are available depending on the spectral range of interest: ultraviolet-enhanced silicon from 250 nm to 900 nm, indium gallium arsenide from 900 nm to 1700 nm and extended indium gallium arsenide from 1700 nm to 2500 nm.

We typically characterized the MSR and CCRS surface finish test coupons at 440 nm, 550 nm and 700 nm. BRDF measurements were made at $0°$, $15°$, $30°$, $45°$ and $60°$ incident angles over scatter angles of $-80°$ to $80°$ in increments of $5°$. Total hemispherical reflectance was also measured using a Prkin-Elmer 1050 spectrometer equipped with a 150 mm diameter integrating sphere. A summary of the materials tested is provided in Table 6. A summary of measurements is provided in Figures 33 and 34.

Table 6. Summary of the MSR and CCRS material whose surface scattering characteristics were measured.

| Coating	Coupon Description	Relevant MSR CCRS Component
Ceranovis CN-V14, No Sealant	60 mm × 60 mm, 50 μm coating thickness, 1.5 mm Ti-6Al-4V substrate, pre-friction testing	Potential OS endcap surface finish
Ceranovis CN-V14 Li-doped Sealant	60 mm × 60 mm, 50 μm coating thickness, 1.5 mm Ti-6Al-4V substrate, pre-friction testing	Nominal OS endcap surface finish
Ceranovis CN-V14 Sealant	60 mm × 60 mm, 50 μm coating thickness, 1.5 mm Ti-6Al-4V substrate, pre-friction testing	Potential OS endcap surface finish
Ceranovis CN-V14, No Sealant	60 mm × 60 mm, 50 μm coating thickness, 1.5 mm Ti-6Al-4V substrate, post-friction testing	Potential OS endcap surface finish after CCRS capture
Ceranovis CN-V14 Li-doped Sealant	60 mm × 60 mm, 50 μm coating thickness, 1.5 mm Ti-6Al-4V substrate, post-friction testing	Nominal OS endcap surface finish after CCRS capture
Ceranovis CN-V14 Sealant	60 mm × 60 mm, 50 μm coating thickness, 1.5 mm Ti-6Al-4V substrate, post-friction testing	Potential OS endcap surface finish after CCRS capture
20 psi Bead-blasted Aluminum with Clear Anodize	60 mm × 60 mm, aluminum 6061-T6	Potential illumination module baffle interior coating
30 psi Bead-blasted Aluminum with Clear Anodize	60 mm × 60 mm, aluminum 6061-T6	Nominal illumination module baffle interior coating
40 psi Bead-blasted Aluminum with Clear Anodize	60 mm × 60 mm, aluminum 6061-T6	Potential illumination module baffle interior coating
Final EDU Baffle Interior	60 mm × 60 mm aluminum	30 psi bead-blasted aluminum with clear anodize
Final EDU Baffle Exterior	60 mm × 60 mm aluminum	Black anodize
3D Printed White Resin	60 mm × 60 mm, 3D-printed resin RS-F2-GPWH-04	CCRS vision system lab capture cone and orientation mechanism
Aluminum 7075 with Teflon coating	60 mm × 60 mm aluminum coupon	CCRS capture cone interior and exterior
Aluminum 6061 with Teflon coating	60 mm × 60 mm aluminum coupon	CCRS capture cone flange interior and exterior
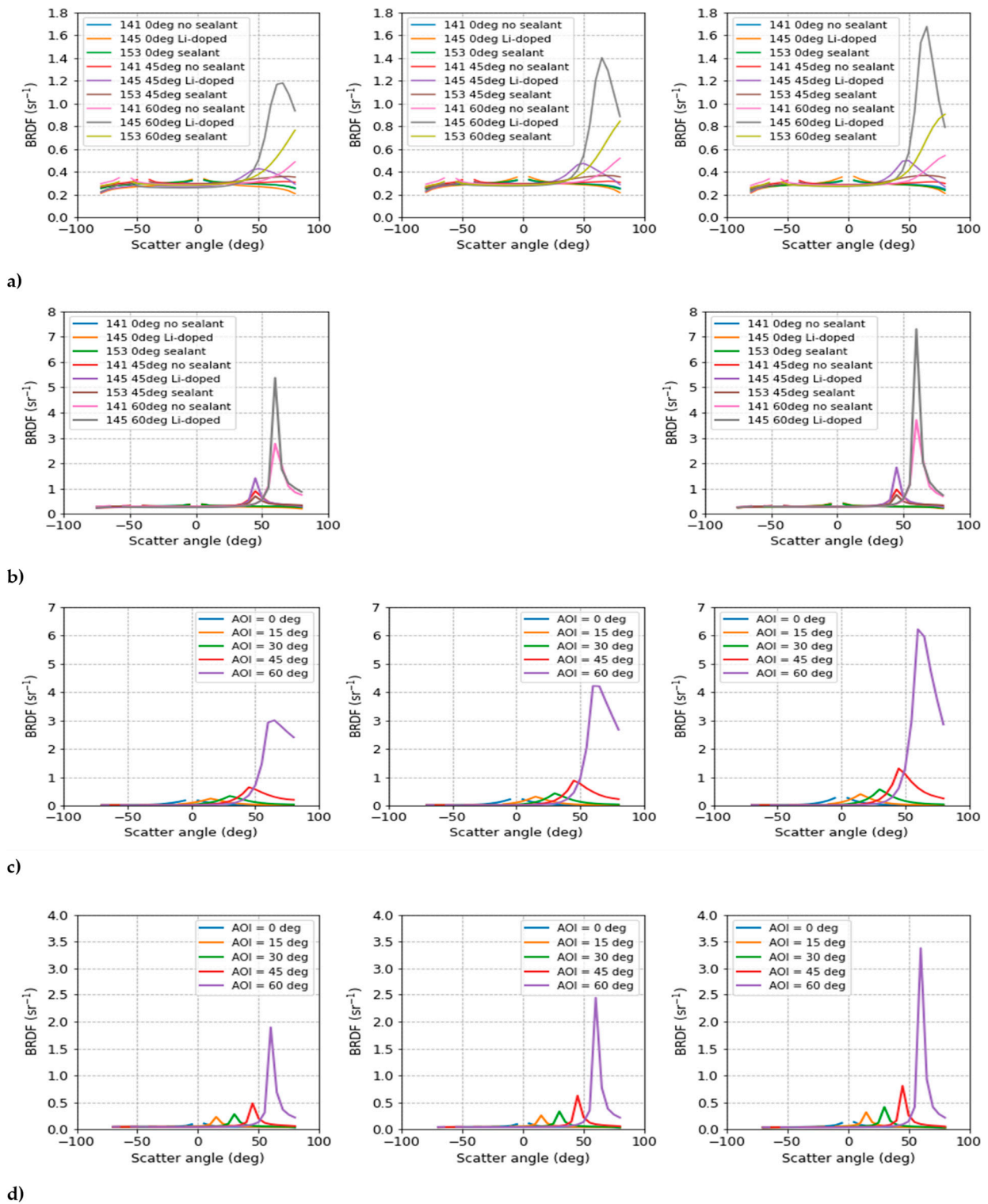
Figure 33. BRDF measurements of CCRS surface treatments relevant to the vision system at 440 nm (**left column**), 550 nm (**middle column**) and 700 nm (**right column**) for (**a**) Ceranovis pre-friction test, (**b**) Ceranovis post-friction test, (**c**) aluminum 6061 with Teflon coating and (**d**) aluminum 7075 with Teflon coating.
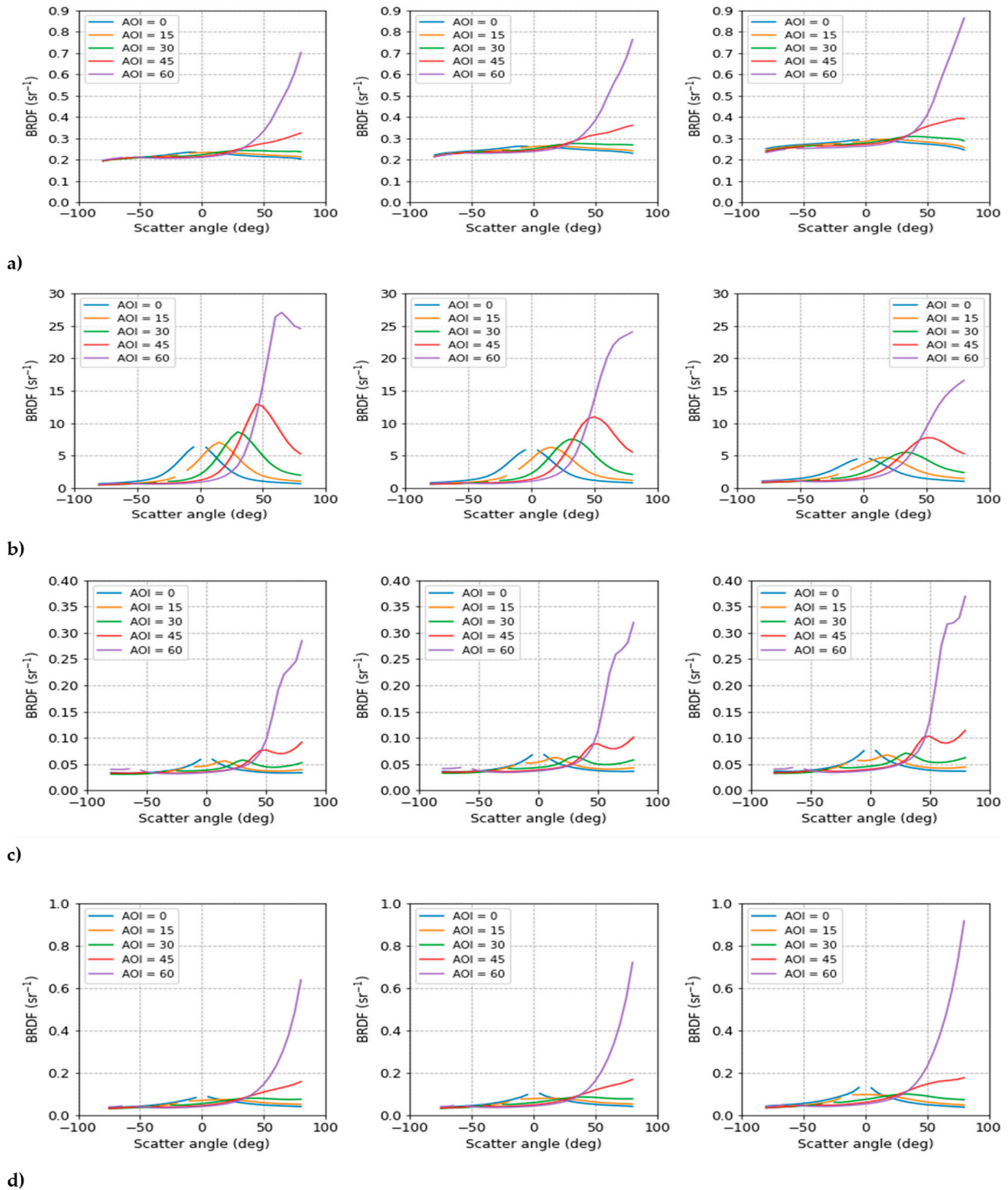
Figure 34. Vison system surface treatment BRDF measurements of (**a**) 3D-printed material at 440 nm (**left**), 550 nm (**center**) and 700 nm (**right**) for the OS endcap surrogates, (**b**) 550 nm measurements of bead-blasted aluminum with clear anodize at 20 psi (**left**), 30 psi (**center**) and 40 psi (**right**), (**c**) 30 psi bead-blasted aluminum with clear anodize at 440 nm (**left**), 550 nm (**center**) and 700 nm (**right**) and (**d**) black anodized aluminum at 440 nm (**left**), 550 nm (**center**) and 700 nm (**right**).

5.2. Laboratory Results

To assess imaging performance, we constructed a vision system laboratory testbed to support component and system level optical testing. It is capable of rapidly producing high-fidelity images in geometries and conditions comparable to the CCRS. We use it to predict

system performance under a wide range of scenarios and to cross-check computational models. The system level testbed is composed of off-the-shelf components, engineering development units (EDU) and custom 3D-printed parts. See Figure 35.
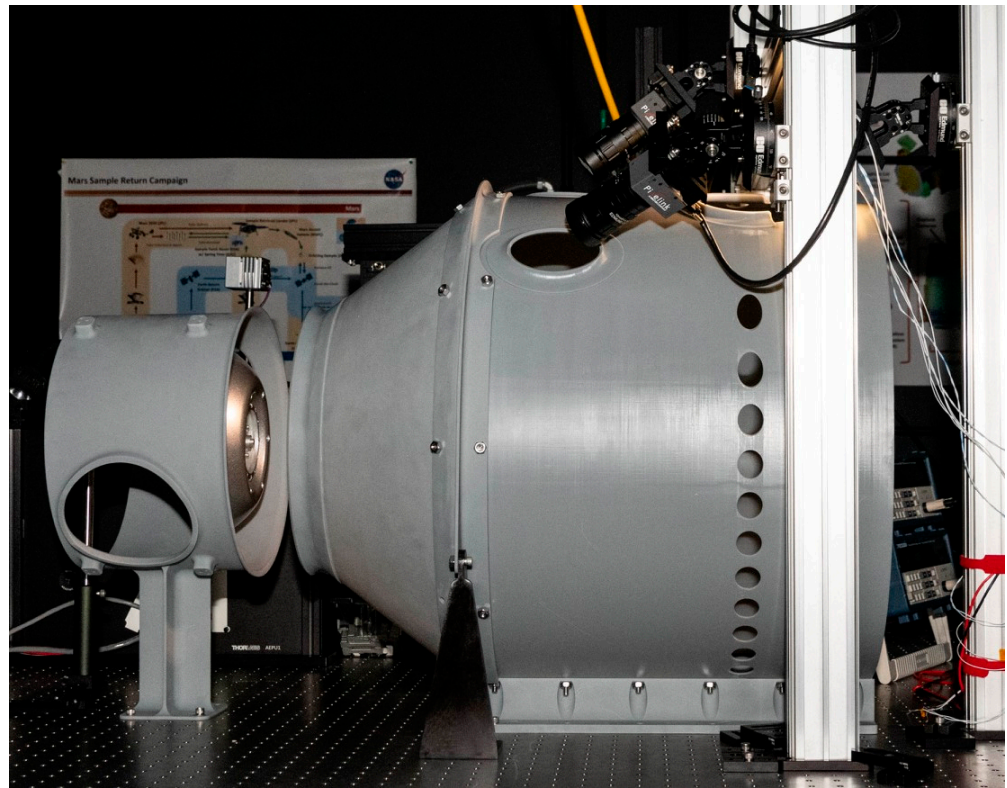

Figure 35. Vision system laboratory testbed utilizing commercially available off-the-shelf (COTS) cameras, engineering development unit (EDU) illumination modules and 3D-printed representations of the CCRS capture cone, orientation mechanism and both OS container endcaps (Photo Credit: Katherine M. Mellos).

The testbed imaging system consists of two PixelLink Color 20 Mpx 1" 12-bit sensor cameras with Edmund Optics 12 mm TECHSPEC HP Series fixed focal length lenses set to F/3.5. This system has higher resolution, better signal-to-noise (SNR > 80), larger FOV and a smaller instantaneous field of view than the assumed flight system, allowing us to degrade and resample images in postprocessing to match specific flight system candidates. Postprocessing is further discussed in Section 5.4. The modulation transfer function (MTF) of the lens was measured using the commercially available Optikos LensCheck Finite Conjugate System [19] and exceeds or closely matches the performance of the flight lens system (see Figure 36). We confirmed that the camera's linear response with respect to luminance and exposure duration extends from at least 70 ms to 2000 ms using calibrated reflectance standards and a stable illumination source.

The testbed illumination system consists of two EDU LED boards with 3D-printed baffles designed to create the current flight design illumination footprint. The diffuse-white 3D-printed specialty baffles mimic the diffuse bead-blasted interior of the flight illumination system assembly baffles and shape the outgoing illumination pattern. The testbed illumination modules were operated at 25 °C and driven at 80 mA for each set of seven LEDs connected in series, then scaled in postprocessing to match worst-case operating temperature and voltage conditions.
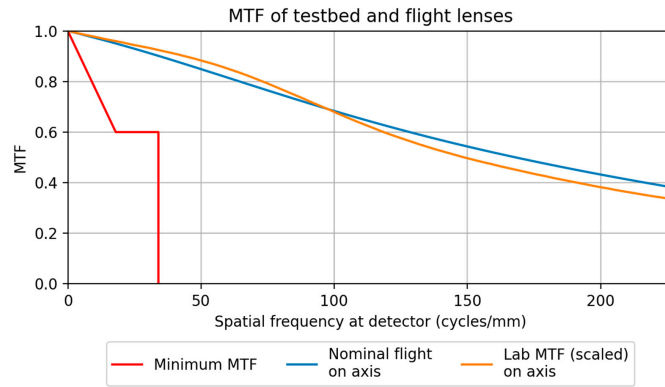
Figure 36. MTF of the lab testbed lens (orange), the flight camera lens (blue) and the minimum allowable vision system camera optics (red).

The testbed uses 3D-printed OS lid and base endcaps. These are printed in-house at GSFC to allow for rapid turnaround with OS design changes. The bare white resin material is used as a proxy of the baseline Li-doped, Ceranovis-145 OS coating. A shiny metallic spray paint coating is used as a proxy of the worst-case specular OS BRDF specification (See Equation (1)). Since the testbed did not have access to endcaps with the flight materials and coatings, BRDF measurements were taken of bare and painted 3D-printed coupons to determine how closely they matched the actual surfaces (see Figure 37).
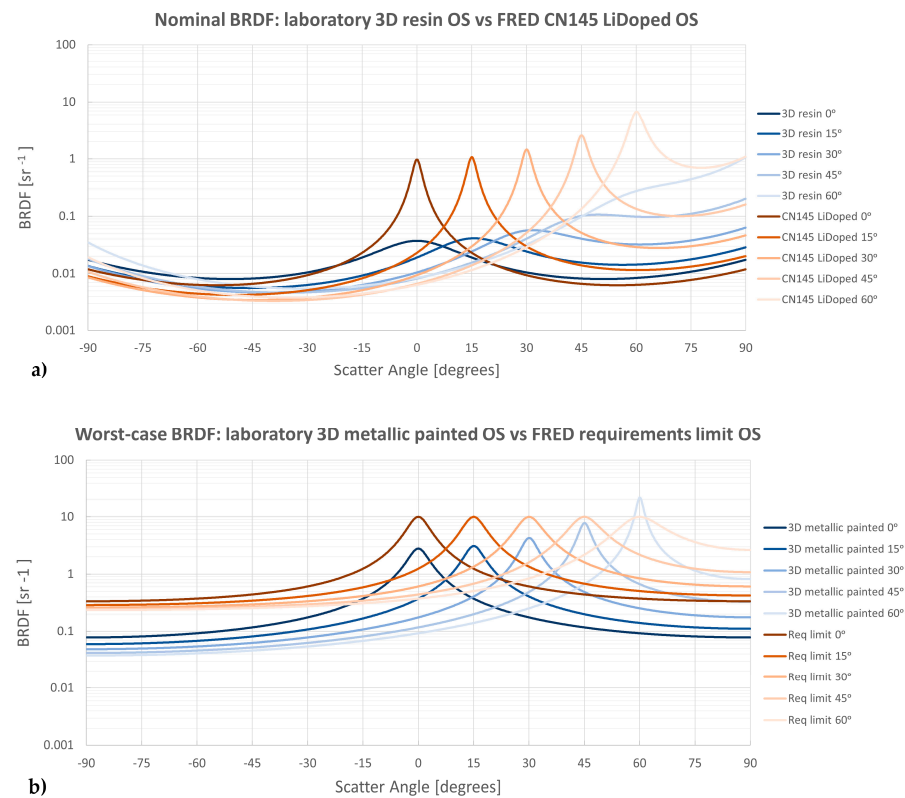

Figure 37. BRDF comparison for a variety of incidence angles (AOI) of the two laboratory testbed OS surface finishes (3D resin and 3D metallic paint) to the two OS surface finishes (CN145 Li-Doped and Req. limit) used in the non-sequential ray trace model. The 3D resin (**a**) represents the current OS surface finish in the testbed and matches well to the Ceranovis BRDF modeled in the non-sequential model except for the specular peak caused via friction testing. The metallic paint (**b**) represents the worst-case OS surface finish currently allowed by OS requirements. It agrees well with the OS BRDF requirement limit, particularly near the specular peaks.

3D-printed parts manufactured by Protolabs Inc. are used as proxies for the surrounding spacecraft infrastructure which substantially interacts with the vision system. Part structure is taken directly from flight assembly part models and altered only for attachment to the lab bench. BRDF measurements were not taken of these materials, as they are intended only for checks of obscuration and high-level scatter effects, though visual comparison of the grey 3D-printed pieces and the Teflon anodized Al 7075 assumed flight surfaces show roughly similar optical properties.

Laboratory cameras and illumination modules are manually aligned and located to within 0.5 mm and 0.5° at each build stage (i.e., camera location and pointing relative to the camera mount). The components mount via multiple layers of stages, with the propagated errors resulting in approximately 5 mm and 3° locational uncertainty relative to the lab origin. An image of the lab setup from 1 m behind the OS along the y-axis, taken with a known imaging system, was compared to a simulated image of the perfectly aligned setup. The comparison showed the alignment error to be less than ~5 mm. Final laboratory system level images agree in perspective with simulated non-sequential ray trace model images, further indicating that laboratory locational errors do not significantly impact our laboratory results and conclusions.

Illuminance is measured using an International Light Technology (ILT) 2400, SED033 sensor with a photopic filter at a spectral range of 400–700 nm. ILT calibrated the meter to $\pm4.8\%$ at 3215 K using a standard quartz–tungsten–halogen source. Readout error at different color temperatures within 500 K of 3215 K falls within 1%. We used two independent cosine and photopic corrected light meters (Cooke cal-LIGHT 400) to perform an initial cross-check of the ILT calibration; results agree on-axis to within 3% and off-axis to within 4%. In all the photometer calibration checks, we used the same LXZ1-4070 LED at 20 °C and powered it at 0.3 mA to illuminate the photometer 600 mm away. Additionally, the photometer calibration was verified against the GSFC photonics group's Ocean Optics Spectrometer illuminated with a 4000 K White LED Board; the ILT photometer is 12% lower than the spectrometer's calibrated power value, likely due to the ILT photometer being calibrated for a different spectrum shape than the 4000 K LEDs. We investigated the response of the photometer to oblique illumination and found that its response deviates by $\geq5\%$ from that of an ideal radiometer when the angle of incidence is $>20°$. Removal of the diffuser head provides a photometer response that follows the theoretical cosine falloff out to an incidence angle of 45° to within 5% but invalidates the absolute photometric calibration.

For most laboratory work that involves cameras or the entire vision system, we require our testbed images to be radiometrically calibrated in terms of luminance. To accomplish this, we image diffuse reflectance standards of varying reflectance and calibrate against the ILT photometer placed at the same location as the standard. The calibration setup is illuminated at normal incidence to the plane of the standard/photometer head and imaged at 13° off axis (as close as possible given the setup) to minimize cosine fall-off effects. We calculate a calibration factor for each red, green and blue image layer and apply it in postprocessing. Dark current images are taken for each unique set of images and applied in postprocessing.

Our laboratory images of the current flight baseline and worst case (i.e., all system performance characteristics at the edge of compliance) show compliance with requirements, see Figures 38 and 39. The images provide clear distinguishability between the OS lid and base, and luminance requirements are met over the visible portion of the OS with key distinguishing features. Testbed images were also used to cross-check images generated completely by computer simulations (see Section 5.3). These show agreement overall views and in endcap distinguishability and agree in calibrated luminance to within ~10% (see Section 5.3 for further discussion).
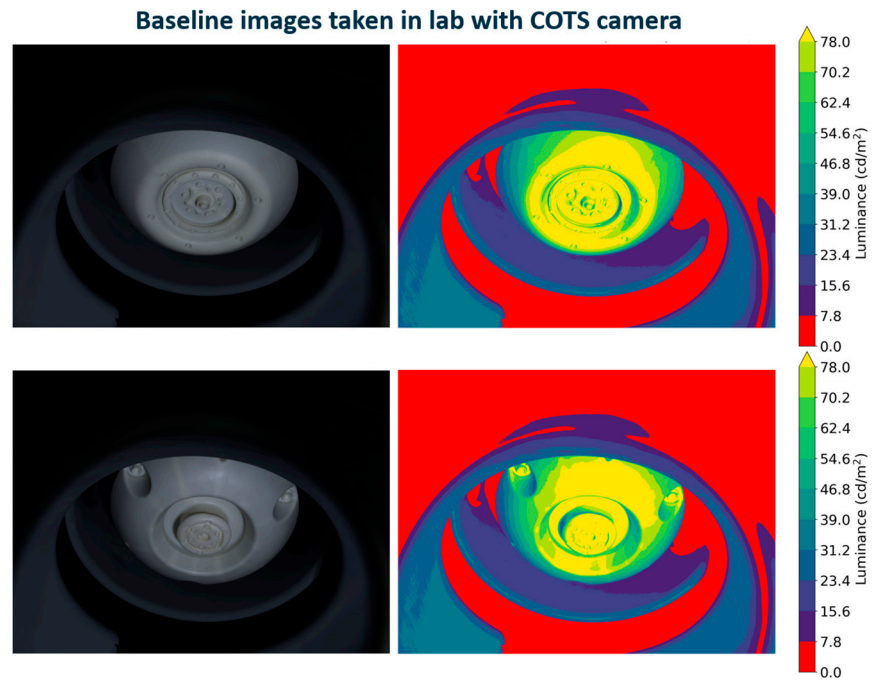
Figure 38. System-level images from the $-Z$ camera position in the laboratory testbed, showing the vision system baseline performance for the lab surrogate of the current OS surface finish. The right column shows the same images reporting calibrated luminance values. Red indicates the areas in the image below the 7.8 candela/m2 OS luminance requirement. No areas on the OS are below the luminance requirement.
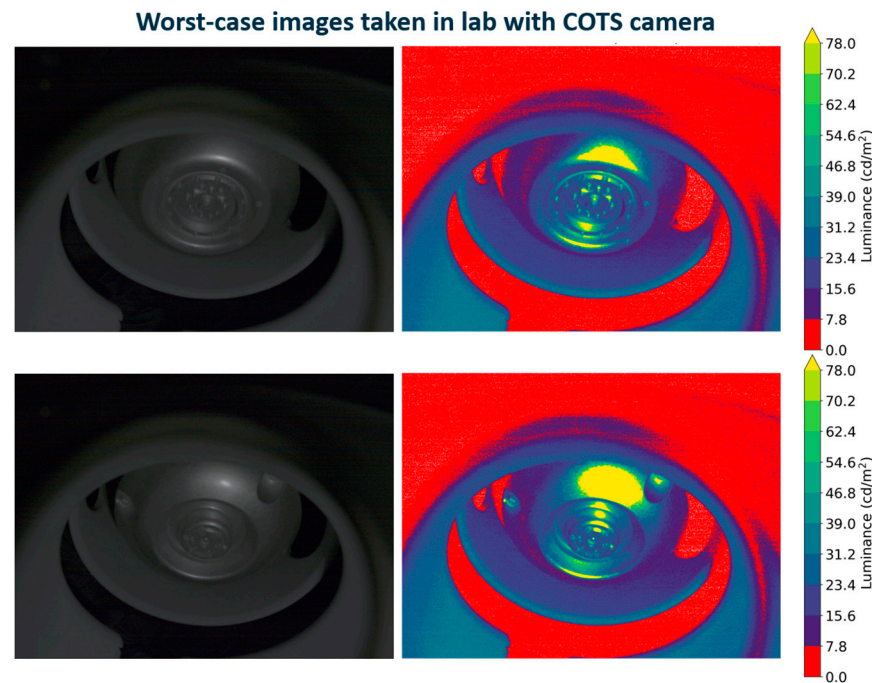

Figure 39. System-level images from the $-Z$ camera position laboratory testbed, showing the baseline vision system performance for an OS with the most specularly reflective surface finish allowed by requirements. The right column shows the same images reporting calibrated luminance values. Red indicates the areas in the image below the 7.8 candela/m2 OS luminance requirement. Except for a few small points, the majority of the OS surface meets the luminance requirement.

5.3. Non-Sequential Ray Trace Modeling

In addition to the laboratory testbed that we constructed to assess vision system performance (Section 5.2), we built in parallel a non-sequential ray trace model of the CCRS vision system using the commercially available FRED Optimum software version 22.40.4 with the FREDmpc extension (Photon Engineering, Tucson, AZ, USA). We used this tool in conjunction with the laboratory testing to accomplish the following:

- More accurately represent the CCRS surface finishes;
- Incorporate the optical performance of the actual lens design;
- Position and orientate components more accurately than the laboratory;
- Include CCRS components that cannot be economically or quickly created in the laboratory;
- Evaluate the performance of off-nominal conditions;
- Assess scattered light paths within the CCRS capture enclosure.

We created the model geometry primarily from STEP (Standard for the Exchange of Product Model Data) file exports of the CCRS and OS CAD designs developed in Creo (PTC, Boston, MA, USA). CCRS components were simplified within Creo prior to export to contain only the optical information relevant to the non-sequential model.

Both camera models were built from information provided by MSSS. The refractive optical prescription was imported from a Zemax OpticStudio (Ansys, Canonsburg, PA, USA) model while the mechanical housing was built from information provided in a STEP file. The model validity was confirmed by verifying the glass model for each lens, crosschecking dimensions with the original Zemax file and then checking the skew ray intercepts at the detector and lens surfaces to confirm they match the Zemax results.

The illumination module representations were built from a combination of native FRED objects and STEP file exports from the illumination system CAD design. LED emission properties were modeled using a curve fit of the vendor's beam apodization data, and the total LED reported integrated light output in terms of lumens.

We assigned model optical properties based on measurements of hardware coupons or measurements of similar materials that have previously flown on spacecraft. The model surface properties are summarized in Table 7. Optical properties that varied with incidence and exitance angle were modeled by fitting analytical forms of a combined Harvey–Shack and Lambertian model [20] to the laboratory BRDF measurements. An example of the scatter model we used for the OS coating is shown in Figure 40. Views of the completed model are shown in Figures 41 and 42.

Table 7. Summary of the surface properties assigned to the CCRS vision system non-sequential ray trace model (FRED) key components.

FRED Model Component	Optical Properties Assigned	Notes
Capture Cone Interior	AL 7075 with Teflon coating	Measured BRDF at NASA/GSFC
Capture Cone Exterior	AL 7075 with Teflon coating	Measured BRDF at NASA/GSFC
Capture Cone Collar Interior	AL 6061 with Teflon coating	Measured BRDF at NASA/GSFC
Capture Cone Collar Exterior	AL 6061 with Teflon coating	Measured BRDF at NASA/GSFC
Lens Volumes	0% absorbing; 100% transmittance; 0% reflectance; 0% scatter	Assumes ideal lens system
Lens Surfaces	100% anti-reflection coating	Assumes ideal lens system
Camera Housing Interior	100% absorbing	Not necessary for analyzing target scene luminance
Camera Housing Exterior	100% absorbing	Not necessary for analyzing target scene luminance
Camera Detector	100% absorbing	Not necessary for analyzing target scene luminance

Table 7. *Cont.*

| FRED Model Component	Optical Properties Assigned	Notes
Illumination Module Baffle Interior	100% absorbing	LED directivity varied less than 2% due to baffle multi-scatter and absorption
Illumination Module Baffle Exterior	100% absorbing	N/A
Illumination Module Base Interior	100% absorbing	Multi-scatter and back-scatter effects negligible
Illumination Module Base Exterior	100% absorbing	N/A
Illumination Module PCB	100% absorbing	Multi-scatter and back-scatter effects negligible
Orientation Mechanism Inner Liner Exterior	AL 6061 with Teflon Coating	Measured BRDF at NASA/GSFC
Orientation Mechanism Flat- and V-Paddles	AL 6061 with Teflon Coating	Measured BRDF at NASA/GSFC
Orientation Mechanism Primary Structure Exterior	AL6061-T651 Machined; Clear Coat	OSIRIS-REx surface property library
Nominal OS Base	Friction-Tested Ceranovis with Li-Doped Sealant	Measured BRDF at NASA/GSFC
Nominal OS Lid	Friction-Tested Ceranovis with Li-Doped Sealant	Measured BRDF at NASA/GSFC
Highly Specular OS Base	Requirement-Limited BRDF	Harvey–Shack BRDF model fitted to requirement limits
Highly Specular OS Lid	Requirement-Limited BRDF	Harvey–Shack BRDF model fitted to requirement limits
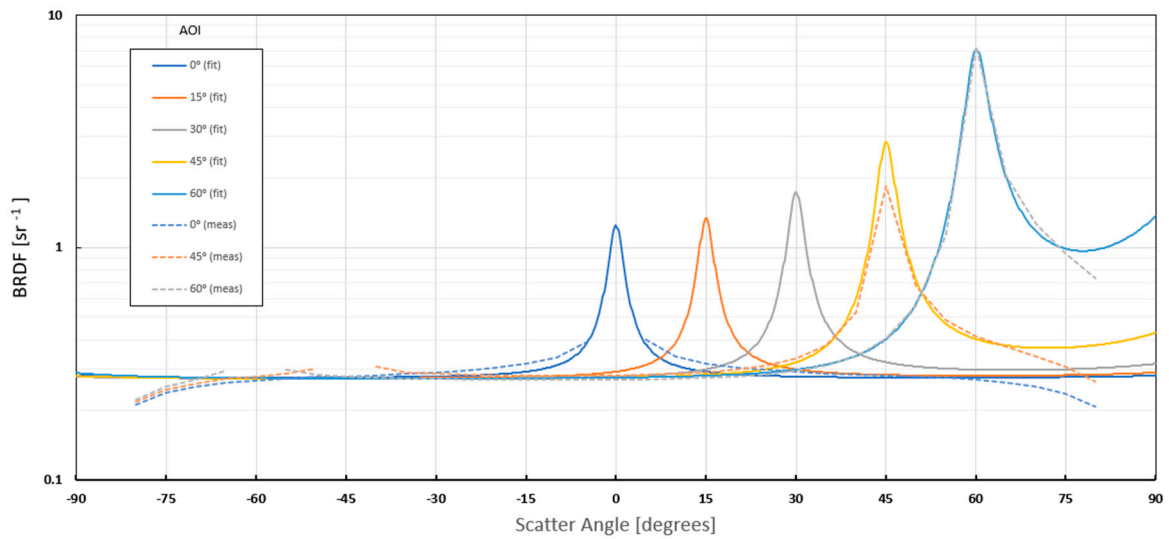
Figure 40. FRED BRDF model fit at various angles of incidence (AOI) to the measured data for the Ceranovis-145 with Li-Doped sealant after going through surface friction testing.

We validated the radiometric accuracy of the non-sequential model by ray tracing a special case of the CCRS set up that we could also readily replicate in the laboratory. The test set up included just the cameras, illumination modules and a nominal OS base and lid. The LED light output in the model was set to match the current draw on the laboratory power supply. This initial crosscheck identified a small error in the laboratory calibration as well as a non-trivial calculation error in FRED. Through additional work, we determined the FRED radiometric error only occurred when running ray trace calculations on the computer's graphics processing unit (GPU). Subsequently we started running our FRED calculations on the computer's central processing units (CPU) while the software vendor worked with the GPU vendor (NVIDIA) to correct the 522.30 NVIDIA driver issue. We also recalibrated all of our laboratory data. Even though the GPU-based calculations run 100 to 145 times faster than the CPU calculations, we have not been able to validate that the GPU calculations produce radiometrically accurate predictions and are avoiding that

functionality for the time being. All of the results we present here come from calculations run on the CPU.
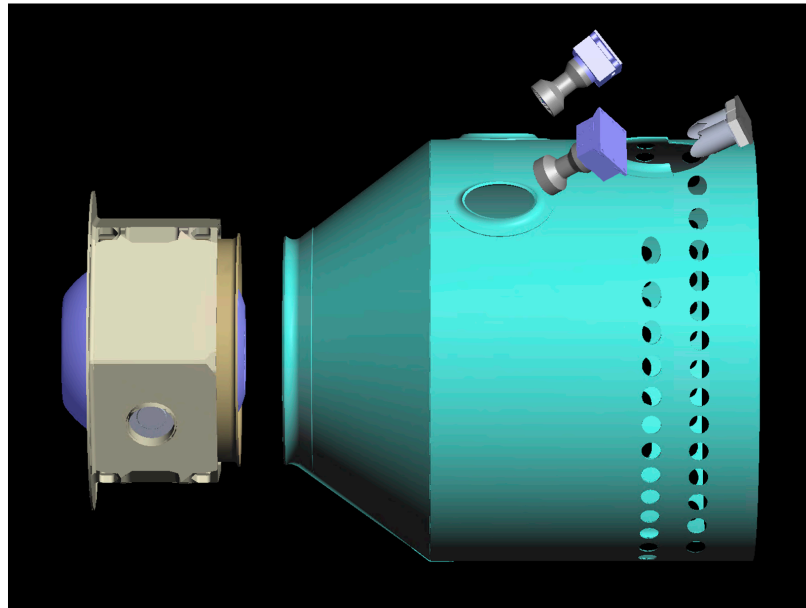

Figure 41. View of the CCRS vision system non-sequential ray trace model components. It includes both cameras, both illumination modules, the capture cone with porthole strengthening members, the major portions of the orientation mechanism and the OS.
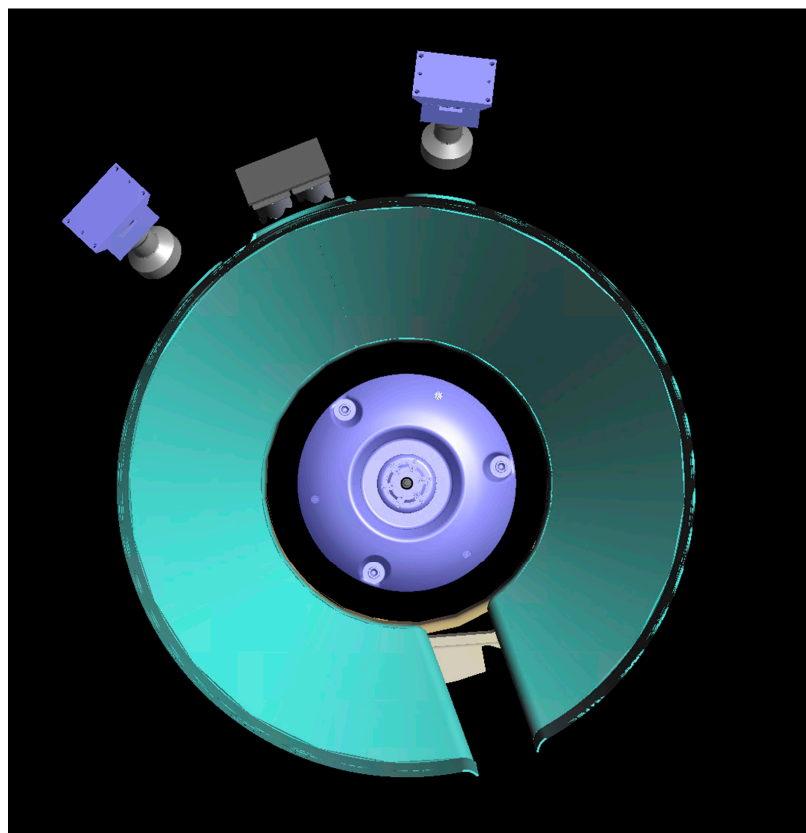

Figure 42. View of the CCRS vision system non-sequential ray trace model components looking from the capture side along the CCRS Y-axis. Viewable items include both cameras, both illumination modules, the capture cone interior, one OS endcap and small portions of the orientation mechanism.

After correcting the laboratory and software errors, we find good radiometric agreement between the laboratory test results and the non-sequential model predictions. Within the areas of slowly varying luminance across the OS base and lid, the radiometric predictions typically agree to ~10%—about the level of agreement we would expect based on our photometer's calibration uncertainty, our ability to measure and model the OS surface BRDF and the positional errors inherent in the laboratory set up (see Figure 43).
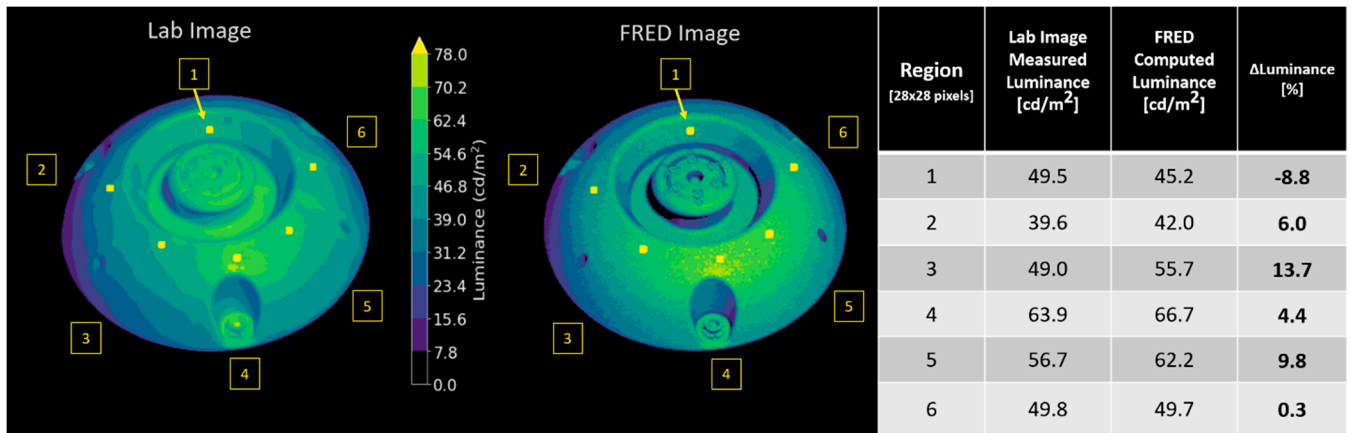

Region [28x28 pixels]	Lab Image Measured Luminance [cd/m²]	FRED Computed Luminance [cd/m²]	ΔLuminance [%]
1	49.5	45.2	-8.8
2	39.6	42.0	6.0
3	49.0	55.7	13.7
4	63.9	66.7	4.4
5	56.7	62.2	9.8
6	49.8	49.7	0.3

Figure 43. Comparison of the OS base luminance results from the laboratory measurements and the FRED non-sequential ray trace model prediction. Agreement between the two results is typically ~10%, consistent with our photometer calibration uncertainty and our ability to measure and model the OS BRDF. Luminance values shown in the table above are region averages calculated within square windows equivalent to a 28×28 pixel area on the flight vision system camera detector.

To create nominal vision system performance predictions, we set up the model geometry to match the nominal post-capture OS geometry of CCRS, including both possible OS capture orientations. Nominal surface properties (post-friction tested Ceranovis CN-14 with Li-doped sealant) are assigned to the OS (see Table 7). We allow one level of ray splitting from each ray launched and up to eleven scatter rays per ray (i.e., up to eleven "children" rays can come from one "parent" ray). Importance sampling is implemented to force scattered rays to propagate toward one of the cameras while maintaining radiometric accuracy. A total of 15.4 million rays with the same wavelength (700 nm) are launched in a single Monte Carlo run from either the primary or redundant set of LEDs and allowed to propagate and scatter until they reach a camera detector plane. This ray trace is repeated 250 times to improve the prediction statistics while keeping the ray trace dataset size below the computer memory cache limit. To improve the prediction statistics further, we sum the detected energy over 8.8 μm × 8.8 μm pixels in the analysis plane (equivalent to 4 × 4 pixel spacing in the actual detector). In this way, simulation signal-to-noise ratios (SNR) on the order of 20 or better can be achieved with only slight degradation in the prediction.

To generate the worst-case vision system performance predictions, to feed into the full vision system performance predictions of Section 5.4, we use the same settings and procedure as described above for the nominal conditions with two modifications. First, we switch the OS surface properties to match the worst-case specular BRDF described with Equation (1). Second, we position the OS as far away from the vision system as allowed by the CCRS capture tolerances and tilt the OS to the maximum tolerance in the most unfavorable orientation for viewing endcap features. Model results for both the worst-case and nominal conditions are presented in the following section (Section 5.4).

5.4. Full System Performance Predictions

Although both the laboratory testbed hardware and the non-sequential ray trace models are powerful tools for predicting the vision system performance, neither of them are able to include all the relevant effects that will determine the on-orbit vision system

performance. Fully predicting the interplay between the light emitted from the illumination module LEDs, the reflection of that light off the OS and its passage through the camera lens to the detector plane where it generates signal electrons within the CCRS flight environment requires additional work. Here, we describe the modeling techniques we use to turn the results from both the laboratory and the non-sequential ray trace tools into more accurate imaging performance predictions.

The laboratory testbed generates images with higher resolution and optical distortion that differs from the flight camera design. To correct this, we use the Zemax optical model provided with the Edmund Optics lens and the flight model optical prescription provided by MSSS. We use these optical models to calculate the radial distance from the optical axis at the image plane corresponding to field angles into each camera. These curves are then used to map pixel coordinates of the COTS lens to the image space of the flight lens. We average the values from the COTS sensor pixels with mapped coordinates falling within a flight system pixel to produce image data matching the FOV and IFOV of the flight system. Interpolation is not required since the IFOV of the COTS camera is less than that of the flight camera. Using this approach, we create the nominal performance predictions shown in Figure 44 using the laboratory results.
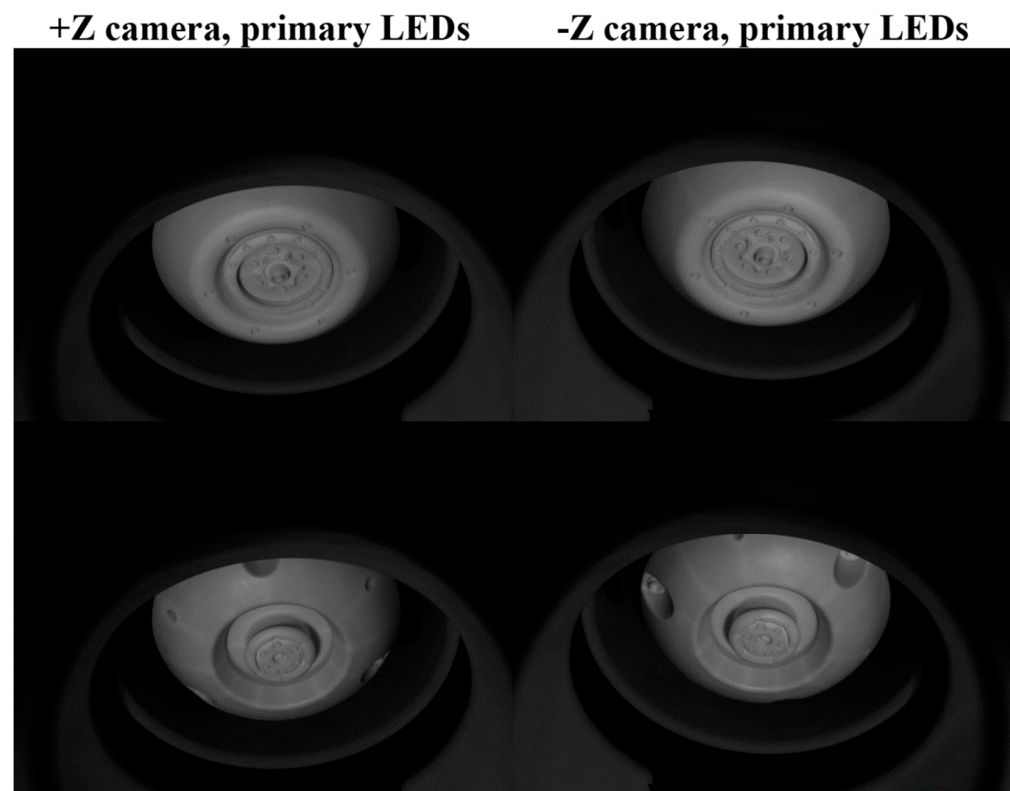

Figure 44. Four nominal vision system imaging performance predictions for the OS lid (**top row**) and OS base (**bottom row**) based on the laboratory testbed results for the +Z camera (**left column**) and −Z camera (**right column**) with the primary LED circuits in both illumination modules providing illumination.

Figure 44 shows that we can easily discriminate between the OS lid and base from vision system images. Based on the in-flight sensitivity of previous ECAM cameras [9], these simulations are equivalent to a 0.2 s exposure with a 1X gain setting—well within our 1 s requirement. The results from the non-sequential ray trace model lead us to the same conclusion (see Figure 45). Unlike the laboratory results, the FRED non-sequential ray trace model results do not require additional processing to faithfully represent nominal vision system performance. In fact, the FRED model's image quality is already slightly degraded due to the use of detector pixels four times larger than the actual detector. In

addition, the simulated images have approximately three times more random noise than a well-exposed real image will have due to the Monte Carlo ray trace statistics. Even under these less-than-optimal conditions our non-sequential ray trace modeling predicts excellent vision system performance.
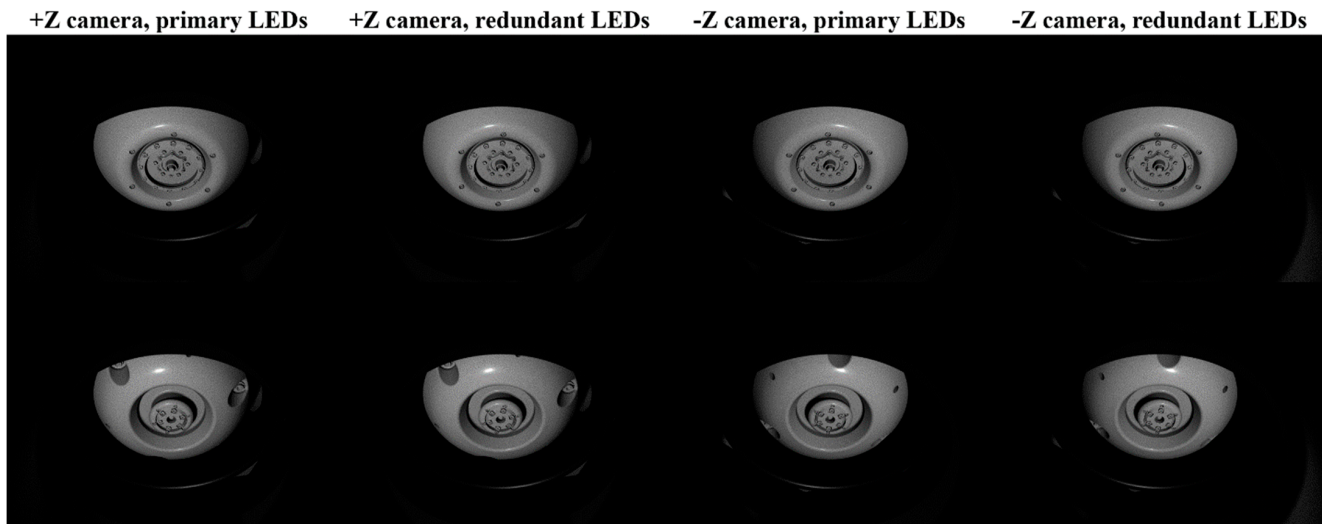
+Z camera, primary LEDs   **+Z camera, redundant LEDs**   **-Z camera, primary LEDs**   **-Z camera, redundant LEDs**

Figure 45. Eight nominal vision system performance predictions for the OS lid (**top row**) and OS base (**bottom row**) based on non-sequential ray trace modeling in FRED. Left to right: +Z camera, primary circuit LEDs; +Z camera, redundant circuit LEDs; −Z camera, primary circuit LEDs and −Z camera, redundant circuit LEDs.

A feature to note in Figures 44 and 45 is that the vision system cameras have a larger field of view than is required to image the OS endcaps, and the cameras see portions of the capture cone exterior. This allows for large alignment tolerances on the camera installation and is due to ECAM lens availability and limitations on the size of the capture cone portholes. Also, a part of the capture cone flange obscures a small portion of the OS endcaps from the camera fields of view.

Unfortunately, we may encounter vision system manufacturing and assembly issues prior to launch or less than nominal conditions in flight that degrade the imaging performance predicted in Figures 44 and 45. To verify that the vision system will meet its requirements under all off-nominal conditions, we perform additional modeling to add the deleterious effects of off-nominal OS alignment, specularly reflective OS endcaps, maximum lens contamination, worst-case lens performance and worst-case detector noise.

We model the worst-case OS by changing the nominal OS surface BRDF characteristics to the most specular allowed via Equation (1). Then, we move the OS and tilt it into a post-capture tolerance extreme position that obscures more of the endcap from the cameras. This is all realized in the FRED model described in Section 5.3, and worst-case images are generated using the same procedure as for the nominal case. These worst-case images are then processed further to add image degradations caused by other effects.

To simulate particulate contamination on the first lens surface at the maximum level specified for the post-capture CCRS flight environment (0.02% areal coverage scattering ~0.05% of incident light), we convolve the worst-case images with a Mie scatter profile at normal incidence. Although we could have modeled this scatter caused by contamination with slightly higher fidelity in FRED, this simplified approach accounts for this effect with far less computation time.

To degrade the camera lens performance to the minimum level specified by the camera requirements, we convolve the worst-case images with a significantly degraded point spread function (PSF)—one that just meets the minimum MTF requirement shown in Figure 8. This worst-case PSF comes from a 1000-case Monte Carlo analysis that allowed

the lens parameters to vary randomly across a uniform distribution with the tolerances shown in Table 8. These tolerances were significantly looser than the actual fabrication and assembly tolerances prescribed by MSSS. The resulting PSF was dominated by coma and just met the minimum MTF requirement.

Table 8. Worst-case lens tolerances used in the 1000 Monte Carlo instances of the MSSS prescription. These tolerances were used to create a point spread function that just meets the minimum camera MTF requirement. Perturbed parameter values were sampled from uniform distributions centered on the nominal values. Actual MSSS fabrication and assembly tolerances are better constrained than the worst-case tolerances summarized here.

Parameter	Perturbation Limits
Radius of curvature	$\pm0.2\%$
Center thickness	±0.15 mm
Element decenter	±0.13 mm
Element tilt	$\pm0.91°$
Wedge	±0.05 mm
Surface irregularity	±633 nm PTV
n_d	±0.001
V_d	$\pm0.8\%$

Finally, detector noise is added to the worst-case simulation to simulate images with a signal-to-noise ratio of ten. Noise is added by assigning to the images new pixel values drawn from normal distributions centered on the original pixel values with the standard deviation equal to the maximum pixel value divided by ten. The image predictions for all of these combined worst-case effects are shown in Figure 46. These predictions show that even if all known effects combined together in the worst possible way, only one vision system image would be required to identify the OS post-capture orientation.
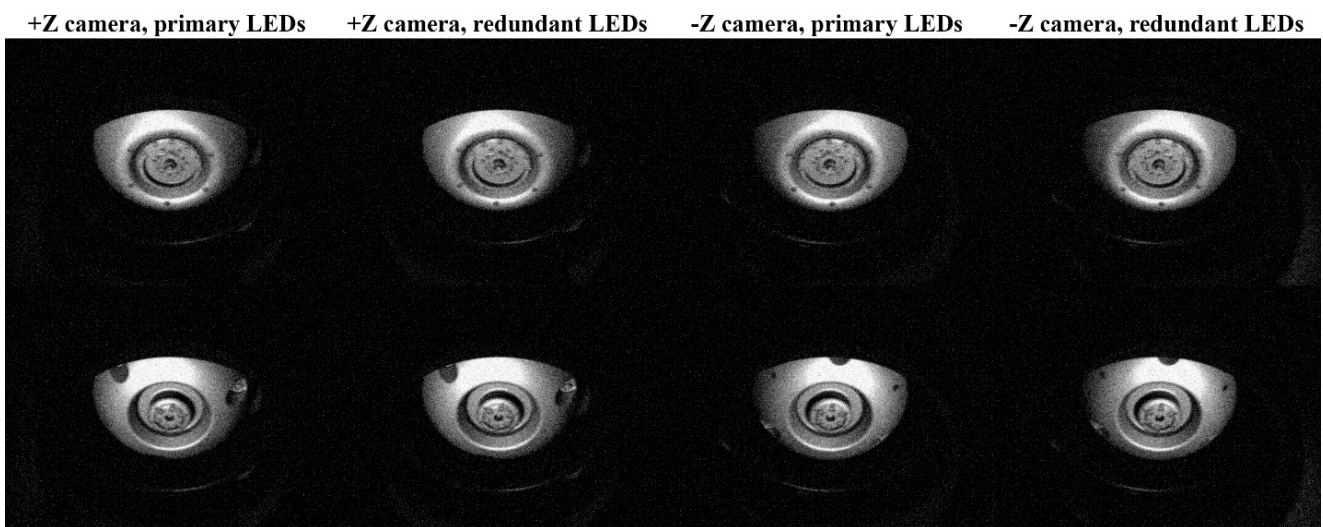

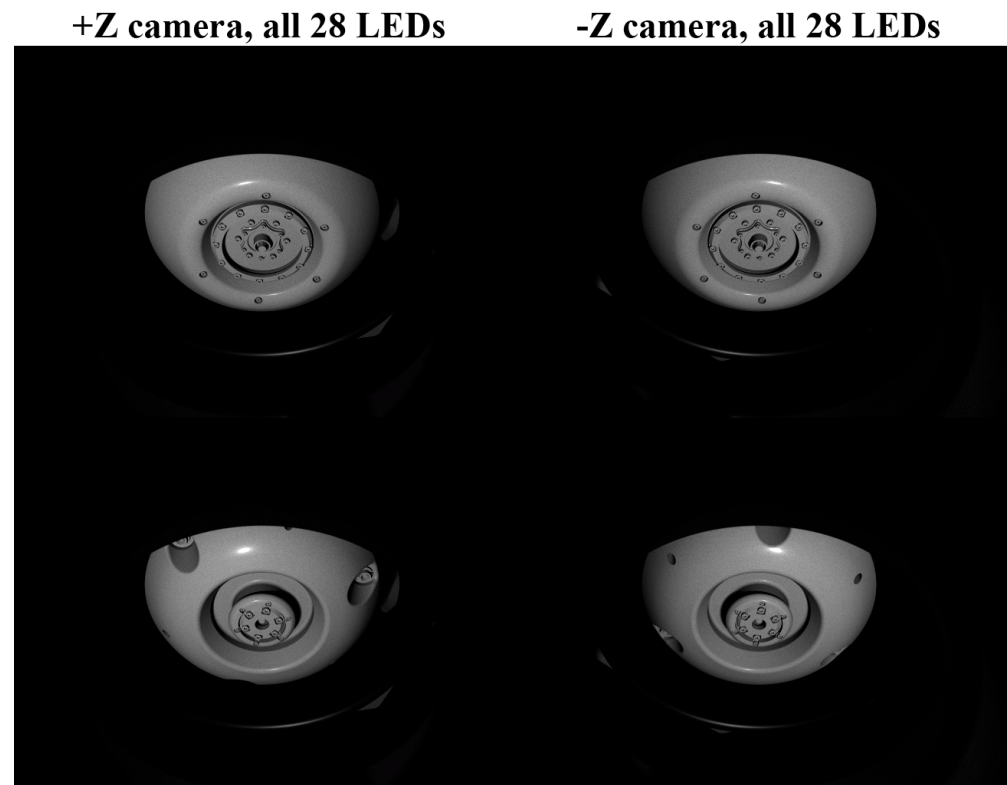**Figure 46.** Eight worst-case vision system performance predictions for the OS lid (**top row**) and OS base (**bottom row**) based on non-sequential ray trace modeling in FRED. The worst-case lens contamination; OS surface treatment; OS position and orientation; lens performance and detector noise are added to the nominal conditions to create the images. Left to right: +Z camera, primary circuit LEDs; +Z camera, redundant circuit LEDs; −Z camera, primary circuit LEDs; −Z camera, redundant circuit LEDs.

Although the nominal vision system operations concept plans for only 14 LEDs to illuminate the OS during image acquisition (from seven LEDs in each illumination module), the current baseline CCRS operations concept calls for powering on all 28 LEDs at once for the sake of operational efficiency. Figure 47 shows the nominal vision system performance if this concept is followed. The image quality is almost indistinguishable from the 14 LED case (Figure 45), slightly improves image uniformity and allows us to cut the exposure time (0.1 s) in half.

Figure 47. Four nominal vision system performance predictions for the OS lid (**top row**) and OS base (**bottom row**) based on non-sequential ray trace modeling in FRED when all 28 vision system LEDs are powered on. +Z camera images are shown in the left column. −Z camera images are shown in the right column.

6. Quantitative OS Orientation Identification Tool

During flight operations, vision system images will be evaluated on the ground by one or more observers to determine the OS orientation. For the scenarios we have investigated this will only require one image to be returned to Earth. Although highly reliable, without polling a statistically significant number of image analysts, this approach does not produce quantitative metrics with which we can quantify vision system degradation or score performance with respect to CCRS or OS modifications. To overcome this, we developed an analysis tool that trains a neural network to classify OS endcap images and generates metrics that estimate the probability of the presence of an OS lid or base.

We investigated the performance of two well-known neural network architectures: a fully connected network (FCN) with three hidden layers—perhaps the simplest type of architecture—and a slightly modified version of the LeNet convolutional neural network (CNN) [21]. These networks were trained and evaluated on a total of 2976 images. A total of 2381 images (80%) were randomly selected for training while 595 images (20%) were randomly selected to test performance. We created these images from a base set of 186 FRED-simulated images that represented different OS orientations, various OS clocking positions, different lighting conditions and OS axial positional differences of a few mm. These images were further processed in Python to randomly add blurring, contrast

reduction, lateral translation, locations of high specularity and patchy noise until a total of 2976 images were produced.

Figure 48 shows the receiver operating characteristic (ROC) curves of the two classification models. Both the FCN and the CNN models demonstrated an accuracy rate $\geq 97\%$ for the 595 images evaluated, but the FCN failed to correctly identify images that would not be challenging for a human analyst. Figure 49 shows examples of the misclassified images from both models. For our purposes, the CNN model has proven to be a better proxy than the FCN model for a trained observer.
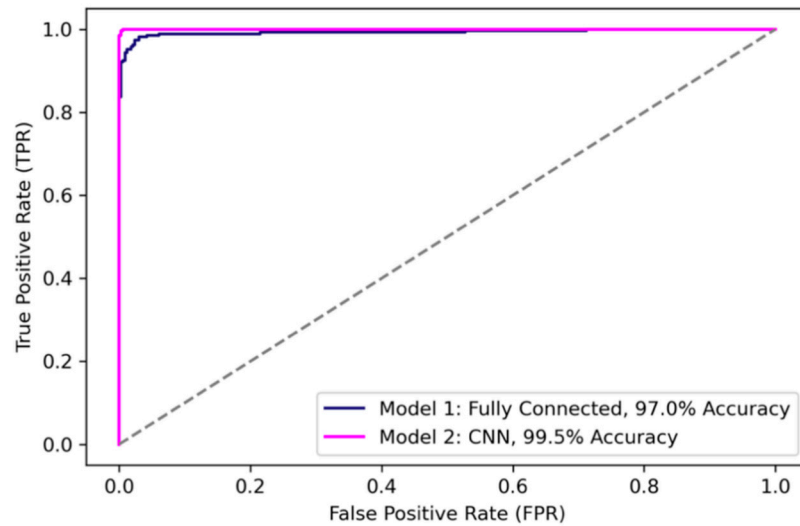
Figure 48. The receiver operating characteristic (ROC) curves for the trained fully connected network (FCN) and convolutional neural network (CNN) models, which illustrates the false positive rate at different decision thresholds. ROC curves that stay close to the top left corner indicate better performance while the dashed line corresponds to random (50/50) classification.
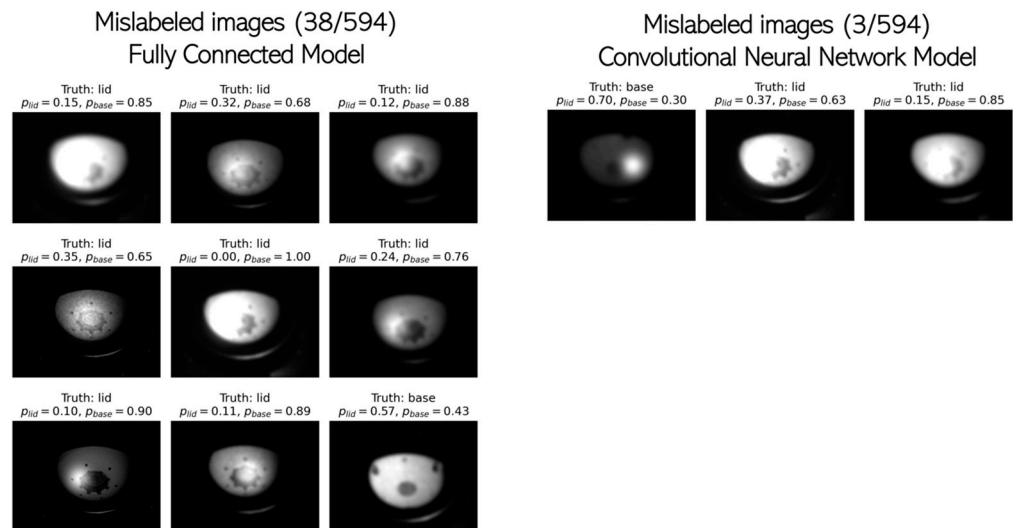

Figure 49. Examples of misidentified images and the corresponding probabilities calculated by each neural network model for a decision (identification) threshold set to $p > 0.5$. (**Left**) A random sample of 9 test images from the 38 that were misidentified via the FCN model. Several images that are easily identified by humans are confidently assigned the incorrect label via the model; for example, the bottom middle image is identified as a base endcap with an 89% probability. (**Right**) The three test images that were misidentified via the CNN model. These would also be challenging for a human observer to identify.

To help us understand the viability of the minimum MTF requirement, we allocated the CNN model to the vision system cameras we used to assess the probability of correct image identification in the presence of significant image blurring. We created blurry images of each endcap by convolving Gaussian-shaped PSFs of various sizes and classified them using the CNN model. Then we converted the PSFs into MTF curves and compared them to the nominal and worst-case camera MTFs. Figure 50 shows the results. Even though the Gaussian PSFs are only rough approximations to actual PSFs, the results indicate that cameras with significantly lower resolution than required would still capture images that would allow us to reliably verify the OS orientation.
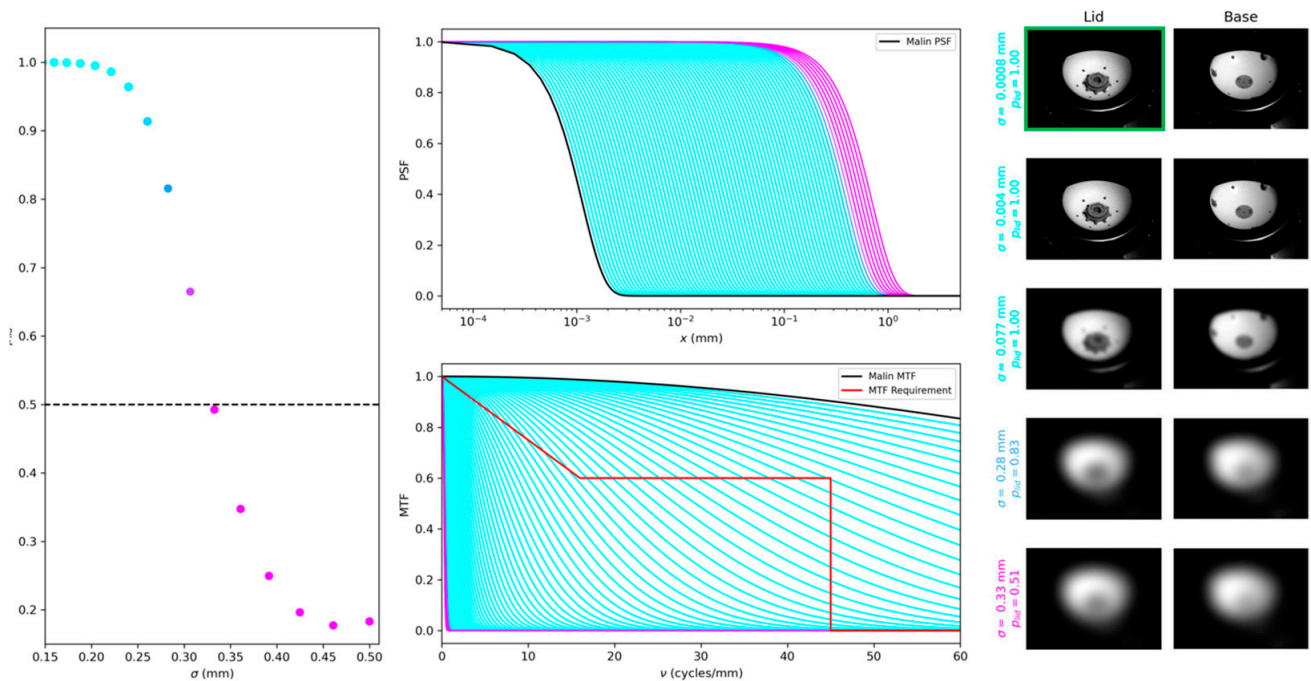

Figure 50. The impact of increasing Gaussian blur widths on the confidence of the CNN model. Different levels of blurring were applied to an image of the lid endcap, which is outlined in green on the rightmost panel. All units are in image space. (**Left**) Probabilities generated via the CNN for different Gaussian convolution kernel widths. Images that fall below the decision threshold of 0.5 are colored pink. Bluer points correspond to a higher confidence in identification. (**Middle top**) The Gaussian convolution kernels, which are effectively PSFs, next to the expected PSF of the vision system cameras (labeled "Malin PSF"). The curves are color-coded to match the points—or probabilities—shown to the left. (**Middle bottom**) The MTF for each of the blurring cases, which are the modulus of the Fourier transform of the PSFs. (**Right**) Five levels of blurring applied to the images of the lid and the base. The top row corresponds to the nominal vision system camera PSF.

7. Key Future Work Prior to Flight Unit Fabrication and Testing

The CCRS vision system design is mature, and its performance is well understood. Delivery of our flight hardware to the CCRS program will only require an additional ~13–15 months for assembly and test. Prior to the flight unit test and delivery, there are several additional pieces of work we will complete either before the flight fabrication commences or while the flight units are being assembled to reduce programmatic risk.

One of the first additional pieces of work we will pursue is modifying the illumination module baffle profile to correct the small petal design error that causes less-than-desired illumination uniformity in a small portion of the required area (discussed in Section 4.2.9). Although the vision system performs well with the current design and has sufficient margin, the design principles are well-understood, and so we deem it worthwhile to improve the illumination uniformity by modifying the baffle petal geometry. We will accomplish this by following the same design procedure described in Section 4.2.5 but will replace the

SolidWorks "Lofted Cut" calculation with a Python script written to ensure each position on the perimeter of the LED emission area has an unobstructed view of every point on the perimeter of the illumination area. The script sample points on the perimeter of each area calculates where rays connecting every combination of points between the two areas intersect the baffle cylinder and finds the intercept nearest the emission in 1° azimuthal bins around the cylinder perimeter to identify where baffle material must be removed.

Another near-term task we will complete is the construction of an engineering model (EM) camera at MSSS. Up until this point, we have only been able to test vison system performance using various EDU versions of the illumination modules combined with COTS (commercially available off-the-shelf) cameras and lenses. Upon delivery of the EM version of the flight camera, we will be able to perform higher fidelity system assessments in the laboratory without requiring data postprocessing to make the results flight-like. Although the EM camera will not be able to survive environmental testing, its optical and electrical performance will be identical to the flight units. In addition to the optical performance tests that we have planned for it, we will also use the EM camera to develop and test the CCRS-to-vision-system-camera electrical and software interfaces—providing the opportunity to identify and solve any interface issues with the flight units at least more than one year in advance of the flight model delivery.

Once the EM camera is completed, we will put it through the EMI/EMC test program described in Section 4.1 and summarized in Table 3. We plan for this to be the only EMI/EMC test of the vision system prior to higher-level test and characterization at the CCRS level. The results of this test will determine if the cameras can be compliant with the operation of the ERO Electra channel or if the CCRS will need to pursue an operational mitigation.

To support the initiation of the camera flight model construction, we will complete a camera PCB inspection at GSFC prior to approving the population of the flight and flight-spare PCBs. The flight PCB design for the particular ECAM revision that will be delivered to us is still being finalized and we will need to determine the necessity for completing a variety of inspections. Figure 51 summarizes the decision-making process for the camera PCB inspection and the number of coupons required. If the PCB is single-sided or does not include any through holes, then no additional inspection will be required. If the PCB is double-sided and has through holes, then one PCB coupon will be required for an as-delivered, dissected inspection; one coupon will be needed to go through a dissected inspection after a thermal stress test and one coupon will be provided for an X-ray fluorescence (XRF) surface finish thickness measurement. In addition, if there are any blind, buried or micro vias then additional coupons will be needed for a post thermal stress test dissected inspection of each via. The camera vendor will provide at least one extra coupon for each inspection that is required. If the PCB is constructed from a panel, then we will acquire coupons from diagonally opposite corners of the same panel as well as an accompanying layout diagram that indicates the manufacturing location of each coupon.

We will also, schedule permitting, complete a full environmental test (thermal vacuum and vibration testing) campaign of the latest EDU illumination modules that replicates the flight unit testing. Although we have already completed individual LED-level thermal testing and environmental testing of full units, the EDU test models were not identical to flight and did not endure the full number of cycles that the flight units will see. These last EDU tests will not be for a qualification campaign but will be a risk-reduction activity that will benefit the flight effort if any problems are found. This will reduce the programmatic risk of a late vision system delivery to the CCRS.
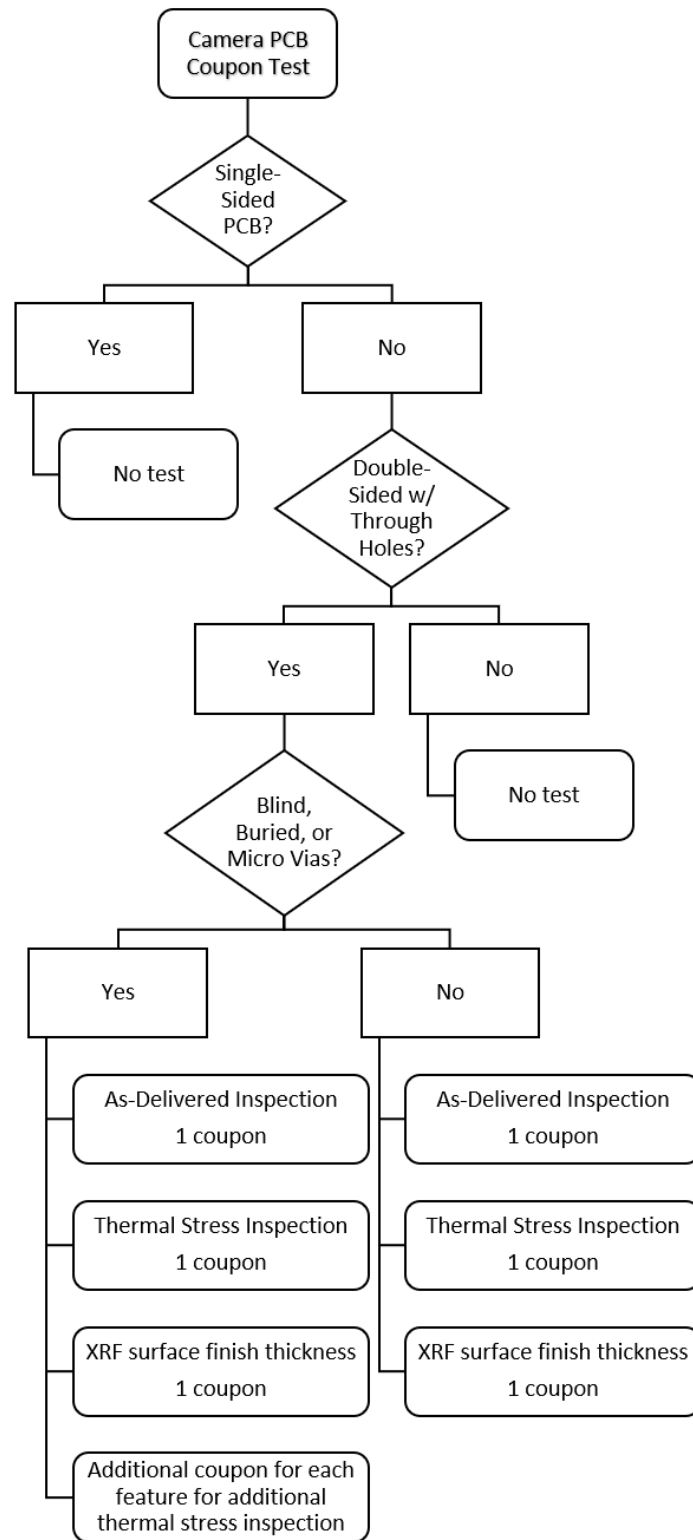
Figure 51. Summary of the vision system camera PCB pre-population inspection process.

Finally, prior to the start of the flight illumination module environmental test campaign, we will complete a PCB-level screening and assembly-level design qualification test campaign for the illumination modules. This will identify reliable LED/PCB assemblies for the flight-build as well as ensure LED long-term survivability. Although the illumination module resistors are purchased flight-qualified, the LEDs are not. As described in Section 4.2, we have already completed a significant amount of testing to prove the LED

design is compatible with the CCRS environment (the same LED design also has significant Mars flight heritage). Our efforts will establish that the commercial LED lot we purchased is suitable for our task.

Figure 52 shows a summary of our plans for identifying the flight model illumination module populated PCBs and the final tests to confirm the viability of our LED lot. The PCB screening tests include 160 h of continuous operation at 112 mA of current at room temperature followed by ten unpowered thermal cycles to survival limits on 20 fully populated PCBS. After completing the screening, we will select eight PCBs for the flight and flight-spare illumination modules. Seven of the remaining twelve PCBs will be assembled into full illumination modules for qualification testing and be exposed to conditions we do not want to expose the flight and flight-spare models to prior to flight operations. This includes a lifetime electrical test on three units for 1000 h at 186 mA and vibration testing followed by 100 thermal cycles to survival limits on four units. Due to the excellent results from the EDU radiation testing, we have determined that follow-up radiation testing is not required for this qualification campaign.
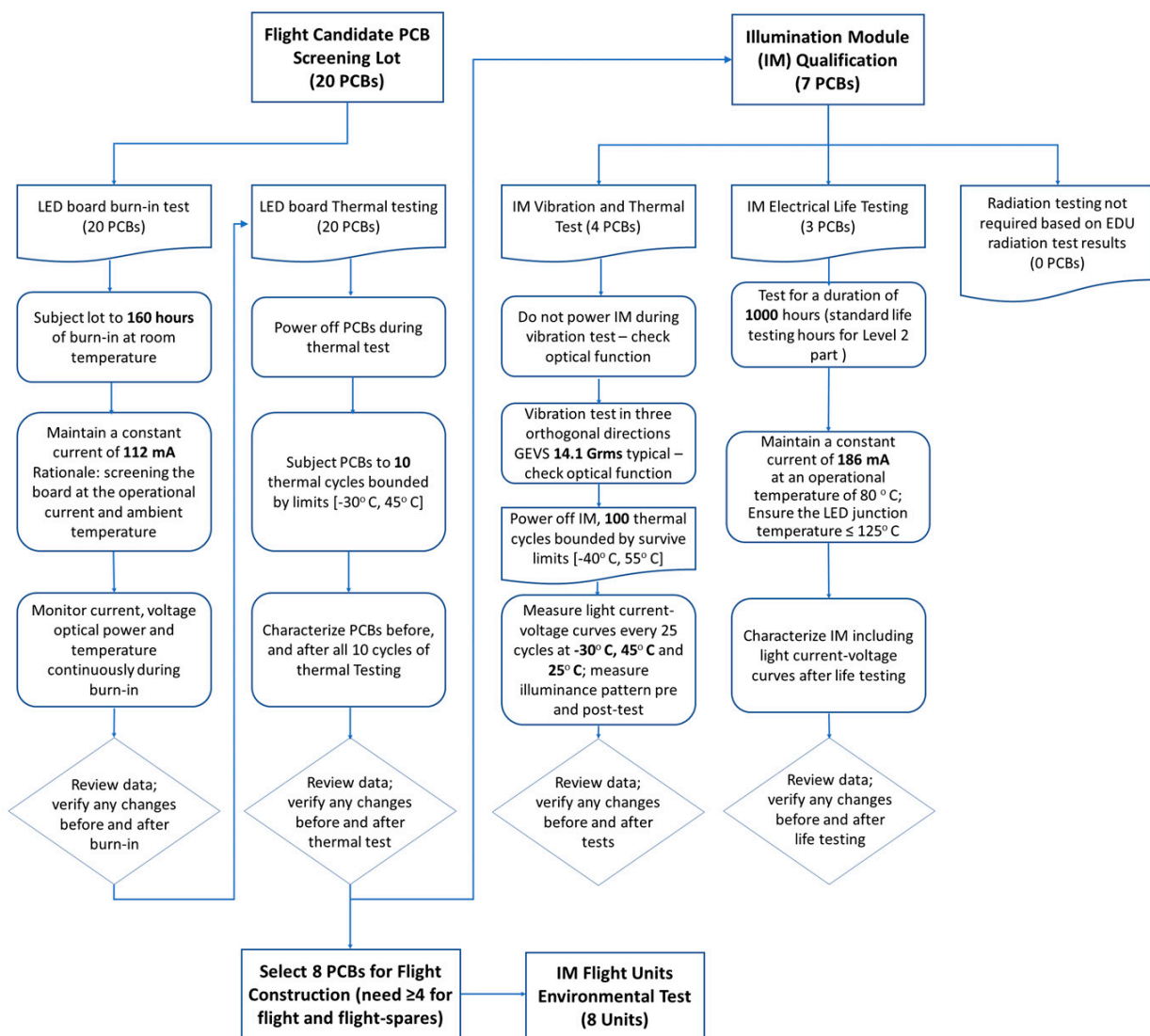

Figure 52. Summary flow diagram of the illumination system printed circuit board (PCB) flight screening and illumination module qualification plans.

8. Conclusions and Summary

We have developed a vision system for the MSR campaign to serve as a component of the ERO CCRS payload. It provides key telemetry regarding CCRS processing of the OS container in Mars orbit. The system consists of two cameras sensitive to the visible portion of the electromagnetic spectrum and two illumination modules constructed from broadband light emitting diodes (LED).

The CCRS vision system is fully redundant and robust to multiple combinations of CCRS and vision system failure modes. The cameras we have selected and designed the system around have significant spaceflight heritage and have already proven themselves as part of the OSIRIS-REx asteroid sample return mission. The new illumination system we developed for this application is designed around LEDs that have been successfully operating on the surface of Mars for more than three years. Our vision system laboratory tests and physics-based optical simulations predict that CCRS ground processing will be able to correctly identify the OS post-capture orientation using only a single vision system image that is transmitted to Earth from Mars orbit.

The CCRS vision system flight hardware was on schedule to be fully assembled, flight qualified and delivered during the first half of 2025 when NASA put CCRS design and construction on hold following the CCRS preliminary design review (PDR) in late 2023.

The NASA and ESA MSR campaign is arguably the most ambitious robotic planetary exploration program planned to date. Due to its complexity and accompanying costs, the entire program is currently under review by NASA and other stakeholders. This document is being made available for information purposes only. The decision to implement Mars Sample Return will not be finalized until NASA's completion of the National Environmental Policy Act (NEPA) process. In addition, as part of the NASA response to the recent MSR Independent Review Board's report [22], and in light of the current budget environment, the MSR Program is undergoing a consideration of changes in its mission architecture. This work is based upon the previous baseline MSR architecture in which ERO/CCRS would return the OS to Earth within approximately five years of landing on Mars to retrieve samples collected by the Perseverance rover. The CCRS project completed system development to a Preliminary Design Review level of maturity in mid-December 2023, after which it was stopped indefinitely pending the results of the re-architecting effort. This may affect the current launch readiness dates of both the ERO and SRL and impact the requirements placed on all the major components—including the CCRS. Whatever comes out of this activity, we have developed a robust, flexible and reliable imaging system for the Mars environment that can be used in support of the MSR campaign or any other spaceflight mission targeting Mars orbit.

Author Contributions: Conceptualization, B.J.B., D.L.D., J.I.C., C.W., M.A.R., M.C., I.O., C.S., R.A.E., D.A.H., C.M.Y. and E.L.D.M.; methodology, B.J.B., R.P., J.I.C., B.R.; J.-M.L., K.L.R., M.J.C., D.E.J., W.J.T., R.G.S., J.C.M., A.H.L. and B.Y.; software, J.I.C., T.C.H., R.P., K.C.O., M.T.H., E.P. and E.L.; validation, T.C.H., R.P. and J.I.C.; formal analysis, T.C.H., R.P. and J.I.C.; investigation, T.C.H., C.W., G.T.G., K.A.W., P.C., E.P., L.Q.V., K.C.O., B.D., L.H., C.T., M.H. and B.B.; resources, B.J.B., D.E.B., R.R.B. and E.M.G.; data curation, B.J.B., D.L.D., J.I.C., C.W., T.C.H., D.E.B., Y.Z., R.P., B.R., G.T.G., M.J.S. and S.I.; writing—original draft preparation, B.J.B., D.L.D., J.I.C., C.W., T.C.H., D.E.B., Y.Z., R.P., B.R., R.A.E., D.A.H., C.S., G.T.G., M.C. and E.L.; writing—review and editing, B.J.B., D.L.D., J.I.C., C.W., T.C.H., D.E.B., Y.Z., R.P., B.R., R.A.E., D.A.H., C.S., G.T.G., M.C. and E.L.; visualization, B.J.B., D.L.D., J.I.C., C.W., T.C.H., D.E.B., Y.Z., R.P., B.R., R.A.E., D.A.H., C.S., G.T.G., E.L.D.M., M.C. and E.L.; supervision, B.J.B., E.M.G., C.W., Y.Z. and D.E.B.; project administration, B.J.B. and D.E.B.; funding acquisition, B.J.B. All authors have read and agreed to the published version of the manuscript.

References

1. Sun, V.Z.; Hand, K.P.; Stack, K.M.; Farley, K.A.; Simon, J.I.; Newman, C.; Sharma, S.; Liu, Y.; Wiens, R.C.; Williams, A.J.; et al. Overview and Results from the Mars 2020 Perseverance Rover's First Science Campaign on the Jezero Crater Floor. *J. Geophys. Res. Planets* **2023**, *128*, e2022JE007613. [CrossRef]
2. Tzanetos, T.; Aung, M.; Balaram, J.; Grip, H.F.; Karras, J.T.; Canham, T.K.; Kubiak, G.; Anderson, J.; Merewether, G.; Starch, M.; et al. Ingenuity Mars Helicopter: From Technology Demonstration to Extraterrestrial Scout. In Proceedings of the 2022 IEEE Aerospace Conference (AERO), Big Sky, MT, USA, 5–12 March 2022; pp. 1–19. [CrossRef]
3. Hughes, D.W.; Catalado, G.; Pellerano, F.A.; Hardwick, T.C.; Micalizzi, F.; Chambers, V.J.; Bean, B.R.; Braley, B.J.; Cook, W.B.; Day, R.; et al. Lessons Learned in Designing an Ultraviolet Sterilization System for Space. *Aerospace*.
4. Smith, P.H.; Tomasko, M.G.; Britt, D.; Crowe, D.G.; Reid, R.; Keller, H.U.; Thomas, N.; Gliem, F.; Rueffer, P.; Sullivan, R.; et al. The imager for Mars Pathfinder experiment. *J. Geophys. Res.* **1997**, *102*, 4003–4025. [CrossRef]
5. Reid, R.J.; Smith, P.H.; Lemmon, M.; Tanner, R.; Burkland, M.; Wegryn, E.; Weinberg, J.; Marcialis, R.; Britt, D.T.; Thomas, N.; et al. Imager for Mars Pathfinder (IMP) image calibration. *J. Geophys. Res.* **1999**, *104*, 8907–8925. [CrossRef]
6. Bos, B.J. Design, Calibration and Operation of Mars Lander Cameras. Ph.D. Thesis, University of Arizona, Tucson, AZ, USA, 2002.
7. Keller, H.U.; Goetz, W.; Hartwig, H.; Hviid, S.F.; Kramm, R.; Markiewicz, W.J.; Reynolds, R.; Shinohara, C.; Smith, P.; Tanner, R.; et al. Phoenix Robotic Arm Camera. *J. Geophys. Res.* **2008**, *113*, E00A17. [CrossRef]
8. Bos, B.J.; Ravine, M.A.; Caplinger, M.; Schaffner, J.A.; Ladewig, J.V.; Olds, R.D.; Norman, C.D.; Huish, D.; Hughes, M.; Anderson, S.K.; et al. Touch And Go Camera System (TAGCAMS) for the OSIRIS-REx Asteroid Sample Return Mission. *Space Sci. Rev.* **2018**, *214*, 37. [CrossRef]
9. Bos, B.J.; Nelson, D.S.; Pelgrift, J.Y.; Liounis, A.J.; Doelling, D.; Norman, C.D.; Olds, R.D.; May, C.W.; Witherspoon, R.; Church, E.; et al. In-Flight Calibration and Performance of the OSIRIS-REx Touch and Go Camera System (TAGCAMS). *Space Sci. Rev.* **2020**, *216*, 71. [CrossRef]
10. Bell, J.F.; Zhao, Y.; Cisneros, E.; Beasley, M.; Olkin, C.; Caplinger, M.A.; Ravine, M.A.; Schaffner, J.A.; Clark, M.J.; Shamah, J.; et al. The Terminal Tracking Camera System on the NASA Lucy Trojan Asteroid Discovery Mission. *Space Sci. Rev.* **2023**, *219*, 86. [CrossRef]
11. Edwards, C.D. The Electra Proximity Link Payload for Mars Relay Telecommunications and Navigation. In Proceedings of the 54th International Astronautical Congress of the IAF, the International Academy of Astronautics, and the International Institute of Space Law, Bremen, Germany, 29 September—3 October 2003. [CrossRef]
12. Maki, J.N.; Gruel, D.; McKinney, C.; Ravine, M.A.; Morales, M.; Lee, D.; Willson, R.; Copley-Woods, D.; Valvo, M.; Goodsall, T.; et al. The Mars 2020 Engineering Cameras and Microphone on the Perseverance Rover: A Next-Generation Imaging System for Mars Exploration. *Space Sci. Rev.* **2020**, *216*, 137. [CrossRef] [PubMed]
13. *MIL-STD-1504C*; Department of Defense Standard Practice: Abrasive Blasting. USAF: Washington, DC, USA, 2007.
14. *MIL-PRF-9954D*; Performance Specification: Glass Beads: For Cleaning and Peening. USAF: Washington, DC, USA, 2009.
15. *MIL-A-8625F*; Military Specification: Anodic Coatings for Aluminum and Aluminum Alloys. USAF: Washington, DC, USA, 1993.
16. *MIL-DTL-5541F*; Detail Specification: Chemical Conversion Coatings on Aluminum and Aluminum Alloys. USAF: Washington, DC, USA, 2006.
17. Gilmore, D.G. *Spacecraft Thermal Control Handbook, Volume I: Fundamental Technologies*; Aerospace Press: El Segundo, CA, USA, 2002. [CrossRef]
18. Georgiev, G.T.; Butler, J.J.; Thome, K.; Cooksey, C.; Ding, L. Establishing BRDF Calibration Capabilities Through Shortwave Infrared. In Proceedings of the SPIE Optical Engineering + Applications, San Diego, CA, USA, 6–10 August 2017; Volume 10402, p. 104021N. [CrossRef]
19. Optikos Corporation. LensCheck Finite Conjugate System, [Apparatus and Software]. 2020. Available online: www.optikos.com/lens-testing-equipment (accessed on 23 February 2024).
20. Harvey, J.E. Light-Scattering Characteristics of Optical Surfaces. In Proceedings of the 1977 SPIE/SPSE Technical Symposium East, Reston, VA, USA, 18–21 April 1977. [CrossRef]

21. Lecun, Y.; Bottou, L.; Haffner, P. Gradient-based learning applied to document recognition. *Proc. IEEE* **1998**, *86*, 2278–2324. [CrossRef]

22. Figueroa, O.; Kearns, S.; Boll, N.; Elbel, J. Mars Sample Return (MSR) Independent Review Board-2 Final Report. 2023. Available online: www.nasa.gov/wp-content/uploads/2023/09/mars-sample-return-independent-review-board-report.pdf (accessed on 23 February 2024).